輔仁學誌—理工類

中華民國九十年十二月　　第三十五期

目錄

FU JEN STUDIES

SCIENCE AND ENGINEERING

NO. 35, DEC. 2001

CONTENTS

輔仁學誌—理工類

FU JEN STUDIES

----SCIENCE AND ENGINEERING

發行人 Publisher

郭維夏 副校長 (Michael G. Kwo, SVD, Vice President)

出版者 私立輔仁大學理工學院

臺北縣新莊市中正路 510 號

電話：(02)2903-1111 轉 2411

傳真：(02)29014749

承印者 至潔有限公司

臺北市桂林路 28-3 號 2 樓

電話：(02)2302-6442

傳真：(02)2302-7562

ISSN 1028-5679

輔仁學誌——理工類

第三十五期

FU JEN STUDIES

SCIENCE AND ENGINEERING

No. 35, Dec. 2001

SINCE 1925

輔仁大學理工學院
中華民國九十年十二月

COLLEGE OF SCIENCE AND ENGINEERING
FU JEN CATHOLIC UNIVERSITY
TAIPEI, TAIWAN, R.O.C.

Rigorous Proofs of the Expansion Theorems in the Problems of Forced Capillary-Gravity Waves Generated by Vertical Wavemakers

Nai-Sher Yeh

Mathematics Separtment
Fu- Jen Catholic University

Abstract

The purpose of this paper is to rigorously prove the expansion theorems in the linearized problems of forced capillary-gravity waves generated by vertical wavemakers proposed by Rhodes-Robinson [1971]. The use of these expansion theorems will also be demonstrated.

I. INTRODUCTION

The problems of forced capillary-gravity waves have been long studied. Havlock [1929] published a paper regarding the problem of forced surface waves under gravity generated by a plane wave maker. Later Evans [1968] studied the problem of a heaving cylinder in a fluid with the effect of surface tension included and proposed an edge condition. Hocking [1987] proposed another dynamic edge condition that at a contact line the time derivative of the free surface is proportional to the slope of the free surface. Both of these edge conditions have been studied for their contributions to the solution of related problems. Rhodes-Robinson [1971] studied the problems of forced capillary-gravity waves generated by a plane or cylindrical wavemaker under Evans' edge condition. In his construction of solutions, some very unconventional expansion theorems for arbitrary functions defined on either

a finite closed interval or an infinite half-closed-half-open interval were introduced. However, rigorous proofs for these theorems were not given.

These expansion theorems mentioned above are very powerful in solving forced capillary-gravity waves problems in either edge conditions. The purpose of this paper is to give rigorous proofs to these expansion theorems, and some simple demonstrations of how the solutions are obtained through these theorems. Finite depth and infinite depth cases will be handled separately.

II. FORMULATIONS

The formulation of the plane wavemaker problem is as the following:

(A). Plane Wavemakers (See Figure 1)

1). Formulation

$$\Psi = \Psi(x,y,t),\ \nabla_2^2\Psi = 0 \text{ in } (0,\infty)\times(-h,0) \text{ (or } (0,\infty)\times(-\infty,0)),$$
$$\Psi_y = Z_t \text{ and } \Psi_t + gZ = T\nabla_1^2 Z \text{ on } S,\ \Psi_y = 0 \text{ on } y=-h,$$
$$(\Psi_{\infty y}\to 0 \text{ as } y\to-\infty,)$$
$$\Psi_x = u(y)\,e^{i\omega t} \text{ on } x=0,\ \Psi\to C_0 e^{i(k_0x+\omega t)}\cosh k_0(h+y) \text{ as } x\to\infty,$$
$$(\Psi_\infty\to \widehat{C_0}e^{i(k_0x+\omega t)+k_0y} \text{ as } x\to\infty,)$$

where in Ψ, k_0 is the positive root of

$$\Delta_0(\alpha) = \alpha(T\alpha^2+1)\sinh\alpha h - \omega^2\cosh\alpha h = 0;$$

and in Ψ_∞, k_0 is the positive root in

$$\Delta_{\infty 0}(\alpha) = \alpha(T\alpha^2+1) - \omega^2 = 0.$$

Hocking's Edge Condition: $Z_x = \delta Z_t$ at $x=0$, $y=0$.

2). Time-reduce and non-dimensionalize the problem

Let $\Psi(x,y,t) = \psi(x,y)\,e^{i\omega t}$,
and $Z(x,t) = \varsigma(x)\,e^{i\omega t}$, then we find that

$$\nabla_2^2\psi = 0 \text{ in } (0,\infty)\times(-1,0) \text{ (or } (0,\infty)\times(-\infty,0)),$$
$$\psi_y = i\omega\varsigma \text{ and } i\omega\psi + g\varsigma = T\nabla_1^2\varsigma \text{ on } y=-1,$$
$$\psi_x = u(y) \text{ on } x=0,\ \psi_y = 0 \text{ on } y=-1,\ (\psi_{\infty y}\to 0 \text{ as } y\to-\infty,)$$
$$\psi\to C_0 e^{ik_0x}\cosh(k_0(1+y)) \text{ as } x\to\infty,\ (\psi_\infty\to\widehat{C_0}e^{k_0(ix+y)} \text{ as } x\to\infty,)$$

and $\psi_{xy} = i\omega\delta\psi_y$ at Γ.

(B). Cylindrical Wavemaker (See Figure 2)

1). Formulation

$$\nabla_3^2\Phi = 0 \text{ in } V = (0,\infty)\times(0,2\pi)\times(-h,0) \text{ (or } (0,\infty)\times(0,2\pi)\times(-\infty,0))$$
$$\Phi_z = Z_t \text{ and } \Phi_t + gZ = T\nabla_2^2 Z \text{ on } z=0\ (S),$$
$$\Phi_r = f(z)\,e^{i(\omega t\pm m\theta)} \text{ on } r=a,\ \Phi_z = 0 \text{ on } z=-h,\ (\Phi_{\infty z}\to 0 \text{ as } z\to-\infty,)$$
$$\Phi \to C_0 \mathrm{H}_m^{(1)}(k_0 r)\,e^{i(\omega t\pm m\theta)}\cosh(k_0(h+z)) \text{ as } r\to\infty,$$
$$(\Phi_\infty \to \widehat{C_0}\mathrm{H}_m^{(1)}(k_0 r)\,e^{i(\omega t\pm m\theta)+k_0 z} \text{ as } r\to\infty,)$$

where in Φ, k_0 is the positive root of

$$\Delta_0(\alpha) = \alpha(T\alpha^2+1)\sinh\alpha h - \omega^2\cosh\alpha h = 0;$$

and in Φ_∞, k_0 is the positive root in

$$\Delta_{\infty 0}(\alpha) = \alpha(T\alpha^2+1) - \omega^2 = 0.$$

Hocking's Edge Condition: $Z_r = \delta Z_t$ at $r=a$, $z=0$.

2). Time-and-θ-reduce and non-dimensionalize the problem

Let $\Phi(r,\theta,z,t) = \varphi(r,z)\,e^{i(\omega t\pm m\theta)}$,

and $Z(r,\theta,t) = \varsigma(r)\,e^{i(\omega t\pm m\theta)}$. Then we have

$$\mathcal{L}_2\varphi = 0 \text{ in } V,\ \varphi_z = i\omega\zeta \text{ and } i\omega\varphi + g\zeta = T\mathcal{L}_1\zeta \text{ on } S,$$
$$\varphi_r = f(z) \text{ on } r=a,\ \varphi_z = 0 \text{ on } z=-1,\ (\varphi_{\infty z}\to 0 \text{ as } z\to-\infty,)$$
$$\varphi \to C_0\,\mathrm{H}_m^{(1)}(k_0 r)\cosh(k_0(1+z)) \text{ as } r\to\infty,$$
$$(\varphi_\infty \to \widehat{C_0}\,\mathrm{H}_m^{(1)}(k_0 r)\,e^{k_0 z} \text{ as } r\to\infty,)$$

and $\varphi_{rz} = i\omega\delta\varphi_z$ at $r=a$, $z=0$,

where

$$\mathcal{L}_2 = \mathcal{L}_1 + \frac{\partial^2}{\partial z^2} = \frac{1}{r}\frac{\partial}{\partial r}\left(r\frac{\partial}{\partial r}\right) - \frac{m^2}{r^2} + \frac{\partial^2}{\partial z^2}.$$

We now give a full description and proofs to the expansion theorems.

III. EXPANSION THEOREMS AND PROOFS.

The unconventional idea of these theorems are to add zero terms with arbitrary parameters as their coefficients. The motivation for this formulation is to fit various types of edge conditions.

(1). Expansion theorem for finite depth

Theorem 0.1. An arbitrary smooth function $u(y)$ for $-1< y < 0$ posseses a series expansion

$$u(y) = 2\Big[\tfrac{2}{\beta_0}k_0\left(1+Tk_0^2\right)\left(\cosh\left(k_0\left(1+y\right)\right)\right)\int_{-1}^{0} u\cdot\left(\cosh\left(k_0\left(1+\eta\right)\right)\right)d\eta$$
$$+\sum_{n=1}^{\infty}\tfrac{2}{\beta_n}k_n\left(1-Tk_n^2\right)\left(\cos k_n\left(1+y\right)\right)\int_{-1}^{0} u\left(\cos k_n\left(1+\eta\right)\right)d\eta\Big]$$
$$-2\pi T\mu\Big[\tfrac{2}{\beta_0}k_0\left(\cosh\ k_0\right)\left(\cosh\left(k_0\left(1+y\right)\right)\right)+\sum_{n=1}^{\infty}\tfrac{2}{\beta_n}k_n\left(\cos k_n\right)\left(\cos k_n\left(1+y\right)\right)\Big],\ (*)$$

where $\beta_0 = 2k_0\left(1+Tk_0^2\right)+\left(1+3Tk_0^2\right)\sinh 2k_0$, $\beta_n = 2k_n\left(1-Tk_n^2\right)+\left(1-3Tk_n^2\right)\sin 2k_n$, $n = 1,2,3,...;\ \ k_0, k_n > 0, \forall n;\ \{\pm k_0, \pm ik_n\}_{n=1}^{\infty}$ are roots of $\alpha\left(T\alpha^2+1\right)\sinh\alpha - \omega^2\cosh\alpha = 0$, *and* μ *is an arbitrary parameter.*

Poof. First of all, set $u(y) = 2u_1(y) - 2\pi\mu u_2(y)$, where

$$u_1(y) = \tfrac{1}{\beta_0}\Big[2k_0\left(1+Tk_0^2\right)\left(\cosh\left(k_0\left(1+y\right)\right)\right)\int_{-1}^{0} u\cdot\left(\cosh\left(k_0\left(1+\eta\right)\right)\right)d\eta$$
$$+2\sum_{n=1}^{\infty}\tfrac{1}{\beta_n}k_n\left(1-Tk_n^2\right)\left(\cos k_n\left(1+y\right)\right)\int_{-1}^{0} u\left(\cos k_n\left(1+\eta\right)\right)d\eta\Big],$$

$$u_2(y) = \tfrac{1}{\beta_0}\Big[2k_0\left(\cosh\ k_0\right)\left(\cosh\left(k_0\left(1+y\right)\right)\right)\Big]+2\sum_{n=1}^{\infty}\Big[\tfrac{k_n}{\beta_n}\left(\cos k_n\right)\left(\cos k_n\left(1+y\right)\right)\Big].$$

Consider the integral

$$\mathbf{I} = \tfrac{1}{2\pi i}\int_C \tfrac{\alpha}{\Delta(\alpha)}\left(\cosh\left(\alpha\left(1+y\right)\right)\right)d\alpha,$$

where C is the contour from $-\infty$ to ∞, indented above $-k_0$ and below k_0. This integral is identically 0, since the integrand is an odd function. By residue theorem, $\mathbf{I}$ can be written as

$$\mathbf{I} = 2\pi i\cdot\tfrac{1}{2\pi i}\Big[\textstyle\sum_{n=1}^{\infty}\lim_{\alpha\to ik_n}\tfrac{\alpha(\alpha-ik_n)}{\Delta(\alpha)}(\cosh(\alpha(1+y))+\lim_{\alpha\to k_0}\tfrac{\alpha(\alpha-k_0)}{\Delta(\alpha)}(\cosh(\alpha(1+y)))\Big]$$
$$= \tfrac{k_0(\cosh k_0)(\cosh(k_0(1+y)))}{k_0(1+Tk_0^2)(\cosh^2 k_0)+(1+3Tk_0^2)(\sinh k_0)(\cosh k_0)-\omega^2(\sinh k_0)(\cosh k_0)}$$
$$+\textstyle\sum_{n=1}^{\infty}\tfrac{k_n(\cos k_n)(\cos(k_n(1+y)))}{k_n(1-Tk_n^2)\cos^2 k_n+(1-3Tk_n^2)(\sin k_n)(\cos k_n)-\omega^2(\sin k_n)(\cos k_n)}$$
$$= \tfrac{2k_0(\cosh k_0)(\cosh(k_0(1+y)))}{2k_0(1+Tk_0^2)+(1+3Tk_0^2)\sinh 2k_0}+\textstyle\sum_{n=1}^{\infty}\tfrac{2k_n(\cos k_n)(\cos(k_n(1+y)))}{2k_n(1-Tk_n^2)+(1-3Tk_n^2)\sin 2k_n}$$
$$= u_2(y),$$

that is, $\mathbf{I} = u_2(y) = 0$. It follows that

$$u(y) = 2u_1(y).$$

By making use of the relations described above,

$$u_1(y) = 2\omega^2\left\{\frac{1}{\beta_0}\left[(\cosh(k_0(1+y)))(\coth k_0)\int_{-1}^{0} u\cosh(k_0(1+\eta))d\eta\right]\right.$$
$$\left.+\sum_{n=1}^{\infty}\frac{1}{\beta_n}\left[(\cos(k_n(1+y)))(\cot k_n)\int_{-1}^{0} u\cos(k_n(1+\eta))d\eta\right]\right\}$$
$$= 2\omega^2\left\{\frac{(\cosh(k_0(1+y)))(\cosh k_0)\int_{-1}^{0} u\cosh(k_0(1+\eta))d\eta}{2k_0(1+Tk_0^2)\sinh k_0+(1+3Tk_0^2)\cdot 2\cosh k_0}\right.$$
$$\left.+\sum_{n=1}^{\infty}\frac{(\cos(k_n(1+y)))(\cos k_n)\int_{-1}^{0} u\cos(k_n(1+\eta))d\eta}{2k_n(1-Tk_n^2)\sin k_n+(1-3Tk_n^2)\cdot 2\cos k_n}\right\}.$$

Notice that for sufficiently large n,

$$\frac{1}{2}\left|\frac{(\cos(k_n(1+y)))(\cos(k_n(1+\eta)))\cos k_n}{k_n(1-Tk_n^2)\sin k_n+(1-3Tk_n^2)\cos k_n}\right| \le \frac{1}{6Tk_n^2},$$

and the series

$$\frac{1}{2}\sum_{n=1}^{\infty}\frac{(\cos(k_n(1+y)))(\cos(k_n(1+\eta)))\cos k_n}{k_n(1-Tk_n^2)\sin k_n+(1-3Tk_n^2)\cos k_n},$$

converges uniformly, according to Weierstrass M-test. Hence $u_1(y)$ can be written as

$$u_1(y) = \int_{-1}^{0} u(\eta)\left\{\frac{1}{\beta_0}[2k_0(1+Tk_0^2)(\cosh(k_0(1+y)))(\cosh(k_0(1+\eta)))]\right.$$
$$\left.+\sum_{n=1}^{\infty}\frac{1}{\beta_n}[2k_n(1-Tk_n^2)(\cos(k_n(1+y)))(\cos(k_n(1+\eta)))]\right\}d\eta$$
$$= \int_{1}^{0} u(\eta)U(y,\eta)d\eta,$$

where

$$U(y,\eta) = \frac{1}{\beta_0}[2k_0(1+Tk_0^2)(\cosh(k_0(1+y)))(\cosh(k_0(1+\eta)))]$$
$$+\sum_{n=1}^{\infty}\frac{1}{\beta_n}[2k_n(1-Tk_n^2)(\cos(k_n(1+y)))(\cos(k_n(1+\eta)))].$$

Note that when $y \neq 0$, U can be written as the following:

$$U = \frac{1}{2\pi i}\int_C \frac{1}{\Delta(\alpha)(\cosh\alpha)}[\alpha(T\alpha^2+1)(\cosh(\alpha(1+y)))(\cosh(\alpha(1+\eta)))]d\alpha$$
$$-\sum_{\{\alpha|\cosh\alpha=0\}}\mathrm{Res}[\mathbf{P}(\alpha)],$$

where C is the contour described above,

$$\mathbf{P} \equiv \frac{1}{\Delta(\alpha)(\cosh\alpha)}[\alpha(T\alpha^2+1)(\cosh(\alpha(1+y)))(\cosh(\alpha(1+\eta)))]$$

is an odd function, and the zeros of $\cosh\alpha$ are

$\alpha = \left(n - \frac{1}{2}\right)\pi i, \quad n = 1, 2, 3, \cdots$. For a fixed n,

$$\text{Res}\left[\mathbf{P}(\alpha = \left(n - \tfrac{1}{2}\right)\pi i)\right] = \lim_{\alpha \to \left(n-\frac{1}{2}\right)\pi i} \frac{\alpha - \left(n-\frac{1}{2}\right)\pi i}{\Delta(\alpha)(\cosh\alpha)} \times \left[\alpha(T\alpha^2 + 1)(\cosh(\alpha(1+y)))(\cosh(\alpha(1+\eta)))\right]$$

$$= \frac{\cos\left[\left(n-\frac{1}{2}\right)\pi(1+y)\right]}{i\sin\left(n-\frac{1}{2}\right)\pi} \cdot \frac{\cos\left[\left(n-\frac{1}{2}\right)\pi(1+\eta)\right]}{i\sin\left(n-\frac{1}{2}\right)\pi}$$

$$= (-1)^{2n+1}\left\{\cos\left[\left(n - \tfrac{1}{2}\right)\pi(1+y)\right]\right\}\left\{\cos\left[\left(n - \tfrac{1}{2}\right)\pi(1+\eta)\right]\right\}$$

$$= -(-1)^{n+1}\left(\sin\left(\left(n - \tfrac{1}{2}\right)\pi y\right)\right)(-1)^{n+1}\left(\sin\left(\left(n - \tfrac{1}{2}\right)\pi\eta\right)\right)$$

$$= -\left(\sin\left(\left(n - \tfrac{1}{2}\right)\pi y\right)\right)\left(\sin\left(\left(n - \tfrac{1}{2}\right)\pi\eta\right)\right).$$

Again, the integral part of U is zero due to an odd integrand, we find

$$U = -\sum_{n=1}^{\infty} \text{Res}\left[\mathbf{P}\left(\alpha = \left(n - \tfrac{1}{2}\right)\pi i\right)\right] = \sum_{n=1}^{\infty}\left(\sin\left(\left(n - \tfrac{1}{2}\right)\pi y\right)\right)\left(\sin\left(\left(n - \tfrac{1}{2}\right)\pi\eta\right)\right), \quad (1)$$

which implies that

$$u(y) = 2u_1(y) = 2\int_{-1}^{0} u(\eta)U(y,\eta)d\eta$$

$$= 2\int_{-1}^{0}\sum_{n=1}^{\infty} u(\eta)\left(\sin\left(\left(n - \tfrac{1}{2}\right)\pi y\right)\right)\left(\sin\left(\left(n - \tfrac{1}{2}\right)\pi\eta\right)\right)d\eta$$

$$= 2\sum_{n=1}^{\infty}\left(\int_{-1}^{0} u(\eta)\sin\left(\left(n - \tfrac{1}{2}\right)\pi\eta\right)d\eta\right)\sin\left(\left(n - \tfrac{1}{2}\right)\pi y\right).$$

Let us write

$$u(y) = \sum_{n=1}^{\infty} a_n\sqrt{2}\sin\left(\left(n - \tfrac{1}{2}\right)\pi y\right), \quad (2)$$

where

$$a_n \equiv \sqrt{2}\int_{-1}^{0} u(\eta)\sin\left(\left(n - \tfrac{1}{2}\right)\pi\eta\right)d\eta.$$

Since $\{\sqrt{2}\sin\left(\left(n - \frac{1}{2}\right)\pi y\right)\}_{n=1}^{\infty}$ is an infinite set of eigenfunctions of a Sturm–Liouville problem, the set then forms a complete and othonormal basis for $L^2[-1,0)$ (Coddington and Levinson [1955]). Thus we conclude that for all $u \in L^2[-1,0)$, the series (2) for u is always valid, which is equivalent to the expansion (*).

Note that when $y = 0$, U becomes

$$U = \frac{1}{2\pi i}\int_C \frac{1}{\Delta(\alpha)}[\alpha(T\alpha^2 + 1)(\cosh(\alpha(1+\eta)))]d\alpha,$$

which is zero, since the integrand is an odd function. The series representing U when $y \neq 0$ is (1), which is also zero for $y = 0$. Hence we may use (1) to represent U for all y. For all $u \in L^2[-1,0]$, (*) is equivalent to (2).

However, as one may observe, this does not explain the presence of zero term $-2\pi T\mu u_2(y)$ in (*) and the parameter μ. We only note that μ will be determined by the edge condition.

Consider the solution of the finite depth plane wavemaker problem can be written as

$$\psi(x,y)=\sum_{n=1}^{\infty}\chi_n(x)\,\widetilde{u}_n(y),$$

where $u(y)=\sum_{n=1}^{\infty}\widetilde{u}_n(y)$ is the expansion described as in (*), and the solution of the finite depth fluid outside a cylindrical wavemaker problem has the form

$$\varphi(r,z)=\sum_{n=1}^{\infty}\chi_n(x)\,\widetilde{u}_n(z),$$

where $u(z)=\sum_{n=1}^{\infty}\widetilde{u}_n(z)$ is the series expansion in (*). This explains the connection between the expansion theorem and the desired solutions. More detailed description of the solving process and interpretation shall be discussed in another paper.

(2). Expansion theorem for infinite depth

Theorem 0.2. For an arbitrary smooth function $f(z)$, $z\in(-\infty,0)$, there is an expansion in following form

$$f(z)=-\frac{2}{\pi}\int_{-\infty}^{0}f(\eta)\int_{0}^{\infty}\frac{\left[\alpha\left(1-T\alpha^2\right)\cos\alpha z+\omega^2\sin\alpha z\right]\left[\alpha\left(1-T\alpha^2\right)\cos\alpha\eta+\omega^2\sin\alpha\eta\right]}{\alpha^2\left(1-T\alpha^2\right)^2+\omega^4}d\alpha d\eta$$
$$-2\omega^2\int_{-\infty}^{0}\frac{e^{k_0(z+\eta)}}{1+3Tk_0^2}f(\eta)\,d\eta$$
$$+T\mu\left\{2\int_{0}^{\infty}\frac{\alpha\left[\alpha\left(1-T\alpha^2\right)\cos\alpha z+\omega^2\sin\alpha z\right]}{\alpha^2\left(1-T\alpha^2\right)^2+\omega^4}d\alpha+\frac{2\pi k_0e^{k_0z}}{1+3Tk_0^2}\right\},\quad(**)$$

where μ is an arbitrary parameter.

Proof. Consider $\mathcal{L}$ to be a differential operator defined on a Hilbert space H, $\widetilde{x}$ and $\widetilde{\xi}$ denote the vectors in H, and G is the Green's function such that $(\mathcal{L}-\lambda)G=\delta(\widetilde{\xi}-\widetilde{x})$. Then by Stakgold [1979], the following equation is always valid:

$$-\tfrac{1}{2\pi i}\textstyle\int_{C_\infty}G(\widetilde{x},\widetilde{\xi},\lambda)d\lambda=\delta(\widetilde{x}-\widetilde{\xi}),\quad(3)$$

where $\lambda \in \mathbb{C}$, and C_∞ is a circular contour rotating counterclockwise and centered at 0 with radius R approaching ∞. Now in our case, consider a Green's function $G(z,\zeta,\lambda)$ satisfying that

$$\begin{aligned} &G_{\zeta\zeta} - \lambda G = \delta(z-\zeta), \quad -\infty < \zeta, z < 0 \\ &-\omega^2 G + (1+T\lambda)G_\zeta = 0, \quad \zeta = 0; \\ &G_\zeta \longrightarrow 0 \text{ as } \zeta \longrightarrow -\infty. \end{aligned}$$

It is easy to find that

$$\begin{aligned} &G(\zeta < z) = \check{g}(\zeta, z, \lambda) = -\tfrac{e^{\sqrt{\lambda}\zeta}}{\sqrt{\lambda}} \times \tfrac{\sqrt{\lambda}(1+T\lambda)\cosh\sqrt{\lambda}z + \omega^2 \sinh\sqrt{\lambda}z}{\sqrt{\lambda}(1+T\lambda)-\omega^2}, \\ &G(\zeta > z) = \check{g}(z, \zeta, \lambda). \end{aligned}$$

Then by (3), we have

$$-\tfrac{1}{2\pi i}\int_{C_\infty} \tfrac{-e^{\sqrt{\lambda}\zeta}}{\sqrt{\lambda}} \times \tfrac{\sqrt{\lambda}(1+T\lambda)\cosh\sqrt{\lambda}z + \omega^2\sinh\sqrt{\lambda}z}{\sqrt{\lambda}(1+T\lambda)-\omega^2} d\lambda = \delta(z-\zeta).$$

Notice that there is a branch cut from $\lambda = 0$ along the positive real axis, and that G has two poles Ω^2 and $\bar{\Omega}^2$, where Ω and $\bar{\Omega}$ are the complex roots of $\alpha(T\alpha^2+1) - \omega^2 = 0$. Consider the contour C_0 traverses from $\mathrm{Re}\lambda = \infty$ along the branch cut with $\mathrm{Im}\lambda$ slightly negative, and to $\mathrm{Re}\lambda = \infty$ along the branch cut with $\mathrm{Im}\lambda$ slightly positive. It follows that

$$\tfrac{1}{2\pi i}\int_{C_\infty \cup C_0} \tfrac{e^{\sqrt{\lambda}}}{\sqrt{\lambda}} \times \tfrac{\sqrt{\lambda}(1+T\lambda)\cosh\sqrt{\lambda}z + \omega^2\sinh\sqrt{\lambda}z}{\sqrt{\lambda}(1+T\lambda)-\omega^2} d\lambda = -\operatorname{Res}_{\lambda=\Omega^2} G - \operatorname{Res}_{\lambda=\bar{\Omega}^2} G, \qquad (4)$$

where the residue values at Ω^2 and $\bar{\Omega}^2$ are obtained as $-\frac{2\omega^2}{1+3T\bar{\Omega}^2}e^{\bar{\Omega}(z+\zeta)}$, and $-\frac{2\omega^2}{1+3T\bar{\Omega}^2}e^{\Omega(z+\zeta)}$ respectively. So (4) becomes

$$-\tfrac{1}{2\pi i}\int_{C_\infty} G d\lambda = -\tfrac{1}{2\pi i}\int_{-C_0} \tfrac{-e^{\sqrt{\lambda}\zeta}}{\sqrt{\lambda}} \times \tfrac{\sqrt{\lambda}(1+T\lambda)\cosh\sqrt{\lambda}z + \omega^2\sinh\sqrt{\lambda}z}{\sqrt{\lambda}(1+T\lambda)-\omega^2} d\lambda + 2\omega^2\left(\tfrac{e^{\Omega(z+\zeta)}}{1+3T\Omega^2} + \tfrac{e^{\bar{\Omega}(z+\zeta)}}{1+3T\bar{\Omega}^2}\right). \qquad (5)$$

Now let $\lambda = \alpha^2$ in the integral on $-C_0$, and also rotate the lower branch of $-C_0$ clockwise to the negative real axis, while the upper branch along the positive real axis, indented above k_0 and below $-k_0$. Then

$$\begin{aligned} &-\tfrac{1}{2\pi i}\int_{-C_0} \tfrac{-e^{\sqrt{\lambda}\zeta}}{\sqrt{\lambda}} \times \tfrac{\sqrt{\lambda}(1+T\lambda)\cosh\sqrt{\lambda}z + \omega^2\sinh\sqrt{\lambda}z}{\sqrt{\lambda}(1+T\lambda)-\omega^2} d\lambda \\ &= \tfrac{-1}{\pi i}\int_{-\infty}^{\infty} (-e^{\alpha\zeta}) \tfrac{\alpha(1+T\alpha^2)\cosh\alpha z + \omega^2\sinh\alpha z}{\alpha(1+T\alpha^2)-\omega^2} d\alpha + \left(\tfrac{-1}{\pi i}\right)\left(-2\pi i \operatorname{Res}_{\alpha=\bar{\Omega}} \check{G}\right) \\ &= \tfrac{-1}{\pi i}\int_{-\infty}^{\infty} (-e^{\alpha\zeta}) \tfrac{\alpha(1+T\alpha^2)\cosh\alpha z + \omega^2\sinh\alpha z}{\alpha(1+T\alpha^2)-\omega^2} d\alpha + 2\operatorname{Res}_{\alpha=\bar{\Omega}} \check{G}, \end{aligned}$$

where $\check{G} = (-e^{\alpha\zeta}) \cdot \frac{\alpha(1+T\alpha^2)\cosh\alpha z + \omega^2\sinh\alpha z}{\alpha(1+T\alpha^2)-\omega^2}$. Note that we have a negative residue

since in the process of integration we rotate the path of integration clockwise across the pole $\bar{\Omega}$ of $-\check{G}$ in the third quadrant. The above residue is found as $-\frac{\omega^2 e^{\bar{\Omega}(z+\zeta)}}{1+3T\bar{\Omega}^2}$, and (5) becomes

$$-\frac{1}{2\pi i}\int_{C_\infty} G d\lambda = \frac{-1}{\pi i}\oint_{-\infty}^{\infty}(-e^{\alpha\zeta})\frac{\alpha(1+T\alpha^2)\cosh\alpha z+\omega^2\sinh\alpha z}{\alpha(1+T\alpha^2)-\omega^2}d\alpha + \frac{2\omega^2 e^{\Omega(z+\zeta)}}{1+3T\Omega^2}. \quad (6)$$

Again, rotate the considered contour clockwise to the imaginary axis, then

$$\begin{aligned}
&-\frac{1}{\pi i}\oint_{-\infty}^{\infty}(-e^{\alpha\zeta})\frac{\alpha(1+T\alpha^2)\cosh\alpha z+\omega^2\sinh\alpha z}{\alpha(1+T\alpha^2)-\omega^2}d\alpha \\
&= -\frac{1}{\pi i}\int_{\infty}^{0}\check{G}(z,\zeta,-i\alpha)d(-i\alpha) - \frac{1}{\pi i}\int_{\infty}^{0}\check{G}(z,\zeta,i\alpha)d(i\alpha) + 2\,\mathrm{Res}_{\alpha=\Omega}\check{G} + 2\,\mathrm{Res}_{\alpha=k_0}\check{G} \\
&= \frac{i}{\pi i}\int_{0}^{\infty} e^{-i\alpha\zeta}\frac{(-i\alpha)(1-T\alpha^2)\cos\alpha z - i\omega^2\sin\alpha z}{(-i\alpha)(1-T\alpha^2)-\omega^2}d\alpha + \frac{i}{\pi i}\int_{0}^{\infty} e^{i\alpha\zeta}\frac{(i\alpha)(1-T\alpha^2)\cos\alpha z + i\omega^2\sin\alpha z}{(i\alpha)(1-T\alpha^2)-\omega^2}d\alpha \\
&\qquad +2\left(\mathrm{Res}_{\alpha=\Omega}\check{G} + 2\,\mathrm{Res}_{\alpha=k_0}\check{G}\right) \\
&= \frac{i}{\pi}\int_{0}^{\infty}[\alpha(1-T\alpha^2)\cos\alpha z+\omega^2\sin\alpha z]\left[\frac{e^{-i\alpha\zeta}}{i\alpha(1-T\alpha^2)+\omega^2}+\frac{e^{i\alpha\zeta}}{i\alpha(1-T\alpha^2)-\omega^2}\right]d\alpha \\
&\qquad +2\omega^2\left(\frac{-e^{\Omega(z+\zeta)}}{1+3T\Omega^2}+\frac{-e^{k_0(z+\zeta)}}{1+3Tk_0^2}\right) \\
&= -\frac{2}{\pi}\int_{0}^{\infty}\frac{[\alpha(1-T\alpha^2)\cos\alpha z+\omega^2\sin\alpha z][\alpha(1-T\alpha^2)\cos\alpha\zeta+\omega^2\sin\alpha\zeta]}{\alpha^2(1-T\alpha^2)^2+\omega^4}d\alpha \\
&\qquad -2\omega^2\left(\frac{e^{\Omega(z+\zeta)}}{1+3T\Omega^2}+\frac{e^{k_0(z+\zeta)}}{1+3Tk_0^2}\right). \quad (7)
\end{aligned}$$

Notice that we cross two poles of $\check{G}$ clockwise this time. So finally, by (3), (6) and (7), we have

$$\begin{aligned}
-\frac{1}{2\pi i}\int_{C_\infty} G d\lambda &= -\frac{2}{\pi}\int_{0}^{\infty}\Big[[\alpha(1-T\alpha^2)\cos\alpha z+\omega^2\sin\alpha z] \\
&\quad\times[\alpha(1-T\alpha^2)\cos\alpha\zeta+\omega^2\sin\alpha\zeta]/[\alpha^2(1-T\alpha^2)^2+\omega^4]\Big]d\alpha - 2\omega^2\frac{e^{k_0(z+\zeta)}}{1+3Tk_0^2} \\
&= \delta(z-\zeta),
\end{aligned}$$

or for any arbitrary smooth $f(z)$,

$$\begin{aligned}
f(z) = -\frac{2}{\pi}&\int_{-\infty}^{0} f(\zeta)\int_{0}^{\infty}\Big[[\alpha(1-T\alpha^2)\cos\alpha z+\omega^2\sin\alpha z] \\
&\times[\alpha(1-T\alpha^2)\cos\alpha\zeta+\omega^2\sin\alpha\zeta]/[\alpha^2(1-T\alpha^2)^2+\omega^4]\Big]d\alpha d\zeta \\
&-2\omega^2\frac{e^{k_0 z}}{1+3Tk_0^2}\int_{-\infty}^{0} f(\zeta)e^{k_0\zeta}d\zeta.
\end{aligned}$$

Let us also look at the integral

$$\mathbf{I} = -i \int_0^\infty \frac{\alpha e^{-\alpha z}}{\alpha(1+T\alpha^2)-\omega^2} d\alpha, \quad (8)$$

which integrates on the contour from 0 to ∞ and indented below k_0. By rotating the contour to the positive imaginary axis, we find

$$\mathbf{I} = \int_0^\infty \frac{\alpha e^{-i\alpha z}}{\alpha(1-T\alpha^2)+i\omega^2} d\alpha + \frac{2\pi k_0}{1+3Tk_0^2} e^{k_0 z}; \quad (9)$$

and by rotating the original contour for $\mathbf{I}$ toward the negative imaginary axis,

$$\mathbf{I} = -\int_0^\infty \frac{\alpha e^{i\alpha z}}{\alpha(1-T\alpha^2)-i\omega^2}. \quad (10)$$

Combining (9) and (10), we realize that

$$\begin{aligned} Q(z) &= \int_0^\infty 2\alpha \left[\frac{e^{-i\alpha z}}{\alpha(1-T\alpha^2)+i\omega^2} + \frac{e^{i\alpha z}}{\alpha(1-T\alpha^2)-i\omega^2} \right] d\alpha + \frac{2\pi k_0}{1+3Tk_0^2} e^{k_0 z} \\ &= 2\int_0^\infty \frac{\alpha[\alpha(1-T\alpha^2)\cos\alpha z + \omega^2 \sin\alpha z]}{\alpha^2(1-T\alpha^2)^2+\omega^4} d\alpha + \frac{2\pi k_0}{1+3Tk_0^2} e^{k_0 z} = 0. \end{aligned}$$

Multiplying the above equation by a parameter $T\mu$ and adding it to the expression in (8), we obtain

$$\begin{aligned} f(z) = -\frac{2}{\pi} \int_{-\infty}^0 f(\zeta) \int_0^\infty \Big[& [\alpha(1-T\alpha^2)\cos\alpha z + \omega^2 \sin\alpha z] \\ & \times [\alpha(1-T\alpha^2)\cos\alpha\zeta + \omega^2 \sin\alpha\zeta]/[\alpha^2(1-T\alpha^2)^2+\omega^4] \Big] d\alpha d\zeta \\ & - \frac{2\omega^2}{1+3Tk_0^2} e^{k_0 z} \int_{-\infty}^0 f(\zeta) e^{k_0\zeta} d\zeta \\ & + T\mu 2 \int_0^\infty \frac{\alpha[\alpha(1-T\alpha^2)\cos\alpha z + \omega^2 \sin\alpha z]}{\alpha^2(1-T\alpha^2)^2+\omega^4} d\alpha + T\mu \frac{2\pi k_0}{1+3Tk_0^2} e^{k_0 z}, \end{aligned}$$

This concludes the proof of Rhodes–Robinson's expansion theorem for infinite depth.

Finally, if we consider the solution ψ_∞ of the infinite depth plane wavemaker problem, it can be shown as

$$\psi_\infty(x,y) = \int_0^\infty Q_1(\alpha,y)\,\chi_1(\alpha,x)\,d\alpha + Q_2(y)\,\chi_2(x),$$

where $\int_0^\infty Q_1(\alpha,y)\,d\alpha + Q_2(y)$ is the integral expansion in (**); and the solution φ_∞ of the infinite depth fluid outside the cylindrical wavemaker problem is

$$\varphi_\infty(r,z) = \int_0^\infty Q_1(\alpha,z)\, R_1(\alpha,r)\, d\alpha + Q_2(z)\, R_2(r),$$

and again, $\int_0^\infty Q_1(\alpha,z)\, d\alpha + Q_2(z)$ comes from the expansion form of equation (**). Therefore, we may obtain the solutions by simply assuming the expressions of ψ_∞ and φ_∞ as above. More details about finding solutions as well as the interpretation of the solutions and the zero parts of these expansion theorems will be shown in another paper.

IV. REFERENCES.

(1) Coddington, E. A. and Levinson, N. *Theory of ordinary differential equations* (McGraw-Hill, New York, Toronto and London, 1955).

(2) Evans, D. V. The effect of surface tension on the reflection of water waves by a plane vertical barrier, *Proc. Cambridge Philos. Soc.* **64** (1968), 833-847.

(3) Havlock, T. H. Forced surface waves on water, *Philos. Mag.* 8 (1929), 569-576.

(4) Hocking, L. M. The damping of capillary-gravity waves at a rigid boundary, *J. Fluid Mech.* **179** (1987), 253-266.

(5) Rhodes-Rhobinson, P. F. On the forced surface waves due to a vertical wavemaker in the presence of surface tension, *Proc. Cambridge Philos. Soc.* 70 (1971), 323-337.

(6) Stakgold, I. *Green's functions and boundary value problems* (John Wiley & Sons, New York, Chichester, Brisbane and Toronto, 1979).

V. FIGURES

Figure 1.

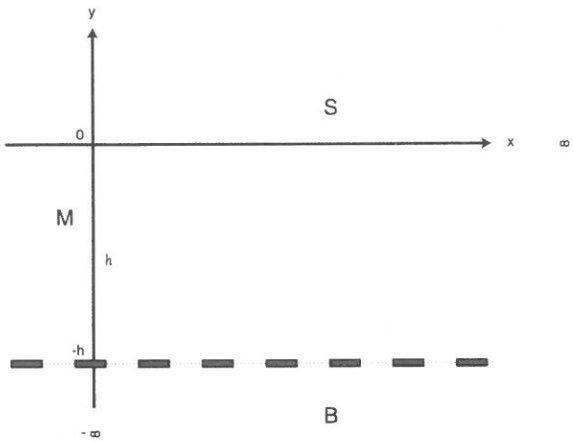

The Figure for Formulation (A)

Figure 2.

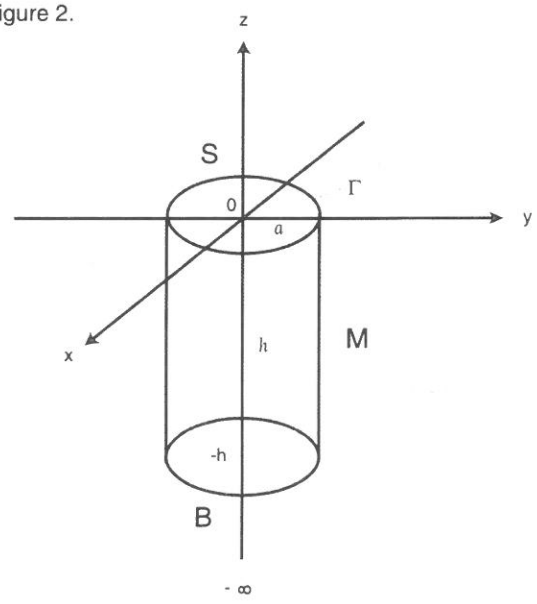

The Figure for Formulation (B)

垂直造波器所造毛細重力波問題中展開式定理之嚴密證明

葉 乃 實
輔仁大學數學系

摘 要

此論文之目的，在於將羅茲-羅賓遜 [1971] 所提出垂直造毛所造毛細重力波問題中展開式定理，給予嚴格的證明。在此也對展開式定理的用法，予以簡單的闡述。

關鍵詞：毛細重力波，展開式定理，邊界條件。

Low Power Programming Design for a Microcomputer 8051 System Powered by Solar Cells

Ying-Wen Bai and Cheng-Lun Chang

Department of Electronic Engineering
Fu Jen Catholic University
Taipei, Taiwan 242, R.O.C.
bai@ee.fju.edu.tw

Abstract

To extend the recharge cycle of a microcomputer system with a limited energy source, such as solar cells, in this paper we propose a low power programming design in order to reduce the power consumption. In our experiment, there are five testing programs with different typical functions of each version in the module of an 8051 assembly, a mixed mode of the assembly and C language, and a pure C language design for comparison testing. Each version of the five programs is surveyed to evaluate the execution time, the HEX codes, the clock cycles and the current consumption. Overall, the experimental results show that we have obtained a scalable energy reduction of from one to nine times, based on the usage percent of the assembly language. This improvement also provides the potential to extend the operation time or recharge cycle for other similar microcomputer systems powered by solar cells.

Key Words: Microcomputer System, Low Power Programming, Solar Cells.

1. Introduction

Many researchers have already investigated power consumption of microcomputer hardware, providing substantial improvements [1,2]. On the other hand, in terms of software, power management methods and low power programming methods are also important factors, both to reduce power consumption by increasing the management efficiency, and to reduce the execution time. Because low power programming techniques can be used with different hardware platforms, therefore when one considers the recharge cycle of a very limited battery power source, software design can also be important for portable information applications. Because a battery has very limited amount of energy, the battery of a portable information system must be frequently recharged. So with the help of a more efficient programming language that consumes less power, the battery recharge cycle can be extended [3-6].

In order to learn more about the relationship between power consumption and the programming technique utilized, we used a microcomputer 8051 system powered by solar cells as the experimental platform. For each of the five testing programs, we designed three different versions, an 8051 assembly, a mixed mode of assembly and C language, and a pure C language. Thus we study the characteristics of the five testing programs by surveying each version with respect to the execution time, HEX codes, clock cycles, current consumption and energy dissipation (W-Sec.). The experimental platform also shows the results that provide us with principles that can be used to obtain low power programming and shorter execution time [7,8].

The rest of this paper is organized as follows. In Section 2, we present Amdahl's Law as the comparison index of the improvement proportion by using the testing programs of a microcomputer 8051 system [9,10]. In Section 3, detailed characteristics of the testing programs, their functions and their flowcharts are presented. In Section 4, experiment results and a comparison

of testing programs between an 8051 assembly, a mixed mode of assembly and a pure C language are shown. In Section 5, we discuss the queueing model for power charging and discharging behavior of a rechargeable battery powered by solar cells, showing that by using low power programming design, the operation time can be extended. Finally, in Section 6, we provide conclusions.

2. Amdahl's Law for Performance Comparison

Amdahl's Law [9,10] gives us a quick way to find the speedup of a computer system design from an enhancement, depending on two factors:

1. The fraction of the computation time in the original unenhanced machine that can be converted to take advantage of the enhancement.
2. The improvement gained by the enhanced execution mode; that is, how much faster the task would run if the enhanced mode were used for the entire program.

The execution time using the original unenhanced machine with the enhanced mode will be the time spent using the unenhanced portion of the machine, plus the time spent using the enhancement. The overall speedup is the ratio of the execution times [9,10]:

$$Speedup_{overall} = \frac{Execution\ time_{old}}{Execution\ time_{new}} = \frac{1}{(1 - Fraction_{enhanced}) + \frac{Fraction_{enhanced}}{Speedup_{enhanced}}} \quad (1)$$

We can transfer the overall "Speedup" of Amdahl's Law from Eq. (1) as an overall "Improvement Proportion", which can be composed of the following: execution time, current consumption, and power consumption and energy consumption:

$$\mathrm{Im}\,provement_{overall} = \frac{1}{(1 - \mathrm{Pr}\,oportion_{enhanced}) + \frac{\mathrm{Pr}\,oportion_{enhanced}}{\mathrm{Im}\,provement_{enchanced}}} \quad (2)$$

3. Testing Programs and Their Flowcharts

In general, an assembly language computer program has a faster execution time, and a lower program code size, providing the potential for lower power consumption due to the higher controllability of computer hardware by utilizing the natural characteristics of assembly language. The main disadvantages of assembly language programs are that they are not easy to design, implement and maintain. On the other hand, the C version of the program has the characteristics of a typical high-level programming language in that it is easy to design, implement and maintain. However, it has a longer execution time, and thus has the disadvantage of the potential for higher power consumption. If we can integrate the characteristics of the high-level and the assembly program languages, then the mixed mode of testing programs will provide a scalable ability in execution time and power consumption.

To demonstrate the different characteristics of the testing programs, we use 8051 single chip microcomputer systems powered by solar cells as the experimental platform for the five testing programs. We use the three versions of the five testing programs: a pure assembly module, a mixed module of C and assembly, and a pure C module respectively. Each of these different versions is used to investigate the scalable characteristics of low power programming [4-8].

Testing program 1 uses the instructions "RRC" and "RLC" to manipulate data in assembly, ">>" and "<<" in C language. Testing program 2 computes data by using "ADD" and "DA" in assembly and typical additive statements in C language. Testing program 3 retrieves data from the table that is established in the testing program by assembly and C language. Then testing programs 4 and 5 emphasize the computation ability without data input/output operations. In these five testing programs, program 1 emphasizes input and output data; program 2 emphasizes the computing data before input/output; program 3 emphasizes the retrieving of data from a table,

and the resulting input or output data; and programs 4 and 5, instead of emphasizing the input and output, emphasize "computation". We use different testing program structures for measurement of the same software characteristics in order to explore the scalability of the improvement proportion from programming [8].

3.1 Testing Program 1 (The LED Shifts Left and Right)

Testing program 1 as shown in Fig. 1 contains a function that can control the LED display by shifting the LED to either left or right. When this program is being used, it outputs data to port P1 of the 8051 microcomputer system, turning on the LED from P1.0 to P1.7 and then forming loops.

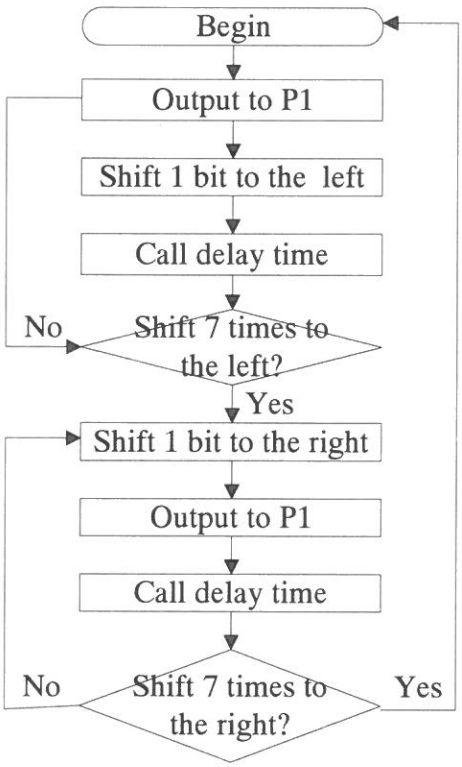

Fig.1 Testing program 1 flowchart

In assembly language, we use the instructions "RLC" and "RRC" to shift the LED to the left or right, and use the instruction "MOV" to output the data to a display. The subprogram "DELAY" generates a delay time between the two states, "on" and "off". Fig. 2 shows the assembly language source code of testing program 1.

```
        CLR     P2.0
START:
        MOV     R2,#08H
LOOP:
        RLC     A
        MOV     P1,A
        CALL    DELAY
        DJNZ    R2,LOOP
        MOV     R2,#08H
LOOP1:
        SETB    P2.0
        RRC     A
        MOV     P1,A
        CALL    DELAY
        DJNZ    R2,LOOP1
        CLR     P2.0
        JMP     START
DELAY:
        MOV     R3,#20
D1:
        MOV     R4,#20
D2:
        MOV     R5,#40
        DJNZ    R5,$
        DJNZ    R4,D2
        DJNZ    R3,D1
        RET
```

Fig. 2 The assembly language source codes of testing program 1

In C language, we use the statement c=c<<1 and c=c>>1 to control an LED display that shifts to the left or right. The variable "c" represents the output data. We use the statement "for" to control the number of times that shift the bit pattern of "c". Fig. 3 is the C language source code of testing program 1.

```
delay(idata int   n)
{
   idata int i;
   for(i=0; i<n; i++ );
}
main()
{
   idata char c;
   idata int i;
   c = 0x01;
   P2.0 =0;

   while(1)
   {
      for( i=0; i<7 ; i++ )
      {
         P1 = ~c;
         delay(0x3e80);
         c = c<<1;
      }
      for( i=0; i<7 ; i++ )
      {
         P1 = ~c;
         delay(0x3e80);
         c = c>>1;
      }
   }
}
```

Fig. 3 Testing program 1 C language source codes

In addition, we use a subprogram DELAY with 8051 assembly language as a substitute for C language and to provide the mixed mode version to investigate the characteristics of this testing program.

3.2 Testing Program 2(Timer)

Testing program 2 as shown in Fig. 4 uses the I/O port P2.0~P2.3 of the 8051 microcomputer system to control a 7-segment LED display for 0~9, and P2.4~P2.7 for decimals. This program shows numbers between 00 and 99, and then repeats the operation in looping.

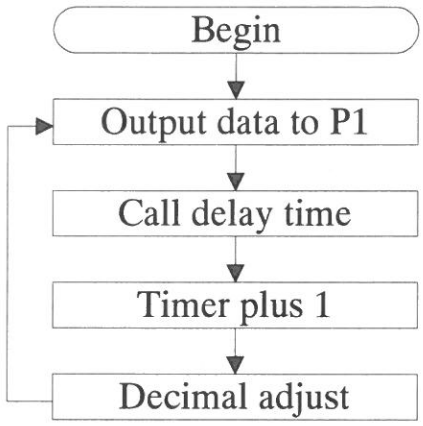

Fig. 4 Testing program 2 flowchart

In assembly language, we add the value "one" to the register by using the instruction "ADD". However, because the registers contain hexadecimal code, we convert hexadecimal to decimal by using the instruction "DA" in order to show the decimal data, and output that data to the 7-segment. Then we use the subprogram "DELAY" between two states to allow for delay time.

In C language, we use two "for" statements to count numbers. Because we show the decimal data, we need to use the statement "c=c+6" to change hexadecimals to decimals. In the design of the mixed mode version, we substitute an assembly language version of the subprogram "DELAY".

3.3 Testing Program 3(5×7 Dot Matrix's LED)

Each row of the dot matrix's LED are scanned by the I/O port P2.0~P2.4 and by the 8051 microcomputer system, and output data is scanned by the I/O port P1.0~P1.6 from the system. The program shows symbols from 0 to 9 and A to H, then repeats the operation. Fig. 5 shows the software flowchart of testing program 3.

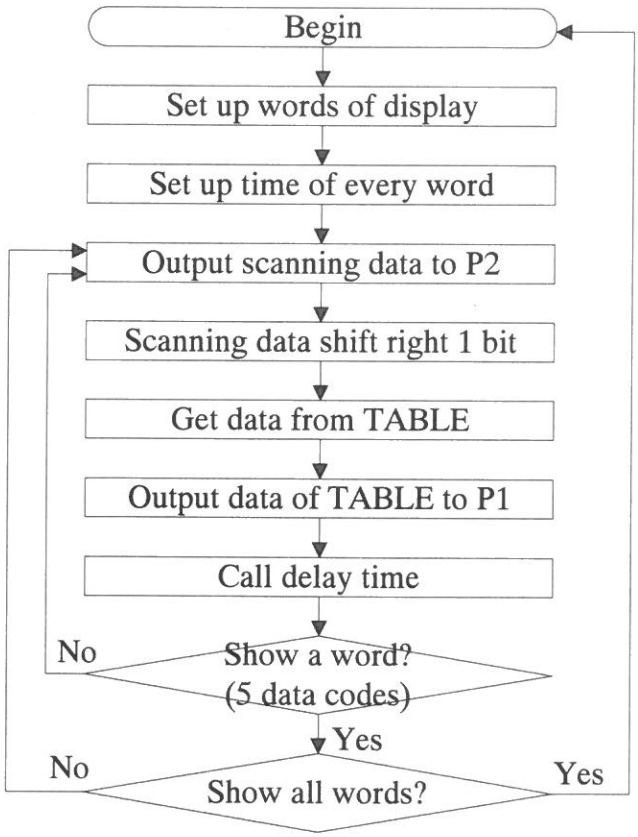

Fig. 5 Testing program 3 software flowchart

When using the mixed mode of assembly and C language, we establish codes of 0~9 and A~H in "TABLE". In the assembly version, we use the instruction "MOVC" to get data into the "TABLE" and then output the data to port P1. The instructions "INC" add "1" and can set flags. In other words, the instruction "INC" gets the next data code. The C language program uses three "for" statements to get data and show data.

3.4 Testing Program 4 (Prime Numbers Between 1 and 100)

We use an 8051 microcomputer system to control the input/output, simple computation and table search for the above three programs. In order to

understand the different characteristics of each programming language, testing programs 4 and 5 are used only for computing data, and not for input/output in order to determine the effects on computation performance in the testing program. Fig. 6 shows the flowchart of testing program 4.

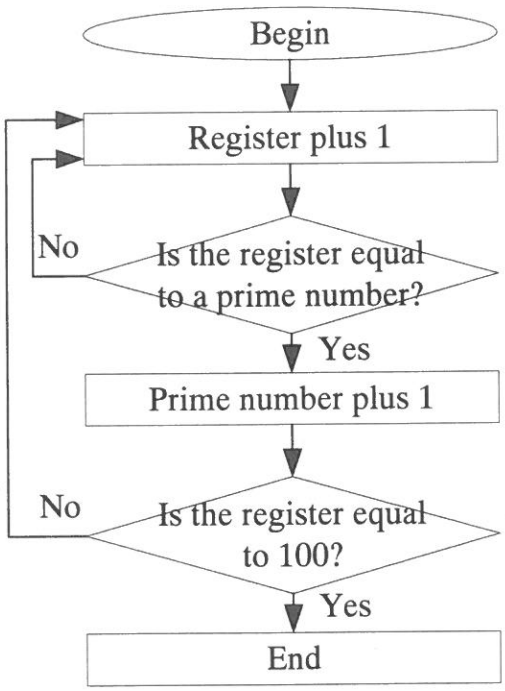

Fig. 6 Testing program 4 flowchart

The testing program 4 obtains prime numbers between 1 and 100. In its assembly version, it uses the instruction "DIV" and "CJNE" to find prime numbers between 1 and 100. The register R3 saves variables of the prime numbers between 1 and 100.

When using C language, we use the "division" statement to find prime numbers. The register variable "k" saves remainders from dividing two numbers, and the statement "if" checks whether the remainder is equal to zero or not. The register l saves the prime numbers between 1 and 100.

In the mixed mode version, we use assembly code to substitute one of C

language the "for" statements that provide scalable characteristics for the middle part of the program's performance.

3.5 Testing Program 5 (Multiply Two 5*5 Matrices)

Testing program 5, as shown in Fig. 7, emphasizes only data computation, but without input/output. "SEG1" and "SEG2" save two 5*5 matrices separately. In the assembly, we use the instruction "MOVC" to get the data from the two matrices separately, and we save that data to the register variables "A" and "B", respectively. Then we multiply two variables in the registers and get an answer. In the C language design, we get the answer by using "for" statements.

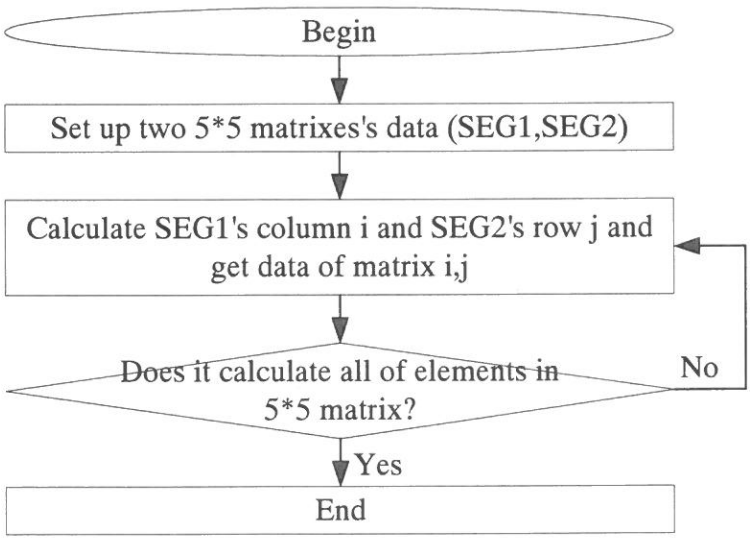

Fig. 7 Testing program 5 flowchart

In the mixed mode version, again, we use assembly code for the "for" statement portion of the testing program that computes each element of the looping matrices.

4. EXPERIMENTAL DATA OF THE FIVE TESTING PROGRAMS

Since the five testing programs are implemented by different

programming language versions, the execution performance can be different. Therefore, in this section, we investigate the differences in execution time, HEX codes, clock cycles, current consumption and energy (W-sec.) dissipation.

4.1 Execution Time and Other Characteristics

From Table 1 we can see that the execution time when using assembly language is shorter than when using C language. Therefore, using assembly language will reduce the power consumption.

Table 1 Execution time of the five testing programs

	Program 1	Program 2	Program 3	Program 4	Program 5
Assembly	0.53 seconds	6.1 seconds	75 seconds	27 seconds	13.1 seconds
C language	5.15 seconds	69 seconds	531.6 seconds	332 seconds	28 seconds
Mixed mode of assembly and C language	0.46 seconds	6.1 seconds	76 seconds	28 seconds	16.1 seconds

By examining the above execution times, we can clearly obtain the improvement proportion for the execution time by using Eq. (2) in Section 2, which may be shown as follows.

For testing program 1, we have

$$\text{Pr}\,oportion_{\,enhanced} = (5.15-0.46)/5.15 = 0.911$$

$$\text{Im}\,provement_{\,enhanced} = 5.15/0.53 = 9.717$$

The overall improvement proportion of testing program 1 can be shown by Eq(3)

$$\text{Improvement}_{overall} = \frac{1}{(1 - \text{Proportion}_{enhanced}) + \frac{\text{Proportion}_{enhanced}}{\text{Improvement}_{enhanced}}} = 5.464 \quad (3)$$

By going through the same procedure for testing programs 2 to 5, we can obtain the average improvement proportion of execution times, as shown in Table 2.

Table 2 Average improvement proportions of the execution times for the five testing programs

	Program 1	Program 2	Program 3	Program 4	Program 5	Average improvement proportion
Improvement proportion	5.464	5.917	3.788	6.329	1.292	4.558

By going through a similar procedure, we obtain Fig. 8, showing the average improvement proportion for the execution time, the HEX codes, the clock cycles, and the current consumption and energy dissipation (W-sec.).

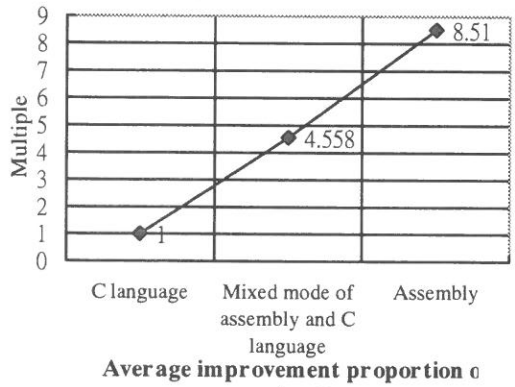

Average improvement proportion o running time

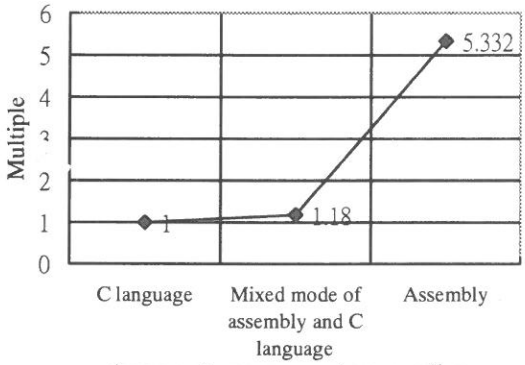

Average improvement proportion o HEX codes

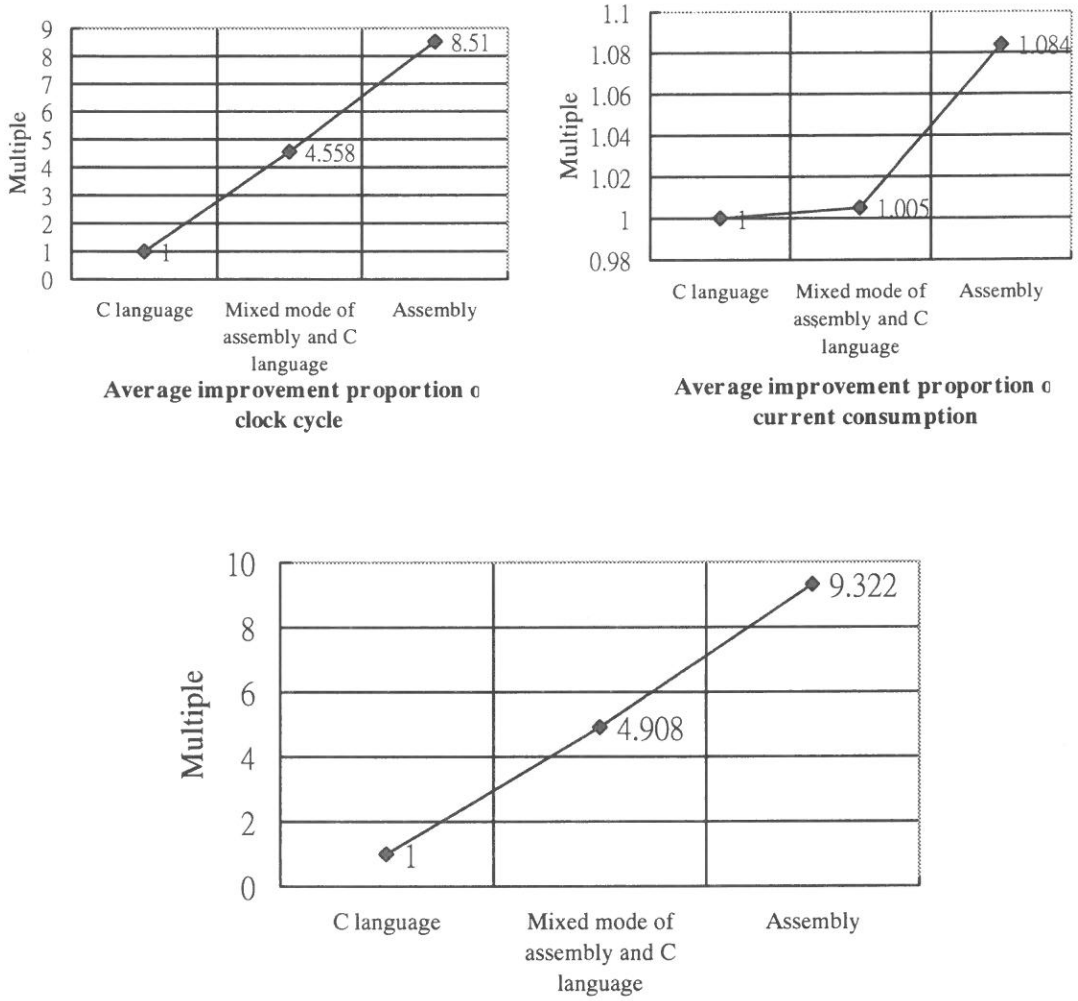

Fig. 8 Scalable relationship of the average improvement proportion for the five testing programs

5. Queueing Model for the Power Charging and Discharging Behavior of a Dual Rechargeable Battery Used in Low Power Programming Design

As for the discharging capability of typical microcomputers in references [1,2], currently, according to its specifications, an 8051 microcomputer consumes less than 6W. As for the charging capability of typical solar cells in references [11-13], their power generation efficiency has increased more than 20 percent in the last five years. From the typical characteristics of typical solar cells, we can derive the power generation density (W/cm^2), as shown in Table 3. Currently, the surface area of a portable microcomputer is around $100 cm^2$, which is close to the physical size of a handset. When one combines the area of the handset with the power generation efficiency, we find that the average power generation of typical solar cells under sunshine is at about the level of 0.384W shown in Table 3.

Table 3 Power densities of typical solar cells.

Type model	Size , cm			Power		Power density
	Width	Length	Thickness	V_{op}, v	I_{op}, mA	mW/cm^2
SP 1506	15.24	5.50	0.235	7.5	48.0	4.30
SP 1508	15.24	7.62	0.235	7.5	60.0	3.88
SP 1512-2A	15.24	15.24	0.235	7.5	130.0	4.20
SP 1512-2B	15.24	15.24	0.235	7.5	106.0	3.42
SP 1530	15.24	29.00	0.235	7.5	200.0	3.40
					Average	3.84

Condition FL: 200 Lux, 25℃

Fig. 9 shows a typical design for a microcomputer powered by solar cells.

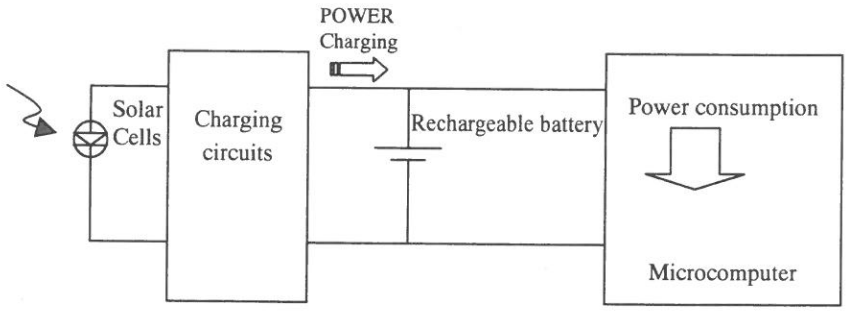

Fig.9 Typical design for a microcomputer powered by solar cells

The energy is generated by solar cells and is used to recharge the battery. Usually, the power generation should be greater than or equal to the power consumption, so that the microcomputer can work without exhausting its battery power. However, because power generation indoors can be less than power consumption, the microcomputer will work with a power exhaustion probability. Because a rechargeable battery provides the energy storage mechanism, the power generated from solar cells can be used to charge the rechargeable battery even if the machine is turned off. The stochastic behavior of power charging and discharging for the microcomputer operation can be modeled by a queueing model [15]. Previous results show that under certain operational conditions in a 24 hour period there is only a 0.46 hour operation time with a power exhaustion probability of less than 1% [16,17].

The equivalent model as shown in Fig. 10 is similar to a single queue with a single-server and a charge buffer, a Poisson energy arrival rate of λ, and an exponential energy departure rate of μ.

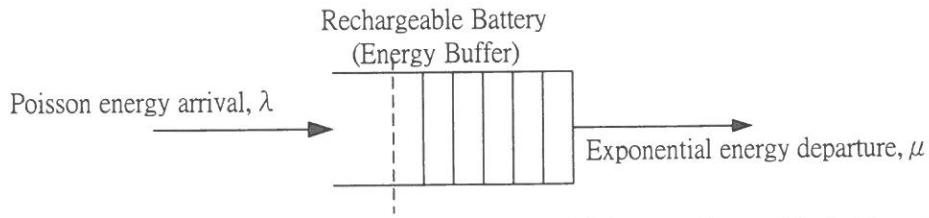

Fig. 10 Equivalent M/M/1 queueing model for a rechargeable battery

As noted in references [15-17], with respect to the static properties of the M/M/1 queue, the average rechargeable battery energy occupancy, and the probability of using up the energy of the rechargeable battery are readily determined once we find the probabilities of state P_n of the rechargeable battery. P_n represents the probability that there are n units of charges in the battery and P_0 represents the probability that there are zero units of charges in the battery. In other words, P_0 is the probability of using-up the energy in a rechargeable battery. If P_0 is small enough, then the solar cell powered microcomputer system can be acceptable from the power supply point of view.

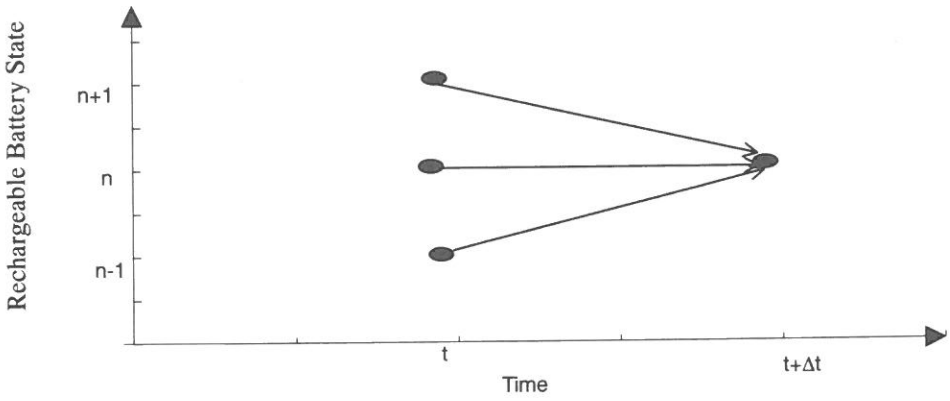

Fig.11 M/M/1 state-time diagram for the model of a rechargeable battery

Specifically, we assume that the charge arrival process to the rechargeable battery has a Poisson distribution, with a charge rate λ. If we assume the charge departure rate to be exponential, with a discharging rate μ, and then the state probability $P_n(t+\Delta t)$ means that there are n units of charge in the rechargeable battery at time (t+Δt). If one refers to the state-time diagram shown in Fig. 11, it is assumed that if the rechargeable battery is in state n at time t+Δt, and it can only have been in states n-1, n, or n+1 at time t. Each state probability is multiplied by the probability of charges arriving at state n in the intervening Δt units of time. We thus have a generating equation for $P_n(t+\Delta t)$,

$$\begin{aligned} P_n(\mathrm{t}+\Delta t) &= P_n(\mathrm{t})\left[(1-\lambda\Delta t)(1-\mu\Delta t)+\mu\Delta t\lambda\Delta t+O(\Delta t)\right] \\ &+ P_{n-1}(\mathrm{t})\left[(\lambda\Delta t)(1-\mu\Delta t)+O(\Delta t)\right] \\ &+ P_{n+1}(\mathrm{t})\left[(\lambda\Delta t)(1-\mu\Delta t)+O(\Delta t)\right] \end{aligned} \tag{4}$$

Since O(Δt) includes terms of orders $(\Delta t)^2$ and higher, the terms involving $(\Delta t)^2$ in Eq. (4) should be incorporated in O(Δt). Simplifying Eq. (4) by dropping O(Δt) terms and higher order terms, one can obtain $P_n(t)$ shown in Eq. (5) by solving differential-difference equations.

$$P_n(t) = \left(1 - \frac{\lambda}{\mu}\right)\left(\frac{\lambda}{\mu}\right)^n \left[1 - \sum_{k=0}^{\infty}\left(\frac{(\lambda t)^k e^{-\lambda t}}{k!} e^{-\mu t} \sum_{m=0}^{n+i+1+k}\left(\frac{\mu t}{m!}\right)^m\right)\right] \tag{5}$$

In taking the limit as t→∞, we see that the terms $e^{-(\lambda+\mu)tm}$ go to 0. Hence, when t→∞ the result is,

$$\lim_{t\to\infty} it\ P_n(t) = P_n = \left(1 - \frac{\lambda}{\mu}\right)\left(\frac{\lambda}{\mu}\right)^n \tag{6}$$

When λ/μ<1 we get a valid steady-state probability distribution, and when n=0 we obtain the power exhaustion probability P_0,

$$P_0 = 1 - \frac{\lambda}{\mu}, \qquad 0 \le \frac{\lambda}{\mu} < 1 \tag{7}$$

where λ is the charging rate for the power generation of the solar cells and μ is the discharging rate for the power consumption of a microcomputer system. Because a typical user is not using the microcomputer system all the time, the utilization of a microcomputer could be smaller than 100%. Hence, we can consider the utilization (u.t.) and then obtain an approximate equivalent power consumption rate as,

$$\hat{\mu} = (u.t.)\mu \tag{8}$$

In addition, because the solar cells can not generate power all day due to a lack of sunshine, the duty cycle of the generating power could be smaller than 100%. Hence, we can consider the duty cycle (d.c.), and then obtain an approximate equivalent power generation rate as

$$\hat{\lambda} = (d.c.)\lambda \tag{9}$$

If we rewrite Eq. (7) with the equivalent power consumption rate $\hat{\mu}$ and the power generation rate $\hat{\lambda}$, we obtain

$$P_0 = 1 - \frac{\hat{\lambda}}{\hat{\mu}} = 1 - \frac{(d.c.)\lambda}{(u.t.)\mu} \tag{10}$$

During daylight, the duty cycle (d.c.) can be assumed to have a typical value, for example, d.c. = 0.3. For the current technology level, from Eq. (4), if we assume $P_0 \leqq 0.01$, a very small probability for using up power, we can obtain Eq. (5),

$$u.t. \leq \frac{0.3\lambda}{0.99\mu} = \frac{0.3 \times 0.384W}{6W} = 1.92\% \tag{11}$$

When u.t. $\leqq$ 1.92%, that indicates that the microcomputer operation time can be 0.46 hours per day. Gradually, as technology improves, the ratio $\hat{\lambda}/\hat{\mu}$ will increase, and the operation time will be longer.

From Section 4.1, we get an average improvement proportion in energy that is 4.908 times the mixed mode design. In other words, we reduce the discharge rate (μ) by almost 5 times. Therefore, we rewrite Eq. (10) as

$$P_0 = 1 - \frac{\hat{\lambda}}{\hat{\mu}/4.908} = 1 - \frac{4.908 \cdot (d.c.)\lambda}{(u.t.)\mu} \tag{12}$$

Table 4 shows the initial relationship and improved relationship with low power programming for the ratio $\hat{\lambda}/\hat{\mu}$, utilization u.t., and operation time. Here, the operation time of the microcomputer can be extended to 2.26 hours, compared to 0.46 hours without using low-power-programming techniques.

Table 4 Relationship and improved relationship with low power programming for ratio $\hat{\lambda}/\hat{\mu}$, utilization u.t., and operation time

Initial relationship	$(\frac{\hat{\lambda}}{0.99\ \mu})$	$\frac{(0.3)(0.384w)}{(0.99)(6w)}$	$\frac{(0.3)(0.4w)}{(0.99)(4w)}$	$\frac{(0.3)(0.5w)}{(0.99)(2w)}$	$\frac{(0.3)(0.6w)}{(0.99)(1w)}$
	Utilization (u.t.)	1.92%	3.03%	7.6%	18.2%
	Operation time in 24 hours	0.46hours	0.72hours	1.82hours	4.3hours
Improved relationship	$(\frac{4.908\ \hat{\lambda}}{0.99\ \mu})$	$\frac{(0.3)(4.908)(0.384w)}{(0.99)(6w)}$	$\frac{(0.3)(4.908)(0.4w)}{(0.99)(4w)}$	$\frac{(0.3)(4.908)(0.5w)}{(0.99)(2w)}$	$\frac{(0.3)(4.908)(0.6w)}{(0.99)(1w)}$
	Utilization (u.t.)	9.42%	14.87%	37.3%	89.33%
	Operation time in 24 hours	2.26 hours	3.53 hours	8.93 hours	21.1 hours

6. Conclusions

In the low-power-programming design for a microcomputer system powered by solar cells, we use the 8051 assembly language, C language and a mixed mode of C language and assembly to design the five testing programs. The experimental results show that there is a potential of 4.908 times energy improvement proportion in the mixed mode design with respect to the total effect of the execution time, the HEX codes, the clock cycles and the current consumption. If the average improvement proportion uses low power programming, the operation time can be extended from 0.46 hours to 2.26 hours per day by using our design with solar cells as energy source. In addition, we can also combine our design with other power management methods, and with programming languages such as those cited in the references [8-17] to further reduce the power consumption.

References:

[1] E. P. Harris, S. W. Depp, W. E. Pence, S. Kirkpatrick, M. Sri-Jayantha, and R. R. Trountman, "Technology Directions for Portable Computers," *Proceedings of the IEEE* Vol. 83, No, 4, pp. 636-658, April 1995.

[2] Z. J. Limnios and K. L. Gabriel, "Low-Power Electronics," *IEEE Design & Test of Computer*, Vol. 11, No. 4, pp. 8-13, Winter 1994.

[3] Rulnick, John, M. and Bambos, Nicholas, "Mobile Power Management for Maximum Battery Life in Wireless Communication Network," *Proceedings-IEEE INFOVOM* V2, pp. 443-450, 1996.

[4] P. Berg and D. Lawrence, "System Power Management for PC Card," *IC Card System & Design* Vol.4, pp.31-33, May-Jun 1994.

[5] V. Tiwari, S. Malik, A. Wolfe, "Power Analysis of Embedded Software: A First Step Towards Software Power Minimization," *IEEE Transactions on VLSI*, vol. 2, no. 4, pp. 437-445, Dec. 1994.

[6] V. Tiwari, S. Malik, A. Wolfe, "Instruction Level Power Analysis and Optimization of Software," *Journal of VLSI Signal Processing*, vol. 13, no. 1-2, pp. 223-233, 1996.

[7] H. Mehta, R. Owens, M. Irwin, R. Chen, D. Ghosh, "Techniques for Low Energy Software," *International Symposium on Low Power Electronics and Design*, pp. 72-75, Aug 1997.

[8] C. Gebotys, R. Gebotys, "An Empirical Comparison of Algorithmic, Instruction, and Architectural Power Prediction Model for High-Performance Embedded DSP Processors," *International Symposium on Low Power Electronics and Design*, pp. 121-123, Aug. 1998.

[9] G. Amdahl's, "Validity of the Single-processor Approach to Achieving Large Scale Computing Capabilities," in *Proc. AFIPS Conf.*, pp. 483-485, 1967.

[10] John L. Hennessy and David A. Patterson: 'Computer Architecture a Quantitative Approach' (Morgan Kaufmann Publishers, Inc. 1996 2nd ed.)

[11] J. Nijs, S. Sivoththaman, J. Szluficik, K. De Clercg, F. Duerinckx, E. Van Kerschaever, R. Einhaus, J. Poortmans, Tom Vermeulen, R. Mertruns, "Overview of Solar Cell Technologies And Results on High Efficiency Multicrystalline Silicon Substrates," *Solar Energy Materials and Solar Cell* 48, pp. 199-217, 1997.

[12] A. Rohatgi, S. Narasimha, "Design, Fabrication, and Analysis of Greater Than 18% Efficiency Multicrytalline Silicon Solar Cells," *Solar Energy Materials and Solar Cells* 48, pp. 187-197, 1997.

[13] Willian Sweet, "Technology 1999 Analysis & Forecast: Power & Energy," *IEEE Spectrum*, pp. 62-67, January 1999.

[14] Rajeevan Amirtharajah and Anantha P. Chandraksan, "Self-Powered Signal Processing Using Vibration-Based Power Generation," *IEEE Journal of Solid-State Circuits*, Vol.33, No.5, pp. 687-695, May 1998.

[15] Ying-Wen Bai, "A Queueing Model for Feasibility Analysis of Solar Cells Power Handheld Information System with Dual Rechargeable Batteries," *1999 IASTED, Modeling and Simulation*, pp. 270-275, 1999.

[16] Ying-Wen Bai and Cheng-Lun Chang, "Feasibility Analysis a Queueing Model for a Dual Rechargeable Batteries in Solar Cells Powered Mobile Computers," *Proceedings of IASTED International Conference Applied Modelling and Simulation*, pp. 136-142, May. 2000.

[17] Ying-Wen Bai and Cheng-Lun Chang, "Design and Implementation of Microcomputer 8051 System Powered by Dual Battery Charged by Solar Cells," Fu Jen Studies, Science and Engineering, No. 34, pp. 43-67, Dec. 2000.

太陽能電池供電 8051 微算機系統之低功率程式設計

白 英 文　張 政 崙
輔仁大學電子工程系

摘　要

在有限的太陽能電池供電能力下，爲了延長 8051 微算機系統之再充電週期，這篇論文提出低功率程式設計方法，用以降低微算機系統耗電，並且延長其再充電週期。實驗上，我們依功能需求設計五個測試程式，針對每個測試程式分別以 8051 組合語言、組合語言和 C 程式語言混合、C 程式語言等三個版本建構，進行比較五個測試程式之執行時間、機器碼大小、機器週期個數、電流大小、功率消耗，並換算成能量消耗比較，實驗結果顯示，我們可以獲得再充電週期可調性性能，其電能節省可調範圍相依於組合語言使用比例，而五個測試程式平均最高可達九倍之電能節省。對於其它微算機系統，使用組合語言的效能改善也提供了類似的潛力，延長了太陽能電池供電之再充電週期。

關鍵詞：微算機系統，低功率程式設計，太陽能電池

I. Introduction

Relaxor ferroelectrics generally mean the complex perovskites with ABO_3-type unit cell and are crystals in which unlike-valence cations belonging to a given site (A or B) are presented in the correct ratio for charge balance, but are situated randomly on these cation sites.[1-4] These randomly different cation charges give rise to random fields, which tend to make the phase transition "diffuse" instead of sharp as in normal ferroelectrics.[3,4] Lead magnesium niobate, $Pb(Mg_{1/3}Nb_{2/3})O_3$ (PMN), is one of the most interesting relaxor ferroelectric (FE) materials. PMN has a disordered complex structure in which the Mg^{2+} and Nb^{5+} cations exhibit only short-range order on the B-site. Near 280 K the PMN crystal undergoes a diffuse phase transition characterized by a broad frequency-dependent dielectric maximum. PMN has cubic symmetry at room temperature with space group *Pm3m,* whereas a small rhombohedral distortion (pseudocubic) was observed below 200 K.[1,5] Transmission electron microscopy (TEM) investigation has revealed the presence of nanometric scale polar clusters in the relaxor state.[6] The normal FE crystal $PbTiO_3$ (PT) has tetragonal symmetry with space group *P4mm* at room temperature and has a normal FE phase transition taking place at T_c=760 K with long-range FE order occurring below T_c.[7]

The relaxor-based FE crystals $(PbMg_{1/3}Nb_{2/3}O_3)_{1-x}(PbTiO_3)_x$ (PMN-*x*PT) naturally has a morphotropic phase boundary (MPB) in the range of ~28 to ~36 mol% of PT.[8] In other words, as temperature decreases, the PMN-*x*PT crystals ($0.28 \le x \le 0.36$) have successive phase transformations: cubic paraelectric (PE) phase → tetragonal FE phase → rhombohedral FE phase. However, these phase transformations do not exhibit normal FE phase transitions in which clear transition temperatures are defined. In relaxor-based ferroelectrics, the symmetry of the low temperature is broken by quenched disorder. Rather than undergoing a normal phase transformation into the low-temperature state, the system freezes into a state with polar clusters of the low-temperature state embedded within the average symmetry

Orientation dependences and E-field effect in relaxor-based ferroelectric crystal $(PbMg_{1/3}Nb_{2/3}O_3)_{0.68}(PbTiO_3)_{0.32}$ (PMN-32%PT)

Chi-Shun Tu, C.-L. Tsai and Li-Wei Hung

Department of Physics,
Fu Jen University,
Taipei, Taiwan 242, Republic of China

Abstract

Dielectric permittivities and polarization-electric-field hysteresis loops have been measured as a function of temperature in relaxor-based ferroelectric single crystals $(PbMg_{1/3}Nb_{2/3}O_3)_{0.68}(PbTiO_3)_{0.32}$ (PMN-32%PT) for $<110>_{cub}$ and $<211>_{cub}$ orientations. Contrary to the pure $PbMg_{1/3}Nb_{2/3}O_3$ (PMN), PMN-32%PT exhibits apparent crystallographic orientation dependences of dielectric permittivities, polarizations, and phase transitions. With a prior field-cooled treatment, a field-induced state, perhaps of orthorhombic symmetry, is evidenced and coexists with the rhombohedral symmetry in the low-temperature region. This field-induced phase is manifested by an extra dielectric peak observed near 373 K for the $<211>_{cub}$ orientation.

Key Words: dielectric permittivity; phase transition; phase coexistence.

of the high-temperature state. TEM results of MPB compositions of PMN-PT ceramics showed tweed-like structures rather than normal micron-sized domains.[9] These tweed-like structures were oriented along the <110> direction. Domains of ~10^3 Å in length and ~10^2 Å in width were reported.[9]

In relaxor ferroelectrics the sensitive lattice symmetry is easily affected by external perturbations. Contrary to normal ferroelectrics, an external electric field can enhance phase transition.[10,11] Paik *et al.* showed that a field of 20 kV/cm in the <001>-oriented $(PbZn_{1/3}Nb_{2/3}O_3)_{0.92}$-$(PbTiO_3)_{0.08}$ (PZN-8%PT) destroys the rhombohedral state and induces a single tetragonal domain.[10] By *in situ* X-ray diffraction, Durbin *et al.* confirmed that the field-induced crystallographic change occurs at E~10 kV/cm from rhombohedral to tetragonal states.[11] It was proposed that under field (E<10 kV/cm) the sample can no longer be perfectly rhombohedral, but that instead it is almost certainly monoclinic.[11] From the E-field-dependent polarization result, a metastable intermediate orthorhombic FE phase (between rhombohedral and tetragonal states) was proposed to exist in the oriented PZN-8%PT crystal.[12] The unit cell of this intermediate orthorhombic phase is double that of the simple unit cell. This simple unit cell has monoclinic symmetry having the same point group as that recently suggested by Cross for PZN-PT crystals.[13] In brief, with increasing E-field strength, PZN-8%PT undergoes successive phase transitions: rhombohedral → orthorhombic → tetragonal. Furthermore, a phenomenological model for MPB compositions of PZT demonstrated that an orthorhombic FE phase is possible as a metastable state between the tetragonal and rhombohedral states.[14] Such an intermediate orthorhombic phase could be enhanced and stabilized under an external E-field. By optical microscopy, with field applied along <001>, Belegundu *et al.* confirmed that tetragonal and rhombohedral domains coexist in PZN-8%PT at room temperature and even down to −100 °C.[15] It has been found that relaxor-based ferroelectrics exhibit large disparity in spatial micro-heterogeneity and transition temperature.[16,17] Such a fluctuation is believed to result from a quenched unequal occupation of the B

site by the competitive ions Mg^{2+}, Nb^{5+} and Ti^{4+}.

Single crystals of PMN-*x*PT have been reported to exhibit much larger piezoelectric constants and electromechanical coupling factors compared with those in the $PbZrO_3$-$PbTiO_3$ (PZT) family of ceramics.[18-20] Such high piezoelectric performance, which converts mechanical and electric energies, is crucial in medical imaging, telecommunication and ultrasonic devices and may revolutionize these applications.[21] Many works have been undertaken on the growth and characterization of relaxor-based ferroelectrics.[22-28] However, limited attention has been paid to phase coexistence at the MPB.[24,28] The physical mechanism and temperature ranges of the MPB between two different phases (cubic ↔tetragonal & tetragonal ↔ rhombohedral) still remain unclear. It is believed that the field-induced transformation, phase coexistence and crystallographical orientation play important roles in the high electromechanical coupling effect. Therefore, we carried out temperature-dependent measurements of dielectric permittivity and polarization-electric-field (P-E) hysteresis loop on PMN-32%PT for $<110>_{cub}$ and $<211>_{cub}$ oriented crystals.

II. Experimental Procedure

The lead magnesium niobate-lead titanate single crystal PMN-32%PT was grown using a modified Bridgman method.[22] Samples were cut perpendicular to either the $<110>_{cub}$ or $<211>_{cub}$ directions. Here, direction "$< >_{cub}$" refers to the pseudocubic axes. Physical analysis by the JEOL6100 electron microscope was used to determine concentrations of local B-site ions Mg^{2+}, Nb^{5+} and Ti^{4+}. In the PMN-32%PT platelets that we measured, the Ti^{4+} concentration of each sample varies by about ±2% from its nominal or average composition. The average Ti^{4+} concentration of the $<211>_{cub}$ oriented sample is slight larger (about 0.3%) than the value of the $<110>_{cub}$ oriented sample. Since the MPB is sensitive to the Ti^{4+} content, a slight spatial heterogeneity will result in difference of structural transformation temperatures at the MPB.[8] For measurements of dielectric permittivity and P-E hysteresis loop,

sample surfaces were coated with silver paste electrodes. The applied electric fields were along either the $<110>_{cub}$ or $<211>_{cub}$ directions. The average thickness of samples for P-E hysteresis loop experiment is about 0.15 mm. A variable-frequency Wayne-Kerr Precision Analyzer PMA3260A with four-lead connections was used to obtain capacitance and resistance. The heating/cooling rate for dielectric measurement was 1.5 K/min. For the field-cooled-zero-field-heated (FC-ZFH) dielectric measurement, the PMN-32%PT samples were first cooled from 470 K (cubic state) to the rhombohedral phase (≤ 200 K) with a dc bias field of E=6 kV/cm along either the $<110>_{cub}$ or $<211>_{cub}$ directions. Then the dielectric permittivity was measured upon heating without a bias field (ZFH) The P-E hysteresis loop was measured by using a Sawyer-Tower circuit in which the P-E loop was obtained within 2-4 cycles of electric field at measuring frequency 47 Hz. A Janis CCS-450 closed cycle refrigerator was used with a Lakeshore 340 temperature controller.

III. Results and Discussion

Figures 1(a) and 1(b) show the temperature dependences of the real part ε' of the dielectric permittivity obtained from ZFH and FC-ZFH for $<110>_{cub}$ and $<211>_{cub}$ oriented PMN-32%PT crystals, respectively. Due to slight difference in PT content (spatial heterogeneity), $<110>_{cub}$ and $<211>_{cub}$ orientations show about 4 K difference in the temperature T_m which corresponds to the maximum of ε'(ZFH). Compared with the ZFH, T_m of the FC-ZFH run was shifted up respectively ~3 K and ~4 K for $<110>_{cub}$ and $<211>_{cub}$ orientations. ε'(ZFH) exhibits a broad plunge accompanied by a frequency dispersion near 360 K and 380 K respectively for $<110>_{cub}$ and $<211>_{cub}$ orientations. These behaviors correspond to the so-called diffuse phase transitions due to structural fluctuations between various local states. In particular, ε'(FC-ZFH) of $<110>_{cub}$ and $<211>_{cub}$ orientations exhibit a sharp step-like jump near 360 K and an extra peak at 373 K (which superimposes on the broad background of dielectric permittivity), respectively.

The temperatures of these anomalies (but not their amplitudes) are independent of frequency. In addition, near 420 K the broad permittivity peak ε_m'(FC-ZFH) of the $<110>_{cub}$ orientation has magnitude ~7,000, about 17% lower than the value of ε_m'(ZFH)~8,400, due to the FC process that reduces domain wall contributions to the dielectric permittivity. For the $<211>_{cub}$ orientation, the permittivity peak ε_m'(FC-ZFH) near 418 K has magnitude ~7,000, about 42% lower than the value of ε_m'(ZFH)~12,000.

Fig. 2 shows two clear thermal hystereses of ε' in the regions of ~280-360 K and ~400-415 K. The insets are the reciprocal of ε' in which a typical first-order-like FE phase transition appears near 415 K. We call these first-order transitions (near 360 and 415 K) for two reasons. First, the thermal hysteresis shows that the system is metastable in this temperature region. Metastability can occur for first- but not second-order transitions.[29] Second, the point groups of the tetragonal and rhombohedral symmetries do not have a group-subgroup relation, so a transition between these two symmetries must be of first order.

P-E hysteresis loops are shown in Figs. 3(a) and 3(b). Spontaneous polarizations (P_s), measured at room temperature, are about 38.7 $\mu C/cm^2$ and 45.4 $\mu C/cm^2$ for $<110>_{cub}$ and $<211>_{cub}$ orientations, respectively. At room temperature, both $<110>_{cub}$ and $<211>_{cub}$ orientations have similar amplitude of coercive field ~5 kV/cm. Coercive fields for different PT contents, measured at room temperature, vary from 3.4 kV/cm (for PMN-24%PT) to 8.0 kV/cm (for PMN-34%PT).[17] However, the coercive field (E_c) of pure $PbTiO_3$ is ~6.8 kV/cm.[30] We cannot explain this E_c dependence, because coercive field is strongly dependent on the rise rate (measuring frequency) of applied field and sample thickness. The thickness dependence of E_c was originally found in $BaTiO_3$ and is attributed to the existence of a space-charge layer.[31]

We now discuss the orientation dependence of P_s. According to the MPB location,[8] near room temperature PMN-32%PT consists of rhombohedral clusters. The fraction of spontaneous polarization along <110> for <111> oriented rhombohedral states must be $\sqrt{2/3}$ [*i.e.* $\cos\theta = (111)\cdot(110)/\sqrt{6}$].

Similarly, the fraction of spontaneous polarization along <211> for <111> oriented rhombohedral states must be $4/3\sqrt{2}$. In other words, the ratio of spontaneous polarization components along <110> and <211> oriented rhombohedral states is $\sqrt{3}/2 \approx 0.87$, which is quite consistent with the ratio of measured spontaneous polarizations (obtained at room temperature), *i.e.* (38.7)/(45.4)≈0.85 (see Fig. 3). Such a crystalline anisotropy of dielectric properties indicates that PMN-32%PT crystal has stronger crystalline distortion than the pure PMN whose average symmetry is cubic near room temperature.[1,5] Temperature-dependent behaviors of remanent polarization (P_r) and E_c are plotted in Fig. 4. Instead of a gradual evolution as seen in PMN,[32] two successive step-like anomalies were observed in both P_r and E_c curves near 360 K and 415 K for the $<211>_{cub}$ orientation. For the $<110>_{cub}$ orientation, the E_c curve also shows two anomalies near 360 K and 415 K. The usual distinctions between first- and second-order transitions, such as discontinuity in dP/dT, do not apply for diffuse phase transitions.

Probably the most convincing evidence for the field-induced, possibly orthorhombic, phase is the extra peak in the zero-field-heated dielectric permittivity ε'(FC-ZFH) shown at 373 K after field cooling in a dc bias field [see Fig. 1(b)]. The ε'(FC-ZFH) exhibits successively a gradual plunge and an extra peak at 360 K and 373 K. These continuous temperature-dependent anomalies possibly imply sequential phase transformatios: rhombohedral→orthorhombic→tetragonal. Similar phase transformations were seen in the $BaTiO_3$ system in which a stable orthorhombic FE phase was observed between the FE rhombohedral and FE tetragonal phases.[33] During the FC process, the external E-field bias along the <211> direction could cause polar displacement to deviate from the <111> direction in the unit cell of the rhombohedral phase, resulting in the lack of threefold symmetry with only mirror symmetry on the {011} plane. An orthorhombic (O) phase occurring near the rhombohedral-tetragonal (R-T) morphotropic phase boundary in this crystal could occur for two reasons. First, this phase could be thermodynamically stable even in the absence of stress energy

considerations. Second, the phase may only be metastable in the absence of stress energy considerations. That is, at the morphotropic phase boundary, the R and T phases would have the same free energy, but the O phase would have higher free energy.

IV. Conclusions

In this report, two important features have been found from $<110>_{cub}$ and $<211>_{cub}$ oriented PMN-32%PT crystals. First, PMN-32%PT exhibits apparent crystallographical orientation dependences of dielectric permittivities, polarizations, and phase transitions. Second, with a prior field-cooled process from the cubic state, a field-induced state, perhaps of orthorhombic symmetry, is observed and coexists with the rhombohedral symmetry in the low temperature region. This partial field-induced effect also enhances a sharp step-like jump and an extra peak in dielectric permittivity appeared near 360 K and 373 K for $<110>_{cub}$ and $<211>_{cub}$ orientations, respectively. It was evidenced that an external E-field can suppress this relaxation behavior and enhances long-range percolating polar clusters.

Acknowledgments

This work was supported by Grant No. NSC90-2112-M-030-001 and the grant from the SVD section.

References:

1. L.E. Cross, *Ferroelectrics* **76**, 241 (1987).
2. D. Viehland, M. Wuttig, and L.E. Cross, *Ferroelectrics* **120**, 71 (1991).
3. V. Westphal and W. Kleemann, and M.D. Glinchuk, *Phys. Rev. Lett.* **68**, 847 (1992).

4. Z.-G. Ye, *Key Eng. Mater.* **155-156**, 81 (1998).
5. L.A. Shebanov. P. Kaspostins, and J. Zvirgzds, *Ferroelectrics* **56**, 1057 (1984).
6. C. Randall, D. Barber, and R. Whatmore, *J. Microsc.* **45**, 275 (1987).
7. M.L. Mulvihill, S.E. Park, G. Risch, Z. Li, and K. Uchino, *Jpn. J. Appl. Phys.* **35** (part 1), 3984 (1996).
8. T.R. Shrout, Z.P. Chang, N. Kim, and S. Markgraf, *Ferroelectrics Letters* **12**, 63 (1990).
9. D. Viehland, M. Kim, Z. Xu, and J. Li, *Appl. Phys. Lett.* **67**, 2471 (1995).
10. D.S. Paik, S.E. Park, S. Wada, S.F. Liu, and T.R. Shrout, *J. Appl. Phys.* **85**, 1080 (1999).
11. M.K. Durbin, E.W. Jacobs, J.C. Hicks, and S.-E. Park, *Appl. Phys. Letter* **74**, 2848 (1999).
12. D. Viehland, *J. Appl. Phys.* **88**, 4794 (2000).
13. L.E. Cross, *Workshop on Piezoelectric Crystals*, Arlington, VA, 2000.
14. A. Amin, M.J. Haun, B. Badger, H. McKinstry, and L.E. Cross, *Ferroelectrics* **65**, 107 (1985).
15. U. Belegundu, X.H. Du, and K. Uchino, *Ferroelectrics* **222**, 67 (1999).
16. F.M. Jiang and S. Kojima, *Appl. Phys. Lett.* **77**, 1271 (2000).
17. C.-S. Tu, C.-L. Tsai, V. H. Schmidt, H. Luo, and Z. Yin, *J. Appl. Phys.* **89**, 7908 (2001).
18. S.-E. Park and T.R. Shrout, *J. Appl. Phys.* **82**, 1804 (1997).
19. Y. Yamashita, *Jpn J. Appl. Phys.* **33** (part 1), 5328 (1994).
20. S.W. Choi, T.R. Shrout, S.J. Jang, and A.S. Bhalla, *Ferroelectrics* **100**, 29 (1989).
21. R.F. Service, *Science* **275**, 1878 (1997).
22. H. Luo, G. Xu, P. Wang, and Z. Yin, *Ferroelectrics* **231**, 97 (1999).
23. H. Fu and R.E. Cohen, *Nature* **403**, 281 (2000).
24. C.-S. Tu, F.-C. Chao, C.-H. Yeh, C.-L. Tsai, and V.H. Schmidt, *Phys. Rev. B* **60**, 6348 (1999).

25. S. Gentil, G. Robert, N. Setter, P. Tissot, and J.-P. Rivera, *Jpn. J. Appl. Phys.* **39**, 2732 (2000).
26. M.K. Durbin, J.C. Hicks, S.-E. Park, and T.R. Shrout, *J. Appl. Phys.* **87**, 8159 (2000).
27. S. Saitoh, T. Kobayashi, K. Harada, S. Shimanuki, and Y. Yamashita, *Jpn. J. Appl. Phys.* **37**, 3053 (1998).
28. Z.-G. Ye and M. Dong, *J. Appl. Phys.* **87**, 2312 (2000).
29. M.E. Lines and A.M. Glass, *Principles and Applications of Ferroelectrics and Related Materials,* (Oxford, London, 1977).
30. J.P. Remeika and A.M. Glass, *Mater. Res. Bull.* **5**, 37 (1970).
31. F. Jona and G. Shirane, *Ferroelectric Crystals*, (Dover, New York, 1993).
32. V.A. Bokov and I.E. Mylnikov, *Soviet Physics-Solid State* **3**, 613 (1961).
33. J. Merz, *Phys. Rev.* **76**, 1221 (1949).

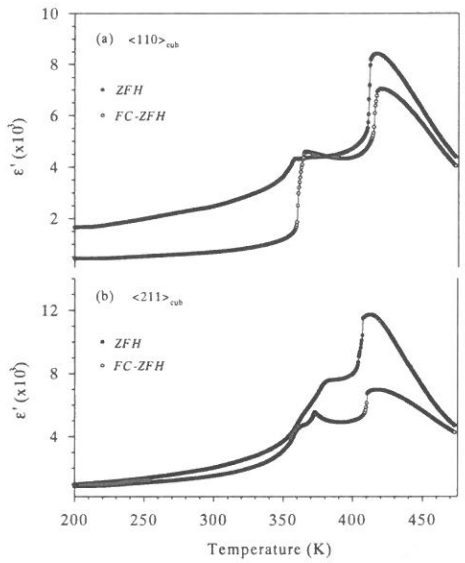

Fig. 1 Temperature dependences of ε'(ZFH) and ε'(FC-ZFH) for (a) $<110>_{cub}$ and (b) $<211>_{cub}$ orientations. The dielectric data are taken at f=10 kHz upon heating.

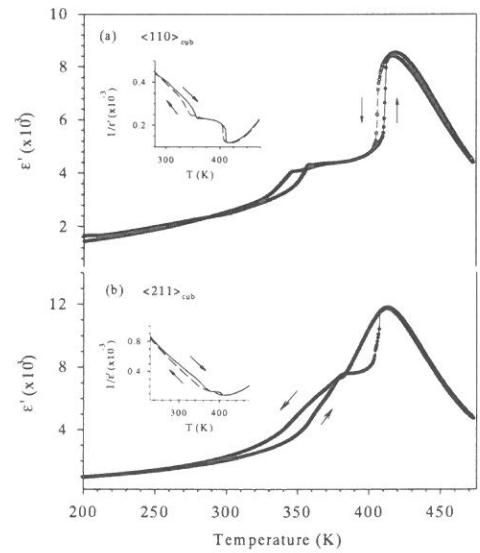

Fig. 2 Thermal hysteresis behaviors of ε'(ZFH) for (a) $<110>_{cub}$ and (b) $<211>_{cub}$ orientations taken at f=10 kHz. The insets are the reciprocal of ε'(ZFH).

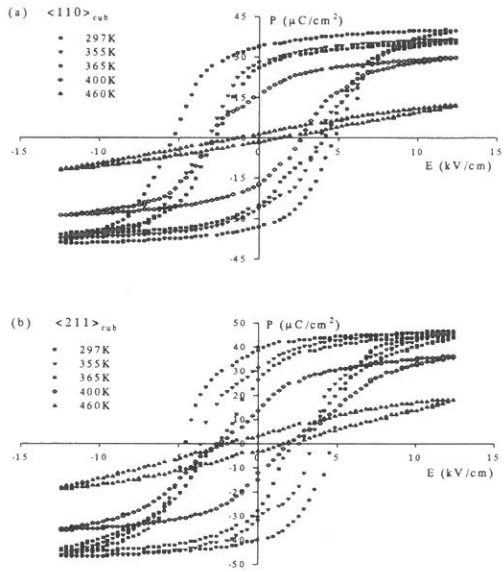

Fig. 3 P-E hysteresis loops of (a) $<110>_{cub}$ and (b) $<211>_{cub}$ orientations obtained upon heating.

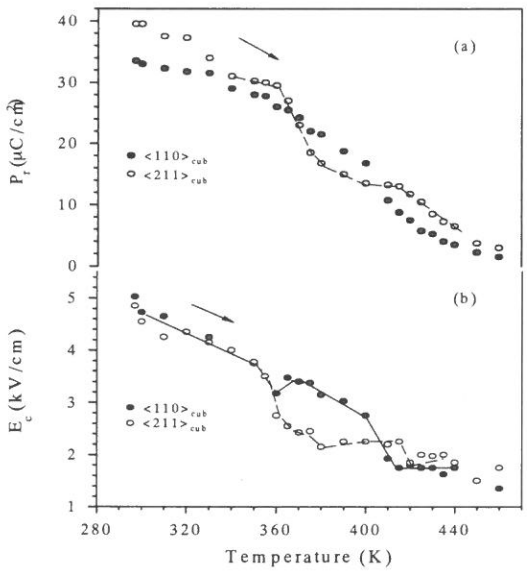

Fig. 4 Temperature dependences of (a) remanent polarization (P_r) and (b) coercive field (E_c) for $<110>_{cub}$ and $<211>_{cub}$ orientations upon heating. The dashed and dotted lines are guide for the eye.

晶格軸向與電場的效應在高應變鐵電晶體 $(PbMg_{1/3}Nb_{2/3}O_3)_{0.68}(PbTiO_3)_{0.32}$

杜 繼 舜　蔡 志 龍　洪 立 維

輔仁大學物理系

摘　要

從變溫，變頻及外加電場的介電常數與電滯曲線，$(PbMg_{1/3}Nb_{2/3}O_3)_{0.68}(PbTiO_3)_{0.32}$ 晶體顯示明顯的晶格軸向與電場效應。而且呈現複雜的連續結構相變：rhombohedral 對稱的鐵電相(低溫相) ↔ 相共存區(I) ↔ tetragonal 對稱的鐵電相 ↔ 相共存區(II) ↔ cubic 對稱的順電相(高溫相)。相共存區(I)含有兩種結構：rhombohedral 及 tetragonal，且共存的溫度範圍很廣。相共存區(II)則是包含 tetragonal 及 cubic 兩種結構，共存的溫度範圍相對狹窄許多。由於不同結構的競爭擾動，在 "相共存區(I)" 裡的結構，不具有長程有序(long-range order)，這種不穩定及低對稱混合結構，使得晶體在外加場作用下，較易產生晶格形變 (可能是 orthorhombic 對稱)。在相變點附近，介電常數顯示明顯的連續 "熱滯曲線" 現象，證實晶體內存在所謂的 "中間穩定態(metastable state)"，連續相變都是屬於一階型(first-order)相變。

關鍵詞：介電常數、相變、共存相

Mobile Agent Technology in Business Processes Management

Jong-Yih Kuo

Department of Computer Science and Information Engineering
Fu Jen Catholic University
Taipei, Taiwan 242, R.O.C.

Abstract

Due to the development of Internet and the desire of almost all departments of business organizations to be interconnected and to make data accessible at any time and any place, more and more workflow management systems are applied to business process management. In this paper, a mobile, intelligent and document-driven agent system framework is proposed to modeling business process management system based on MADEPT (Mobile-ADEPT). By mobility technology, our approach improves the communication, agent life cycle and environment sensibility of ADEPT (Advanced Decision Environment for Process Tasks). The modified communication mechanism in the external architecture of agent reduces the network loading and makes the communication between agents more flexible. The agent life cycle and the environment sensibility affect the internal architecture of agent. Each mobile agent encapsulates a single document to achieve trace ability, document life cycle management, and dynamic scheduling. We also implemented an official document system explaining our approach by Aglet.

1. Introduction

Workflow management promises a new solution to a traditional problem: controlling, monitoring, optimizing and supporting business processes. Traditional business process management (BPM) system utilizes distributed objects management (DOM) technology [15] to manage and negotiate the heterogeneous and distributed business activity of enterprises. DOM supports the interoperation, location transparency, encapsulation and integration for business system [6]. Currently, existing enterprises are expanding from simple organization to international distributed companies where business processes dynamically form temporary alliances, joining their business in order to share their costs, skills and resources in supporting certain activities [1, 7]. Many researches proposed agent technology to automate process operation integrating the different business systems to reduce the complexity [8, 11, 16]. Several benefits are obtained for applying agent technology in the BPM [10], including autonomy, social ability, pro-activeness, and responsiveness. Agents perform the majority of their problem solving tasks without the direct intervention of humans or other agents, and they have control over their own actions and their own internal state. Agents interact, when they deem appropriate, with other artificial agents and humans in order to complete their problem solving and to help others with their activities. Agents take the initiative where appropriate and perceive their environment and respond in a timely fashion to changes that occur in it.

The software agent has been widely adopted in the application area. However, most researchers do not propose a mobile property developing an agent system for business process management. In addition, for the variant communication environment, an artificial intelligence technology for an agent system is in need. Moreover, mobile agent technology offers several advantages over traditional approaches to Internet applications [4]. It can proceed without continuous network connections to save significant bandwidth by moving locally to the resources they need, because interacting entities can be moved to the same site when connections are available, and

can then interact without requiring further network connections. The mobile agent can carry the code to manage remote resources and do not need the remote availability of a specific server, so it has intelligent information gathering to work with mobile computing systems, Thus, several BPM systems are designed by mobile agent technology [5, 17, 18, 19, 20].

As complex business processes rely on intensive information exchange with the company's environment, they are document-driven by nature [2]: employees deal with and react to information and knowledge transferred by and embedded in all kinds of documents, including forms, letters, books, manuals, records, either electronic or paper-based. Documents reflect many results of business processes in the private as well as in the public sector [21]. Most of business processes are centered about the "disposal record", a document that allows a company to dispose of a certain type product or process in the approved way. Consequently, one would like the BPM system to automatically offer access to relevant knowledge source, or to even directly "pump" information items extracted from incoming documents to the appropriate places in the data models of the actual workflow instance.

In order to develop the agent-based system, we first analyze a number of business processes from various industrial and commercial domains. The purposes of this analysis are to abstract the common characteristic. Then we build the external architecture of agent-based BPM system. Second, we extract the documents and its related business logic (that is defined by TBCG-based XML [23, 24]) from the business process. Then we establish the internal architecture of agent-based BPM system. Finally, we implement the framework to different business systems of domains (see Figure 1).

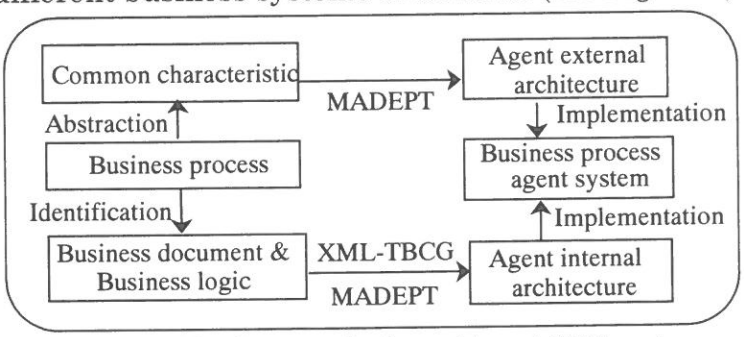

Figure 1: The framework of agent-based BPM system

In this paper, we present the procedures that we use to improve ADEPT approach by mobile agent technology and document-driven concept [2, 21] into MADEPT which owns the advantages of ADEPT and mobility. Because of our improvement of ADEPT approach, the business documents can be packaged and handled by mobile agent over distributed business systems. We will also present a case study explaining our approach. We use Aglet to implement the BMP system of our case study. In the sequel, we first review the ADEPT approach. The MADPET are fully discussed in Section 3. The case study is outlined in Section 4. Finally we conclude the paper by outlining the potential benefits of the proposed approach in Section 5.

2. Adept

ADEPT [9, 10, 12] adapts multi-agent architecture composed of a number of autonomous agencies (see Figure 2). An agency contains a single responsible agent, a possibly empty set of subsidiary agencies and a set of tasks that are under the direct management of the responsible agent. The recursive definition of an agency allows a nested (hierarchical) agent system to be constructed in which a responsible agent realizes its function through the responsible agents of lower level agencies. The responsible agent is autonomous. Agents have control over the tasks that they may perform, the resources available to them and how they coordinate their activities with other agents. A responsible agent's agency represents its domain problem solving resources. Agents operate by negotiation for services, or units of problem-solving activity, in the management of a business process (a task is an atomic service).

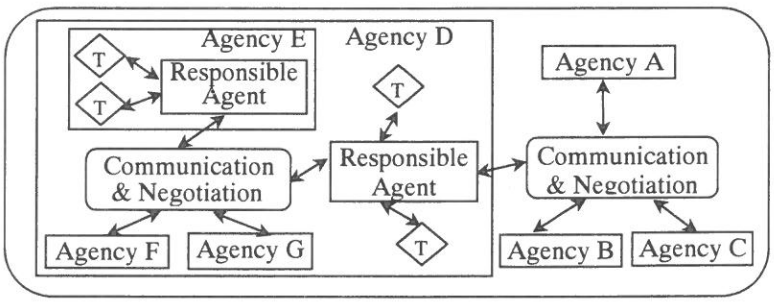

Figure 2 : The external architecture of ADEPT

ADEPT is based on agent-based technology to provide a well structure for dealing with BPM. The architecture can model the organizations of enterprises, such as structure of hierarchical or flat organizations, or a mixture of the two, through the concepts of agents and agencies. It also provides a design and implement pattern for multi-agent BPM systems.

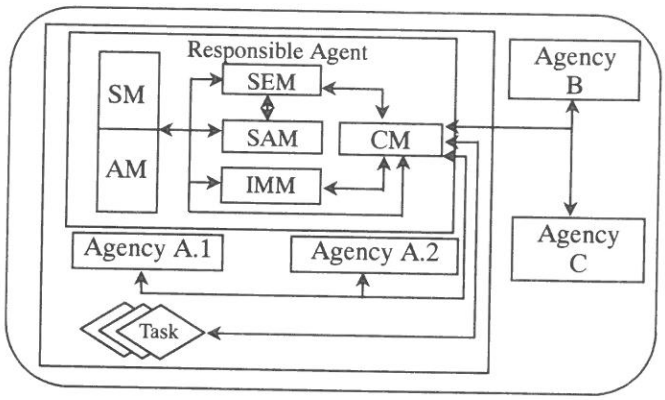

Figure 3 : The internal architecture of ADAPT

All ADEPT agents have the same basic internal architecture, illustrated by the responsible agent of agency A (Figure 3). An agent has six functional components: communication Module (CM), Interaction Management Module (IMM), Situation Assessment Module (SAM), Service Execution Module (SEM), Acquaintance Model (AM), and Self Model (SM).

The CM routs messages between an agent and both its agency and peers. The IMM provisions services through negotiation. The SAM invokes the IMM to initiate negotiation for a service. The SAM is responsible for assessing and monitoring the agent's ability to meet the service level agreements (SLA) it has already agreed and any SLA that it may agree in the future. The SEM is responsible for managing services throughout their execution. This involves service execution management, information management, and exception handling. The Within the AM, the agent maintains a record of peers and subsidiaries which can provide services of interest. The SM is the primary storage site for SLA to which the agent is committed, descriptions of the

services the agent can provide, run time application / service specific information, and generic domain information. The internal architecture of ADEPT is designed to ensure maximum flexibility to adapt as a business process changes.

3. Mobile - ADEPT

Although ADEPT has been attracting widespread interest in BPM, several developmental obstacles remain. The major weakness of this approach is the lack of monitoring, trace ability, and mobility for business activity. We proposed the MADEPT, a document-driven approach that applied the ADEPT and mobility technology to encapsulate a document as a mobile agent that handles the business activity. The mobile agent can trace and monitor the business document, so that the business process may be better managed.

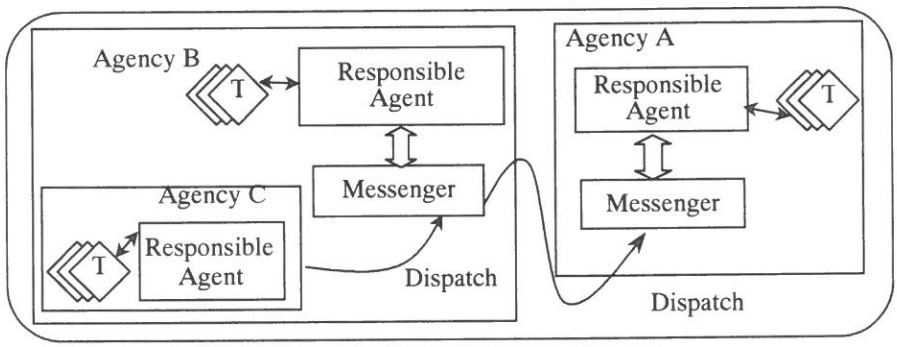

Figure 4 : The external architecture of MADEPT

In the ADEPT environment, agents are stationary. The concepts between mobile agent and stationary agent differ in terms of: (1) the communication message, (2) the life cycle of agent, and (3) the cognition of context. The communication message will affect the external architecture of agent, and the other two may alter the internal architecture of agents.

3.1 The external architecture

In order to communicate with remote agents, we created a messenger agent that moves itself to the remote content. We modify the external architecture of agents shown as Figure 4. In Figure 4, agency A and B are

peers, and agency C is the subsidiary of agency B. The responsible agent of agency C generates a messenger agent that moves locally to agency B in order to interact with each other. In a traditional ADEPT environment, agency C cannot communicate with agency A directly. However, the architecture proposed in this paper is capable of communicating with agency A.

In the architecture proposed, two agent types are provided. The responsible agent is a stationary agent that creates and dispatch the messenger agent into the right server for some missions. The user can control it through the user interface. The messenger agent is a mobile agent with no user interface. A user cannot directly communicate with the messenger agent. The responsible agent is the only one that a user can directly communicate with. A messenger agent can pack a document up and run the business process described in the document. The comparison between the two types of the agents is summarized in table 1.

Table 1: Responsible agent v.s. messenger agent

	Responsible agent	Messenger agent
GUI	Yes	No
CM	User, messenger	Responsible, messenger agent
SEM	Maintain services	Maintain tasks
SAM	Schedule services	Schedule itinerary
Functional Module	No mobility	Mobility
Knowledge-base handler	AM&SM	Locker pattern

3.2 The internal architecture

As Figure 5 shown, the internal architecture of an agent retains some common modules of ADEPT, including CM, IMM, SEM, and SAM. We further proposed the functional module and knowledge-base handler to enable the mobility.

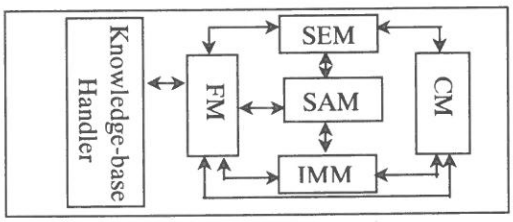

Figure 5 : The internal architecture of MADEPT

The functional module is designed for the mobility and recognition ability of mobile agent, including the mechanisms of dispatch, retract, dispose, clone, activate, deactivate, and create. It also provides some specific domain functionalities. The knowledge-base handler is a knowledge storage for the reasoning mechanism where the agent is committed, describing the services the agent can provided, running time application/service specific information and generic domain information.

3.3 Discussion

By using mobile agent technology to improve ADEPT, there are three advantages of MADEPT, including better communication, higher trace ability, and greater environmental sensitivity

In ADEPT, only the peer agency can communicate with each other. In MADEPT, the messenger agent can move to any level of the agency to communicate with on another. By doing that, the network loading is reduced and the communication between agencies is more efficient and flexible. An administrator can easily monitor the business processes through the messenger agent in MADEPT. We design the functional module of the agent to capture the mobility. We also developed the knowledge-base handler to store the knowledge about the environment. Our design enables an agent of MADEPT to perceive its environment and respond in a timely fashion to the change occurred. Thus, the agent is able to schedule its itinerary and services dynamically.

4. Case Study

In this section, we are going to use Aglet implementing a document-driven agent system and an official document agent system by applying MADEPT architecture. First, we use the activity diagram to represent the scenario of official document system. Second, once the system architecture is established, the internal and external architectures of agent are designed to

fit the system. Finally, the official document agent system is implemented by Aglet [22, 23, 24]. The development process of document-driven agent system is shown on Figure 6.

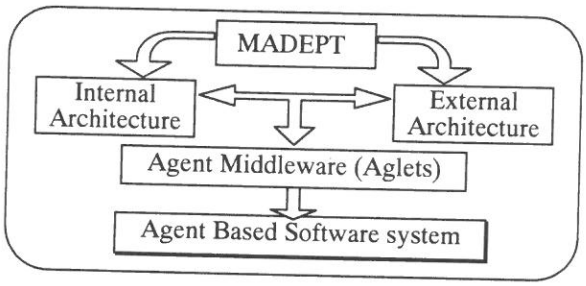

Figure 6 : Development process in document-driven agent system

The scenario of an official document is shown as follow:

1. An office clerk of a department at the college writes a missive and sends it to the chairman of his department.
2. The chairman of department gives some comments and then sends the missive to the chairman of the college.
3. The chairman of the college gives some more comments and then sends the missive to the office of Academic Affairs, Student Affairs, General Affairs, Accounting, and Personnel.
4. The directors of these offices give their comments, and then send the missive to the secretariat.
5. As soon as the head of secretariat receives the missive, she/he sends it to the president of school. Finally, the missive is sent back to the department clerk.

We are going to use the activity diagram representing the scenario described above as Figure 7.

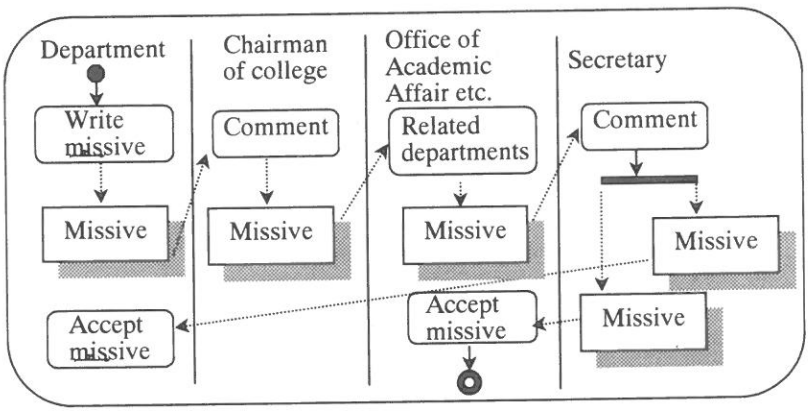

Figure 7 : The activity diagram of official document

4.1 The architecture of the system

Aglet [13, 14] is designed for development the mobile Java agent system that supports the concepts of autonomous execution and dynamic routing on its itinerary. The Agent server provides an environment for aglets to execute in, and the Java virtual machine and the Aglet security manager make it safe to receive and host aglets. Aglets framework use ATP (Agent Transfer Protocol) as a network protocol for dispatching aglets [20]. The other way to move an aglet is to retract it from a remote context. The ATP daemon is responsible for receiving messages and giving safe authorization (Figure 8).

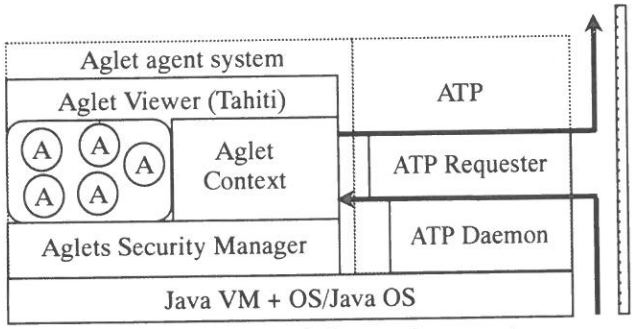

Figure 8 : Aglet environment

In the aglet object model, a mobile agent is a mobile object that has its own thread of control, is event-driven, and communicates by message passing. This model defines a set of abstractions and the behavior needs to leverage

mobile agent technology in Internet-like, open wide-area networks. The key abstractions are aglet, proxy, context, and identifier. An agent is mobile Java object that visit agent-enabled hosts in a computer network. It is autonomous and reactive. A proxy is a representative of an aglet. It serves as a shield that protects the aglet from direct access to its public methods. The proxy also provides location transparency for the aglet; that is, an aglet and its proxies can be separated so that a local proxy hides the remoteness of the aglet. A context is an aglet's workplace. It is a stationary object that provides a means for maintaining and managing running aglets in a uniform execution environment where the host system is secured against malicious aglets. An identifier is bound to each aglet.

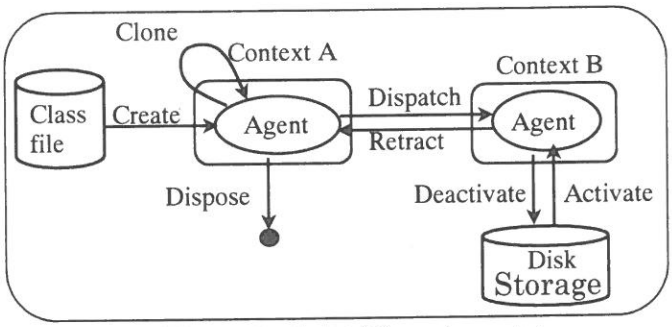

Figure 9 : Aglet life-cycle model

There are two ways to bring an aglet to life: either it is instantiated from scratch (creation) or it is copied from an existing aglet (cloning). To control the population of aglets you can destroy them (disposal). Aglets are mobile in two different ways: (1) actively : An aglet pushes itself from its current host to a remote host (dispatch); (2) passively : A remote host pulls an aglet away from its current host (retract)。When aglets are running, they take up resources. To reduce their resource consumption, aglets can go to sleep temporarily, releasing their resources (deactivation) and later can be brought back into running mode (activation). Finally, multiple aglets can exchange information to accomplish a given task (messaging). The aglet life cycle is shown as Figure 9.

4.2 The external and internal architecture of agent system

The official document agent system is a web-based system, so users can use the web browser to interact with each other*. Each department has an Aglet agent environment that is viewed as an agency of the agent system. Each agency encompasses the document control agent, the document agent, the message agent, and the knowledge-base handler (see Figure 10).

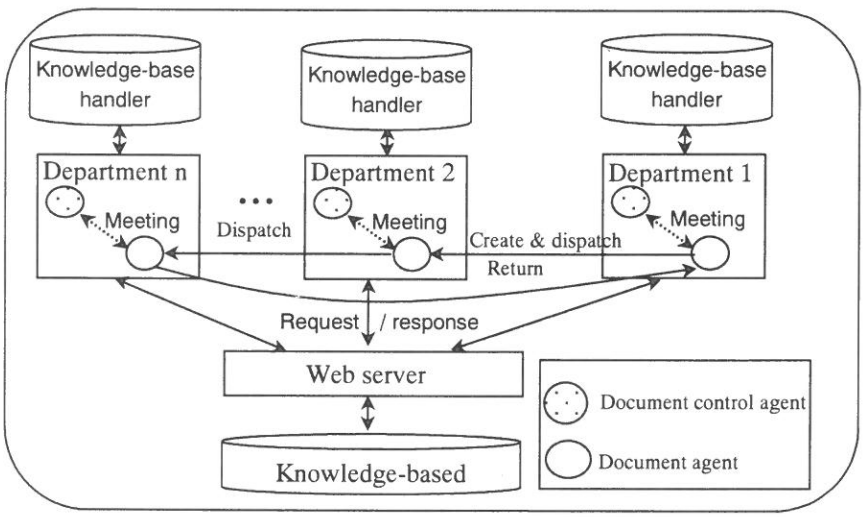

Figure 10 : External architecture of agent system

The document control agent that is the extend of the responsible agent is responsible for managing the document agent and the message agent to provide resources and services for agency. The document control agent dispatches a document agent to other agencies in order to request or supply a service. A user can control the document control agent by web browser. The document control agent monitors the missive through managing the document agent. The document agent extended the messenger agent is charged with the process of missive. It packs and processes the missive over

* A. Lingnau, O. Drobnik, and P. Detel. An Http-based Infrastructure for Mobile Agents. 1997. Available on http://www.tm.informatik.unifrankfurt.de/agents/ www-paper.html.

the Internet. The process order of the missive depends on its degree of emergency. If it is a normal missive, the document agent must make a meeting with others prior to make decision about the process order. If it is an emergency missive, the user can deal with the missive directly in time. The message agent inherited from the messenger agent provided the communication mechanism. The user of the business department can send messages through the message agent. The knowledge-base handler is the knowledge storage for reasoning mechanism in which the document control agent is committed, describing the services the agent provided, running time application/service, and the specific information.

A user can first use web browser to write a missive, and the agent system can later apply the TBCG Parser [23, 24] to parse the business logic of the missive. If the missive passes the parser, the document control agent may get a notification from the agent system and create a document agent to complete the mission of missive. The schedule of missive is determined through a meeting where the document control agent and document agent negotiate with one another. The chairman of the negotiation is the document control agent, and all of the document agents in the same context are the members of meeting. Based on the information regarding waiting time, degree of emergency, and type of missive, the meeting will choose the next document agent to deal with its missive. The negotiation mechanism is implemented by the multicasting technology of Aglet.

4.3 The scenario of document-driven agent system:

Each user of department of college first activates their document agent system, and then the agent system triggers the web browser. The user can manage their document (mobile) agent through the web browser. When the user wants to write a missive, he will have to choose the type of missive and the degree of emergency. The TBCG Parser will check the business logic of the missive and the roles participated this process. If there is any error occurred in the process of parser, the system will demand the user to make some

specific modification. Otherwise, the document control agent will create a document (mobile) agent to finish the process of missive. The document agent carries the missive to the destination office and queues the schedule along with other missives from another department. If the missive is an emergency missive, the document agent will create a new window and notify the user to deal with the missive in time. The missive sender can trace where the missive is and what the situations are. The situations of missive contain the arrival time, the finish time, the waiting time, and any exception event. The missive receiver can click the review function. If there are too many unread missives coming in to the receiver, the document agent will give the receiver a warning. If the receiver completes the review, the agent system will continue to route the missive based on the business logic and the knowledge of agent. If the user has any problem, he can send message to the system by message agent. Finally, the document agent takes the missive and the results back to the original sender.

4.4 The property of document-driven agent system

Using the mobile agent technology, a business document can be packed by a document agent. Thus, the document-driven agent system provides three properties: (1) trace ability: a function enables an administrator to monitor document processes easily, (2) document life cycle: a feature using mobile agent life cycle to manage document life cycle and concurrent processing, and (3) dynamic scheduling: this function contain two components: a document agent that can dynamically schedule its itinerary, and a document control agent that can dynamically schedule its services.

4.4.1 Trace ability

For missive sender, it is importance to know where the missive is and what the situations are. The situations of missive contain the arrival time, the finish time, the waiting time, and any exceptional event in a destination

department. The document agent routinely analyzes the information in order to plan the next route.

We use mobility listener of Aglet implementing the document agent to achieve the trace ability of agent system. The mobility listener can capture the event triggered by mobility reason. The types of event contain dispatching, retraction, activation, and deactivation. We also apply the locker pattern [3], an agent design pattern, to store the private information of the document agent, such as the beginning time, arrival time, and completing time of missive. The document control agent monitors where the missive is and what degree the missive completes through querying the document agent.

4.4.2 Document lifecycle

The lifecycle of a document agent is similar to the life cycle of Aglet. It includes create missive, copy missive, suspend missive, resume missive, and dispose missive. Each document agent encapsulates a document and manages its lifecycle. The lifecycle of a document agent is managed by the lifecycle of Aglet.

4.4.3 Dynamic scheduling

We use mobility technology to improve the internal architecture of ADEPT that enables agents to obtain the environment sensibility. The document control agent can dynamically change the schedule by perceiving the services, types, and amount of document agent. If many missives gathered in a department or a department is suspended, the document control will change its regular route to another department and come back to the previous department later. The document agent perceives their environment and responds in a timely fashion to any change that has occurred. For example, if the context of a department is restarting or shutting down, the document agent will be deactivated or move to another context.

5. Conclusion

In this paper, we have proposed an agent system approach, which applied the mobile agent technology to modify the architecture of ADEPT in order to enable the construction of business management process. We identified two key issues for the modification of architecture in the agent system: the external architecture influenced by the communication and negotiation between agents, and the internal architecture designed for the functionality of agent (e.g. for the BPM). Our intent is to improve the agent system in communication, agent life cycle and environment sensibility. In terms of communication, the mobility affects the external architecture of agent system in order to reduce the network loading and to make the communication between agents more flexible. The agent life cycle and the environment sensibility modify internal architecture of agent system that enables the dynamic schedule. The MADEPT approach proposed in this paper is a document-driven agent system, which encapsulates a single document per agent. Its strengths include: (1) trace ability: a function that enables administrators to monitor document processes easily, (2) document life cycle: a feature using agent life cycle to manage document life cycle and concurrent processing, and (3) dynamic scheduling: a document agent can dynamically schedule its itinerary, and a document control agent can dynamically schedule its services.

The MADEPT provided an architecture and process to develop the document-driven BPM system. It also supplied a mechanism for communication between departments of business.

Acknowledgement

The author wishes to express his thanks for the financial support of the Societas Verrbi Divini.

References:

(1) W.M.P. van der Aalst. On the automatic generation of workflow processes based on product structures. Computers in Industry, Vol. 39, pp. 97-111, 1999.

(2) A. Abecker, A Bernardi, H. Maus, M. Sintek, and C. Wenzel. Information Supply for Business Process: Coupling Workflow with Document Analysis and Information Retrieval. Knowledge-Based Systems, Vol. 13, pp. 271-284, 2000.

(3) Y, Aridor, and D. B. Lange. Agent Design Patterns: Elements of Agent Application design. In Proceedings of Agents'98, pp. 108-115, 1998.

(4) G. Cabri, L. Leonardi, and F. Zambonelli. Mobil-Agent Coordination Models for Internet Applications. IEEE Computer, pp.82-89, Feb. 2000.

(5) P.E. Clements, T. Papaioannou, J. Edwards. Aglets: Enabling the Virtual Enterprise. Engineering Publications Ltd, July 1997.

(6) D. Georgakopoulos and M. Hornick. An overview of Workflow Management: From Process Modeling to Workflow Automation. Distributed and Parallel Databases, Vol. 3, pp. 119-153, 1995.

(7) D. Georgakopolus, H. Schuster, A. Cichocki, and D. Baker. Manageing Process and Service Fusion in Virtual Enterprises. Information Systems, Vol. 24, No. 6, pp. 429-456. 1999.

(8) N. R. Jennings, P. Faratin, M. J. Johnson, T. J. Norman, P. O'Brien, and M. E. Wiegand: Agent-based business process management. International Journal of Cooperative Information Systems, 5 (2&3):105-130, 1996

(9) N. R. Jennings, P. Faratin, T. J. Norman, P. O'Brien, M. E. Wiegand, C. Voudouris, J. L. Alty, T. Miah, and E. H. Mamdani. ADEPT: Managing Business Processes using Intelligent Agents. Proc. BCS Expert Systems 96 Conference (ISIP Track), Cambridge, UK 5-23, 1996

(10) N. R. Jennings, T. J. Norman, and P. Faratin. ADEPT: An Agent-based Approach to Business Process Management. ACM SIGMOD Record 27 (4) 32-39, 1998

(11) N. R. Jennings, P. Faratin, T. J. Norman, P. O'Brien and B Odgers. Autonomous Agents for Business Process Management. Int. Journal of Applied Artificial Intelligence, 14(2):145-189, 2000.

(12) N. R. Jennings, P. Faratin, T. J. Norman, P. O'Brien, B. Odgers and, J. L. Alty. Implementing a Business Process Management System using ADEPT: A Real-World Case Study. Int. Journal of Applied Artificial Intelligence. 14(5):421-465, 2000.

(13) G. Karjoth, D.B. Lange, M. Oshima. A Security Model for Aglets. IEEE Internet Computing, 1(4):68-77, 1997.

(14) D.B. Lange and M. Oshima. Programming and Deploying Java Mobile Agents with Aglets. Addison-Wesley, 1998.

(15) F. Manola, S. Heiler, D. Georgakopoulos, M. Hornick, and M. Brodie. Distributed Object Management. International Journal of Intelligent and Cooperative Information Systems, Vol. 1, No. 1, Mar. 1992.

(16) T. J. Norman, N. R. Jennings, P. Faratin and, E. H. Mamdani. Designing and implementing a multi-agent architecture for business process management. Proceedings of the ECAI-96 Workshop on Agent Theories, Architectures, and Languages (ATAL-96), pages 149-161, 1996.

(17) T. Papaioannou and J. Edwards. Using Mobile Agents to Improve the Alignment Between Manufacturing and its IT Support Systems. Journal of Robotics and Autonomous Systems, 27: 45-57, 1999.

(18) T. Papaioannou and J. Edwards. Mobile Agent Technology in Support of Sales Order Processing in the Virtual Enterprise. Proc. of the BASYS'98 - 3rd IEEE/IFIP Int'l Conf. On Information Technology for BALANCED AUTOMATION SYSTEMS in Manufacturing, pages 23-32, 1998.

(19) T. Papaioannou and J. Edwards, Using Mobile Agents to Improve the

Alignment Between Manufacturing and its IT Systems. Journal of Robotics and Autonomous Systems, 27:45-57, 1999.

(20) Chong Xu, Dongbin Tao. Building Distributed Application with Aglet.1997.

(21) Four Dimensions of Interorganizational, Document-Oriented Workflow: A case Study of the Approval of Hazardous-Waste Disposal. Proceeding of 31 Hawaii International Conference, Vol. 4, pp. 332-341, 1998.

(22) 黃俊凱, 郭忠義, 范姜永益, 李允中。運用行動代理人技術於商業流程管理。第十一屆物件導向技術及應用研討會。八月，2000。

(23) 邱顯凱、徐國勛、李允中。應用 XML 透過概念圖形化工作基規格描述商業邏輯。第十一屆物件導向技術及應用研討會。八月，2000。

(24) 郭忠義、李允中。建構 XML 基虛擬企業模型：文件驅動代理人方法。第十二屆物件導向技術及應用研討會。台南成功大學。十二月，2001。

運用智慧型行動代理人技術於商業流程管理

郭 忠 義

輔仁大學 資訊工程學系

摘 要

隨著組織的快速發展與商業系統的日益複雜化，使得傳統設計方法並不能滿足目前網際網路上，商業流程管理系統對於分散式工作流的監督、控制和管理之複雜需求。本篇論文運用人工智慧與行動式代理人技術，以商業文件爲驅動導向，提出一個多重代理人系統方法以發展商業流程管理系統，我們稱之爲 MADEPT。針對代理人的溝通方式、生命週期與環境的認知能力修改 ADEPT 代理人發展架構。溝通方式改變代理人系統外部架構，生命週期與環境的認知能力改變代理人內部架構。MADEPT 將每件文件封裝成一個代理人，其特點有 (1)可追蹤能力：方便系統管理者對公文流程作追蹤；(2)管理文件的生命週期：利用代理人的生命週期管理文件的生命週期並且達成並行處理；(3)動態排程：透過行動式代理人對環境的認知能力，動態改變文件流程；對於提供服務者而言，可以根據環境的情況，改變服務的排程。最後我們利用 Aglet 實作一個以行動式代理人爲基礎之辦公室公文系統。

A Windows-Based Arbitrary Signal Generator

Ying-Wen Bai and Hong-Gi Wei

Department of Electronic Engineering
Fu Jen Catholic University
Taipei, Taiwan 242, R.O.C.

Abstract

This paper proposes the design and implementation of a Windows-based arbitrary signal generator. By using the friendly GUI (Graphical User Interface) from our implementation, users can adjust the period and amplitude of analog voltage waveforms with mouse clicks and drags. The data of the adjusted waveforms can be sent out to a D/A interface circuit by ISA bus system. To fulfill the programmable input and output functions, we use a low-cost PPI (Programmable Peripheral Interface) I/O chip 8255 as the data buffering and logic controller. The last stage of this implementation is the D/A hardware, converting digital data into analog voltage waveforms. Currently, we implement this signal generator by using very low-cost components in comparison with the cost of professional products. The experimental results show that the bandwidth of the signal generator can reach 50KHz that is the speed limitation of the programmable I/O chip 8255.

Key Words: Instrument, Signal Generator, GUI, Programmable I/O chip.

1. Introduction

A signal generator is an instrument for generating analog voltage waveforms, and these waveforms can be used to verify the design of electronic circuits. Over the past decades, numerous researchers have been working in different ways to improve the functions of signal generators. Many of them use computers to generate digital waveforms and then output them to D/A interface circuits to reconstruct the analog waveforms. However, due to the speed limitations of a computer I/O bus system, data buffer and D/A interface circuits, the bandwidth of a microcomputer-based signal generator can be limited. Fortunately, because of the progress of VLSI and microcomputer system technology, the bandwidth of D/A circuits can be extended beyond a couple of hundred MHz. In addition, the data buffer of a microcomputer system can reach the speed of a couple of hundred MHz. However, the speed of an I/O bus can still be a bottleneck for the real time operation from a continuous data flow, although the speed of I/O bus can reach several MHz [1-5].

From the previous speed comparison of major modules of a Windows-based signal generator, we learn that either we specify the lowest bandwidth of all modules as the bandwidth of the whole system, or we avoid the bandwidth limitation by tolerating the existence of a delay mechanism of the waveform generation. Because the speed of programmable I/O chips is the lowest among all modules, we use a high-speed first-in and first-out data buffer to improve the bandwidth of our signal generator.

In this design, we provide a friendly graphical user interface for preparing the patterns of the output signals. By using mouse clicks on the GUI, we can decide the waveforms to be generated. Later, the waveforms can be stored in a file for outputting to the I/O port for generating the analog waveforms [6-9].

The rest of this paper is organized as follows. In Section 2, the hardware architecture and waveform generation of the Windows-based arbitrary signal

generator is described. In Section 3, the software flowchart of this signal generator is presented. In Section 4, the performance improvement for an experimental system for our signal generator is presented. The last section draws conclusions.

2. Hardware Architecture and Waveform Generation of the Windows-based Arbitrary Signal Generator

Fig.1 shows the design for a Windows-based signal generator, where the digital data of the signal υ (t) is defined by the mouse operation on GUI. The digital data is output to the ISA bus interface and then to the address decoder because it shares the bus connection. To temporally store the digital data for the signal, we use a low-cost programmable I/O interface chip 8255 [10-13].

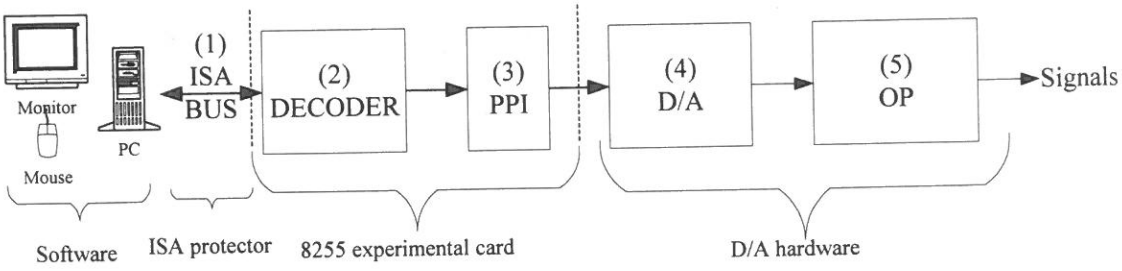

Fig.1 Block diagram of a Windows-based arbitrary signal generator

The bandwidth of the modules used in Fig.1 is as shown in Fig.2. Since the lowest bandwidth of the module in this system is 500KHz, we can obtain the whole system physical bandwidth at 50KHz if we use 10 sampling points to represent a whole period of the analog waveforms.

Fig.3 shows our GUI design of the Windows-based arbitrary signal generator [14-16]. This design provides users a straightforward operation style, so most users can create and edit the waveforms and then send out them within couple of seconds.

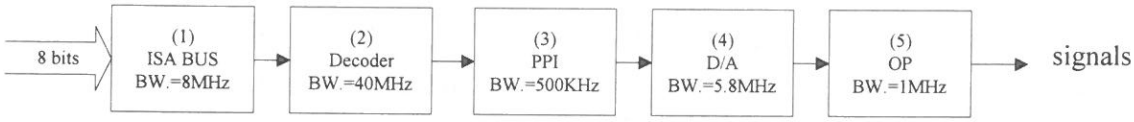

Fig.2 Bandwidth limitation of the low-cost signal generator

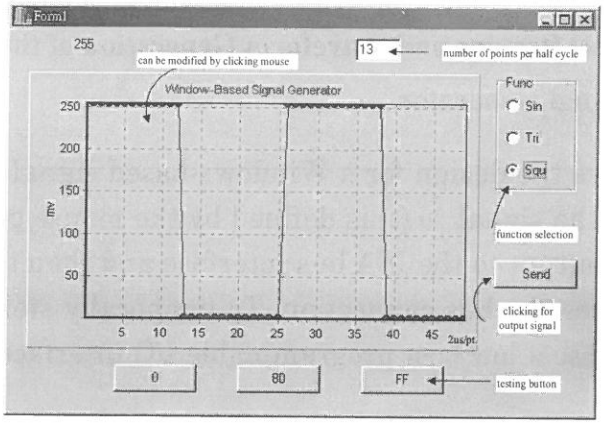

Fig.3 GUI for the Windows-based arbitrary signal generator

The operation of friendly GUI includes, function selection, waveform modification by mouse clicks and drags, and then sending output signals. Fig.4 shows a specific waveform that is modified from Fig.3 by mouse clicks and drags. In Fig 3 and 4, the vertical scale is 50 mV/div and the horizontal scale is 5 X 2us/div.

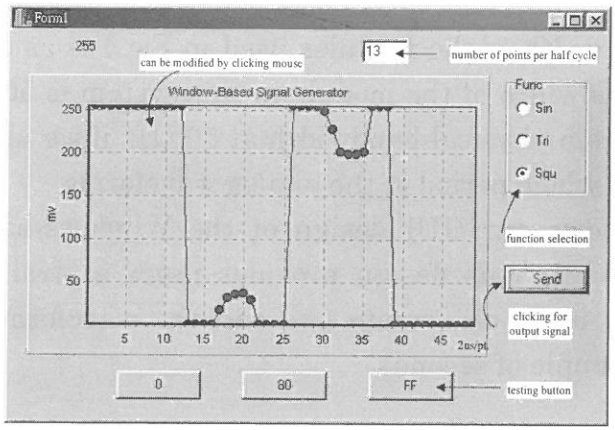

Fig.4 A specific waveform generated by mouse clicks and drags

Fig.5 shows a typical standard square waveform on an HP 54502A oscilloscope with the period 100us and 250 mV peak to peak from the waveform sending out in Fig. 3. Using the intuitive GUI in Fig.3, we can adjust the period and amplitude by mouse clicks and drags to develop any arbitrary waveform. The modified waveform in Fig.4 is measured by oscilloscope, as shown in Fig.6. The waveforms in both Fig. 4 and Fig. 6 are similar in period, amplitude and shape. Therefore, our primary goal for the hardware and software implementation of the Windows-based arbitrary signal generator with very low cost has been fulfilled.

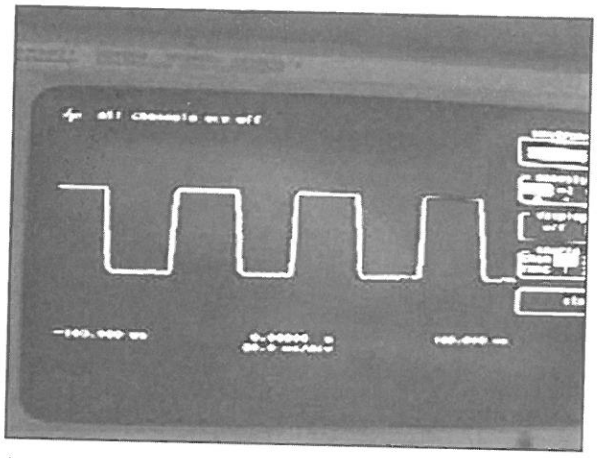

Fig.5 A standard square waveform shown on an oscilloscope

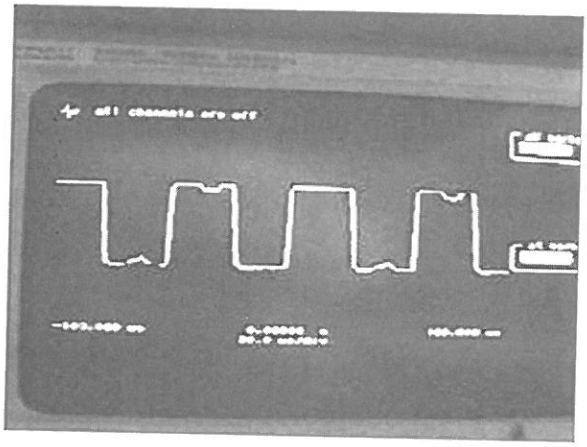

Fig. 6 A specific waveform modified by Windows-based user interface, as shown on an oscilloscope

3. Software Flowchart of an Windows-based Arbitrary Signal Generator

To implement the software module for a Windows-based interface, we use C++ Builder programming for GUI and use in-line assembly language to write inport/outport functions. The flowchart is as shown in Fig.7, indicating how to create a waveform by mouse clicks for selection functions, and output the digital data to the I/O port. Because this software mode is implemented by visual programming that uses event entry, there are many entry points that are not indicated in Fig.7. The source code can be seen in our technology report.

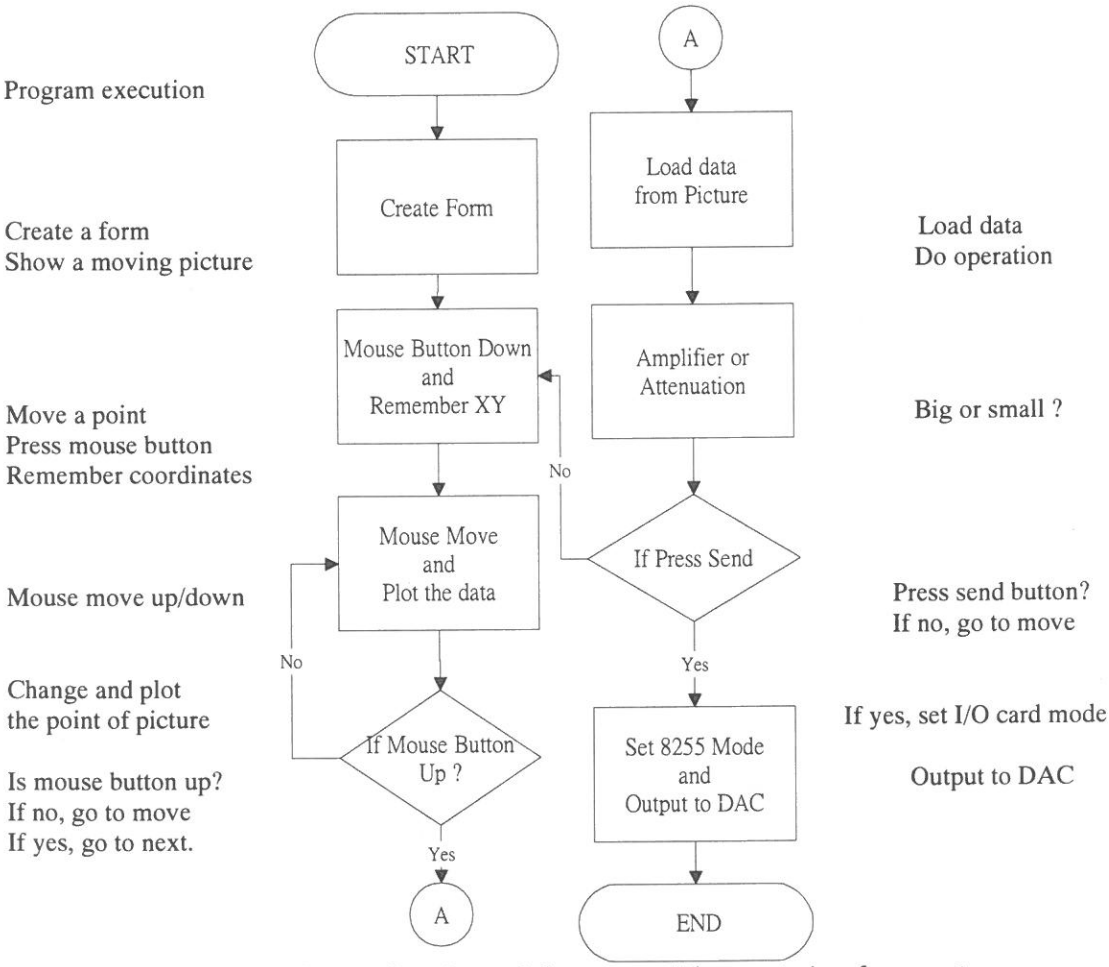

Fig.7 Software flowchart of the proposed low-cost signal generator

4. Performance Improvement for the Experimental Windows-based Arbitrary Signal Generator

The bandwidth limitation of each module is examined and compared, showing the bandwidth bottleneck of each module and the ratio between bandwidth and cost. The first part of the comparison is for the decoder, PPI, D/A and OP. The second part is for the computer I/O bus system that is about the time delay of digital signal output. Table 1 shows the bandwidth and cost for each module of our implementation of versions 1 and 2. In addition, the overall ratios between bandwidth (BW) and cost are presented. In the version 2 implementation, we use PCI bus standard with bus speed of 66MHz as shown in Table 2, so the physical bandwidth of the signal generator can be improved from 50KHz to 6.6MHz. However, the cost of hardware ICs will increase from $14 to $98 dollars. Table 2 shows the speed limits of the popular I/O BUS system in the computer industry; these bus speeds can be used as a candidate for the version 3 implementation.

Table 1 Bandwidth and cost for each module of the implementations

Version	Decoder	PPI	D/A	OP	BW/Cost	Physical BW/Cost
IC V1 BW. Cost	PAL16V8-25 40MHz $2	8255 500KHz $3	ADC7524 5.8MHz $6	AD544 1MHz $3	500KHz/$14	50KHz/$14
IC V2 BW. Cost	FPGA EPM9320LC84-15 PCI Bus: 66MHz $25		AD9768 100MHz $65	AD8048 240MHz $8	66MHz/$98	6.6MHz/$98

Table 2 Comparison among I/O bus systems.

BUS	Full Name	Bits	Speed of BUS (MHz)	Max.Data Transfer Rate (Mbytes/sec)
ISA	Industry Standard Architecture	8	8	8
EISA	Extended Industry Standard Architecture	16	8.33	33.32
MCA	Micro Channel Architecture bus	32	10	40
VESA	Video Electronics Standard Association	32	33	132
PCI	Peripheral Component Interconnection	32	33	132
AGP	Advanced Graphic Port	64	66	528
USB	Universal Serial Bus	1	1.5	0.1857

5. Conclusions

This paper proposes the design and implementation of a Windows-based arbitrary signal generator. It uses low cost experimental cards that can be easily accessed in a common circuit laboratory, and adds some inexpensive ICs to fulfill the basic functions of the interface hardware. For software, we use C++ Builder programming, because it is an RAD (Rapid Application Development) visual tool for Windows programming. Therefore, users can adjust the period and amplitude of analog voltage waveforms by friendly GUI with mouse clicks and drags. Subsequently, the sequential digital data is sent out to the ISA bus, decoder, PPI, D/A and finally to the OP. Using oscilloscope measurement, we obtain that the bandwidth of our experimental signal generator is only 50KHz due to the speed limitation of the programmable I/O chip 8255. However, the Windows-based signal generator that we built costs only a couple of U. S. dollars for the interface hardware, instead of a couple of hundred dollars for the commercial products. In addition, if we need higher bandwidth of signal generator, we can use higher speed ICs and a more expensive bus standard. Thus, the bandwidth of the signal generator can be in proportion to hardware cost.

Acknowledgment

The authors wish to express their thanks for the financial support of the Societas Verrbi Divini.

References:

(1) D.W. Olsen and M. J. Willis, "The Design of Windows-based Software for a PC-based, Low-cost Radar Video Signal Generator," Proceedings of the IEEE 1997 National Aerospace and Electronic Conference, Vol.2, pp.552-558, 1997.

(2) D. W. Olsen and M. J. Willis, "The Design of a PC-based, Low-cost Radar Video Signal Generator," Proceedings of IEEE 1997 National Aerospace and Electronics Conference, Vol.2, pp.544-551, 1997.
(3) M. Hasan, M. S. Iman, R. Sharma and S. A. Abbasi, "A Novel Design and FPGA Based Implementation of a Complex Synchronization Signal Generator for Television," IEEE Transactions on Consumer Electronics, pp.1143-1152, Nov.1997.
(4) S. Brigati, F. Francesconi, P. Malcovati, M Poletti and F. Malberti, "Digital Synthesis of Analog Signals for Audiometric Applications," Proceeding of IEEE 1997, International Symposium on Circuits and System, Vol.4, pp.2625-2627, 1997.
(5) L. Hernandez and A. Quesada, "Programmable Sine Wave Generator Employing a Mismatch-shaping DAC," IEEE International Conference on Eelectronics Circuits and System, Vol.1, pp.135-138, 1998.
(6) F. Palmer, "Integrating System Level Design and Instrumentation for Communications Development," Computer-Aided Design and Test for High-Speed Electronics, 52nd ARFTG Conference Digest, pp.140-156, 1998.
(7) K. Palomaki, J. Niittylahti and M. Renfors, "Numerical Sine and Cosine Synthesis Using a Complex Multiplier," Proceedings of IEEE International Symposium on Circuits and Systems, Vol.4, pp.365-359, 1999.
(8) Li Shuo, Long Teng, Li Fanghui and Tian Liyu, "Real Time Signal Waveform Library and Processing System Based on TMS320C5x DSP Starter Kit," Fourth International Conference on Signal Processing, Vol.2, pp.1662-1665, 1998.
(9) C. Narduzzi and C. Offelli, "Accuracy Characterization of Arbitrary Waveform Generators," Conference on Precision Electromagnetic Measurement Digest, pp.373-374, 1998.
(10) R.S.Varnes, J.A.R. Ball and N.H.Hancock, "A Dual-Output, Coherent Signal Generator Using Direct Digital Synthesis," Proceeding, Sensing, Processing, Networking, IMTC/97, Vol. 2, pp.1299-1304, 1997.

(11) F. X. Witkowski, P. A. Penksoke, R. Plonsey, D. T. Kaplan, M. L. Spano, W. L. Ditto, and K. M. Kavangh, "Development of a Nonlinearly Deterministic Signal Generator for Real Time Chaos Control Testing, " IEEE 17th Annual Conference on Engineering in Medicine and Biology Society, Vol.1, pp.287-288, 1997.

(12) G. Cavone, N. Giaquiato, M. Savino and A. Trotta, "Improved Sine-Wave Parameter Estimation for A/D Converter Testing," 8th Meditarranean Electromechanical Conference, pp.501-504, 1996.

(13) J. Hurll, "IEE Colloquium on Accreditation of RF Measurement," pp.4/1-4/6, 1993.

(14) C. P. Markahuser, "Computer-Aided Generation of Video Test Signals for Evaluation of Television Systems," IEEE Transaction on Consumer Electronics, Vol.373, pp.617-623, Aug.1991.

(15) Y. Xia, "A Programmable TV Sync Signal Generator," IEEE Transaction on Consumer Electronics, Vol.371, pp.57-65, Feb.1991.

(16) Walter Oney, System Programming for Windows 95, Microsoft Press, 1997.

視窗型任意波形產生器

白 英 文　　魏 鴻 祺
輔仁大學電子工程系

摘　要

這篇論文提出視窗型任意波形產生器設計和建構，採用親和式圖形人機介面程式設計，讓使用者操作滑鼠，以拖曳方式調整和編輯類比電壓波形週期和振幅，經過調整電壓波形資料由 ISA 匯流排送至數位/類比轉換介面電路，爲了完成可程式化輸入和輸出功能，我們採用低價位可規劃輸入和輸出介面晶片 8255 當作波形資料暫存和邏輯控制器，這個設計的最後一級是數位/類比轉換介面電路，將波形資料轉換成類比電壓波形。目前，我們的設計相較於工業產品便宜許多，實驗結果顯示，這個信號產生器頻寬爲 50KHz，這是因爲受限於可規劃輸入和輸出介面晶片 8255 頻寬速度。

關鍵詞：儀器，信號產生器，圖形人機介面，可規劃輸入和輸出介面晶片

製程能力指標 C_{pk} 大小順序判斷之研究

申 賢 英
輔仁大學數學研究所
陳 思 勉
輔仁大學數學系
許 玉 生
中央大學數學系

摘 要

當樣本數夠大且中央極限定理成立時，C_{pk} 的自然估計式 $\hat{C}_{pk}$ 近似常態分配，選擇最佳 C_{pk} 的問題可以 Gupta 之選擇方法解決（參考 Gupta（1965）（1984））。但實際的問題則往往受限於小樣本，此時 $\hat{C}_{pk}$ 之分佈十分複雜，用小樣本結果無法精確提供實際製程能力，故本文採用統計模擬方式，根據分別來自於三個不同製程之小樣本，用計算機模擬，估算正確判斷三個 C_{pk} 製程能力指標之順序達一定比率所需之樣本數。

關鍵詞：製程能力指標、製程期望值、製程標準差、選擇最佳製程

1. 簡　介

製程能力指標(Process Capability Index)量化製程能力，它結合了製程參數（μ，σ）和製程規格（LSL，T，USL），其中μ與σ分別爲製程特性分佈的期望值與標準差，USL與LSL分別爲製程上規格界限及下規格界限，而T則爲製程的目標值。藉由指標值的大小可評估出供應商製程能力之強弱，因此常被應用在購買決策上。

Kane (1986)提出的製程能力指標C_{pk}，其定義爲

$$C_{pk}=\frac{\min\{USL-\mu,\mu-LSL\}}{3\sigma}=\frac{d-|\mu-M|}{3\sigma},$$

其中M與d分別是規格上下界限的中點及一半長度。藉由製程能力指標C_{pk}我們可評估實際製程符合規格的程度以及製程能力的高低，因此供應商常以製程能力指標值做爲其製程能力的代表。自西元1986年起至今，此製程能力指標值普遍被應用於購買決策上，因此本研究著重在C_{pk}製程能力指標值，但本文的研究方法也適用於其他製程能力指標，如C_p、C_{pm}、C_{pmk}。

當決策依據是製程能力指標時，廠商在做購買決策最先考慮到的是"如何選出擁有最佳製程的供應商"，因此需要有最佳的選擇方法(Selection procedures)以茲配合。文獻上，選擇方法這個領域導源於1940年代，主要是爲了解決"如何由K個母群體中選出最佳母群體"的問題。當Wald(1947)在發展序貫分析(Sequential analysis)時，Girshick(1946)修正其技術方法並運用於探討兩個母群體的排序問題(Ranking Selection)，爾後被推廣爲K個母群體的排序問題。

選擇方法相關的研究文獻很多，其中一部分是在探討如何根據樣本的資訊，從K個常態分配的母群體中，找出具有最大期望值的母群體。其研究的方法是在這K組樣本所得的K個參數估計值中找出最大者，並將此對應之母群體假設爲具有最大參數母群體，然後求出此假設爲真的機率，並稱此機率爲"選擇正確之機率(probability of a correct selection)"。此機率與兩個變數有關，一爲最大參數和次大參數的實際差距，二爲樣本數的大小。文獻中提及了當最大參數和次大參數的實際差距已知的情形下，若欲達到指定的選擇正確之機率，如何計算出所需的樣本數，細節請參考Bechhofer(1954)，Gupta(1956,1965)。

本文將上述概念應用在購買決策上。假設廠商在做購買決策時，以供應商所提供的製程能力指標C_{pk}作爲判斷其製程能力高低的依據，而供應商的指標值資訊乃根據樣

本而來。當樣本數夠大且中央極限定理成立時的，我們由樣本所計算出的製程能力指標自然估計式$\hat{C}_{pk}$會趨近實際指標值，因此利用指標估計值的大小爲依據所做出的判斷決策正確的機會就很高。但是實際上供應商所提供的製程資訊，泰半是小樣本，此時$\hat{C}_{nk}$的分佈十分複雜，用小樣本結果無法精確提供實際製程能力。因此本文以統計模擬的方式透過製程能力指標C_{pk}研究製程之選擇，文中根據分別來自三個不同製程的小樣本，以計算機模擬，估算正確判斷三個C_{pk}製程能力指標值之順序達一定的比率所需之樣本數。

本論文探討正確判斷三個製程的製程能力指標大小順序(Right Order)的情形,細節將於第二節及第三節中討論，其中第二節討論製程特性服從常態分配時，製程參數、樣本數和正確決策率間的關係，第三節將探討參數未知時樣本數和正確決策率間的關係。第四節爲本研究之結論。

2. 樣本數和正確決策率間之關係的模擬研究

本文的研究方式主要是透過電腦模擬所產生的實驗數據加以分析。文中使用了 Fortran， IMSL 及 Excel 三種軟體，主要的數值計算是由 Fortran 執行，而實驗數據是利用 IMSL 所提供之亂數產生器所生成。在繪圖方面則使用 gnuplot 軟體。

由C_{pk}的定義可知在規格參數 d 與 M 固定時，C_{pk}的大小僅受製程期望值及製程標準差影響，而期望值與標準差分別可反映出該製程的集中趨勢和變異程度，因此我們可藉由指標值的大小判斷供應商製程能力的高低，進而做出決策。

假設製程穩定（under statistical control）且製程特性服從常態分配 $N(\mu, \sigma^2)$ 。在μ與σ^2均給定的情形下，我們將透過統計模擬的方式研究在多種不同製程水準之下，樣本的大小與正確決策率間的關係。

在$(\mu_x,\sigma_x^{\ 2}),(\mu_y,\sigma_y^{\ 2}),(\mu_z,\sigma_z^{\ 2})$均給定的情形下，三個製程的真正指標值$C_{pk}^x$、$C_{pk}^y$及$C_{pk}^z$亦可得知。假設（$X_1,\cdots,X_n$),($Y_1,\cdots,Y_n$),($Z_1,\cdots,Z_n$)分別代表來自$N(\mu_x,\sigma_x^{\ 2}),N(\mu_y,\sigma_y^{\ 2}),N(\mu_z,\sigma_z^{\ 2})$三組樣本數同爲 n 的獨立樣本，考慮三個製程的製程指標值之自然估計式（natural estimator）如下：

$$\hat{C}_{pk}^x=\frac{d-|\bar{X}-M|}{3S_x}\ ,\ \hat{C}_{pk}^y=\frac{d-|\bar{Y}-M|}{3S_y}\ ,\ \hat{C}_{pk}^z=\frac{d-|\bar{Z}-M|}{3S_z}\ ,$$

其中 $\overline{X}=\frac{\sum_{i=1}^{n}X_i}{n}$，$\overline{Y}=\frac{\sum_{j=1}^{n}Y_i}{n}$，$\overline{Z}=\frac{\sum_{k=1}^{n}Z_i}{n}$，

$S_x=\sqrt{\frac{\sum_{i=1}^{n}(X_i-\overline{X})^2}{n-1}}$，$S_y=\sqrt{\frac{\sum_{j=1}^{n}(Y_i-\overline{Y})^2}{n-1}}$，$S_z=\sqrt{\frac{\sum_{k=1}^{n}(Z_i-\overline{Z})^2}{n-1}}$ 。

根據所得之指標估計式，我們比較這三個指標估計值的大小順序及三個母群體的指標值大小順序。兩者之排序順序若相同，則表示透過該三組樣本可反映出三個製程真正的製程能力大小順序。否則，表示該三組樣本無法反映出真實的製程大小關係，很可能會導致錯誤的決策。爲了了解正確判斷的機率，我們將上述的步驟重覆 m 次（本論文中，令 m=1000），藉此計算出此 m 次模擬中正確決策率 R（參圖一），其中

R = 正確決策率 = 三個指標估計值的順序正確的次數/總實驗次數。

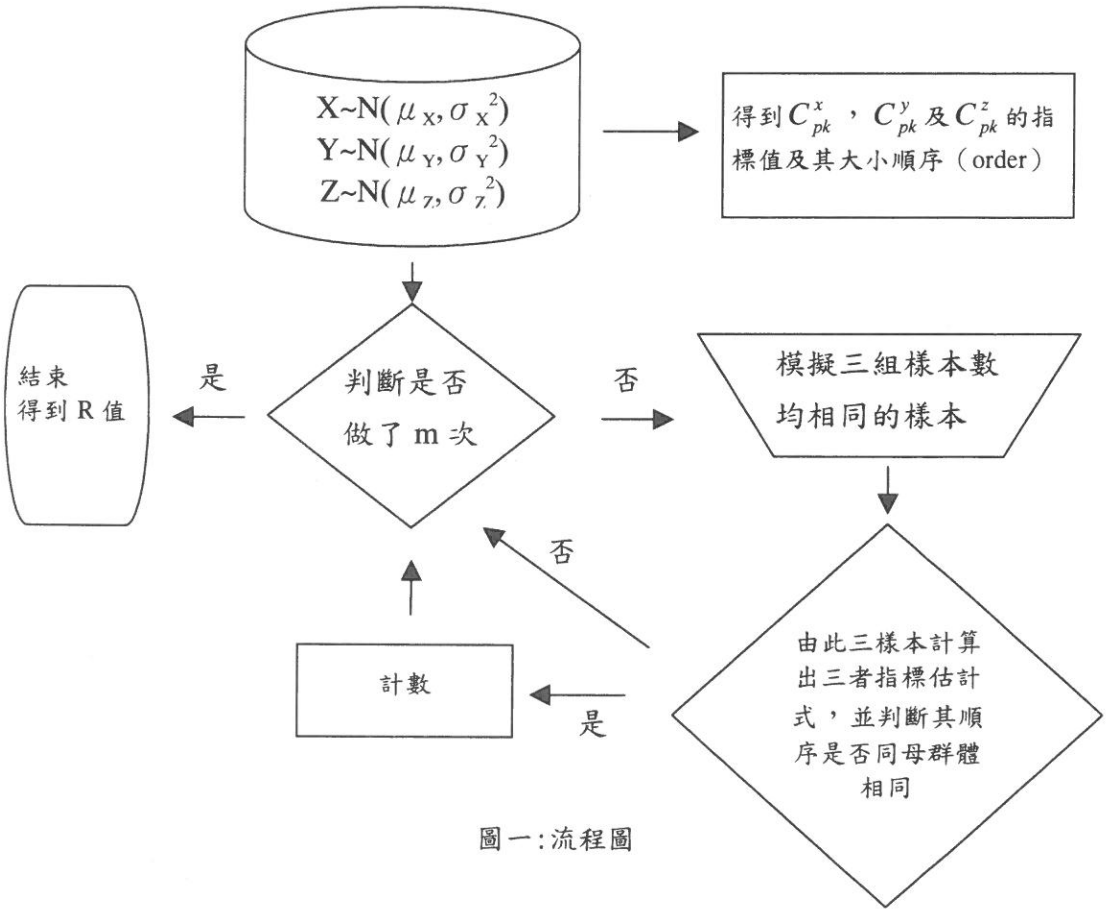

圖一：流程圖

由模擬的結果可出，當$\mu_x=\mu_y=\mu_z=T$ 時，在不同的製程變異之下當樣本數越大時，相對應的 R 亦增加，此乃因$\hat{C}_{pk}\rightarrow C_{pk}$之故。

同時，當σ_x，σ_y，σ_z的差距越大，R 的遞增速度亦加快，此乃因C_{pk}與標準差成反比之故，參圖二。

當三個製程期望值不相等，即部分偏離目標值 T 時，在製程變異相同的情形下，樣本數 n 與 R 則成正比的趨勢。當μ_x，μ_y，μ_z差距越大時，一開始 R 的增加速度相當快，但到達某種程度時,R 增加的速度便緩和下來。參圖三。

在固定的正確決策率 R 之下，分別定義三個製程指標值依序的差距如下：

$$\varepsilon_1 = \max\{C_{pk}^x\ ,\ C_{pk}^y\ ,\ C_{pk}^z\} - \mathrm{med}\{C_{pk}^x\ ,\ C_{pk}^y\ ,\ C_{pk}^z\}\ ,$$

$$\varepsilon_2 = \mathrm{med}\{C_{pk}^x\ ,\ C_{pk}^y\ ,\ C_{pk}^z\} - \min\{C_{pk}^x\ ,\ C_{pk}^y\ ,\ C_{pk}^z\}\ 。$$

當三個製程期望值全都等於目標值 T 時，指標值的差異則導因於製程變異。此處我們討論正確決策率 R 與所需之相對應樣本數之間的關係。爲方便表達之故，令 X 代表最佳製程，Y 代表次佳製程，Z 代表最劣製程，則$\varepsilon_1=C_{pk}^x-C_{pk}^y$，$\varepsilon_2=C_{pk}^y-C_{pk}^z$。在以下的討論中，假設最大的指標值$C_{pk}^x=2.08$，$\varepsilon_1$與$\varepsilon_2$之可能值爲 0.1，0.15，0.2，…，0.5，R 之可能值爲 0.5，0.6，0.7，0.8，0.9。

當三個樣本的製程期望值全在目標值 T 但是三個製程變異不同時，指標值值差ε_1，ε_2，所需之樣本數(n_a)及正確決策率 R 之間的關係於附表一。由附表一我們發現指標值值差大小與樣本數 n_a 呈反比。整體而言，在ε_2固定的情形下，當ε_1的取值由 0.1 遞增到 0.5 時，相對應的樣本數 n_a 呈現遞減的狀態。在固定ε_1的情形下ε_2亦有類似的結果。當 R 越大時，前者的遞減速率明顯大於後者，這是由於母群體的指標值$C_{pk}^x>C_{pk}^y>C_{pk}^z$之故。

當製程期望值(假設爲 5.5)不同於目標值時，令爲達到某預設的 R 時所需之樣本數稱爲 n_b。則樣本數 n_b 與 R，ε_1，ε_2 之間的變化關係列於附表二。就整體而言，樣本數 n_b 與指標值值差ε_1，ε_2間的變化關係與附表一十分類似。附表二所列出的樣本 n_b 皆比相對應於附表一的樣本數 n_a 大，且在 R 值越大時差異越顯著 (參表 I) 。

Sample size n	R=0.5	R=0.6	R=0.7	R=0.8	R=0.9
n_a（當 $\mu = T$）	147	247	382	592	965
n_b（當 $\mu \neq T$）	155	257	403	616	1012
$n_b - n_a$	8	10	21	24	47
n_b / n_a	1.054	1.040	1.054	1.040	1.048

表 I：當製程指標差值 $\varepsilon_1 = \varepsilon_2 = 0.1$，且製程期望值分別落在目標值上（$\mu = T$）與目標值外（$\mu \neq T$）時所需之樣本數 n_a 及 n_b

由表 I 可看出 $n_b / n_a \fallingdotseq 1.04 \sim 1.05$ 之間。在指標值值差 ε_1，ε_2 固定之下，附表一中與附表二中的真正指標值 C_{pk}^x、C_{pk}^y、C_{pk}^z 值固定 (分別爲 2.08、 1.98、 1.88)，所以兩表中製程值的大小皆受製程變異單一因素控制。因爲樣本數 n_b 大於樣本數 n_a，可見得當製程期望值偏離目標值時，三製程的製程變異高低較易判斷。若進一步探討，則可發現，當三個製程的期望值落在目標值外時，X、Y、Z 三個製程之製程變異差距較小，故較難做出正確判斷。

爲了找出適當的模型，我們繪出附表一中樣本數 n 與製程值差 ε_1，ε_2 的三維圖形 (參圖二)。由基礎的幾何學概念可知圖形可以 ε_1，ε_2 的冪次函數表之。爲取得最適合描述資料點的最適函數模型我們以迴歸分析中的校正後決定係數爲評斷標準。

當製程期望值落在目標值上時，樣本數 n、ε_1 與 ε_2 的曲面函數式如下：

R=0.5:

$$f(\varepsilon_1, \varepsilon_2) = -0.0287\varepsilon_1^{-2} - 0.0250\varepsilon_2^{-2} + 1.7357(\varepsilon_1\varepsilon_2)^{-1} - 1.2697\varepsilon_1^{-1} - 1.4537\varepsilon_2^{-1} + 5.3675$$

R=0.6:

$$f(\varepsilon_1, \varepsilon_2) = -0.0236\varepsilon_2^{-2} + 0.0009(\varepsilon_1\varepsilon_2)^{-2} + 2.6360(\varepsilon_1\varepsilon_2)^{-1} - 1.1107\varepsilon_1^{-1} - 1.6949\varepsilon_2^{-1} + 3.9174,$$

R=0.7:

$$f(\varepsilon_1, \varepsilon_2) = 0.4152\varepsilon_1^{-2} + 0.2384\varepsilon_2^{-2} + 0.0034(\varepsilon_1\varepsilon_2)^{-2} + 3.0535(\varepsilon_1\varepsilon_2)^{-1} - 2.2942\varepsilon_2^{-1} + 1.6527$$

R=0.8:

$$f(\varepsilon_1,\varepsilon_2)=1.7929\varepsilon_1^{-2}+1.2360\varepsilon_2^{-2}+0.0040(\varepsilon_1\varepsilon_2)^{-2}+2.8754(\varepsilon_1\varepsilon_2)^{-1}+1.1838\varepsilon_1^{-1}$$
$$-5.5680\varepsilon_2^{-1}+2.0895,$$

R=0.9:

$$f(\varepsilon_1,\varepsilon_2)=5.1776\varepsilon_1^{-2}+3.7020\varepsilon_2^{-2}-0.0127(\varepsilon_1\varepsilon_2)^{-2}+3.4929(\varepsilon_1\varepsilon_2)^{-1}-17.6272\varepsilon_2^{-1}+12.9793.$$

同理，根據附表二，當製程期望值不在目標值時（$\mu_x=\mu_y=\mu_z=5.5\neq5.0=T$），樣本數 n、$\varepsilon_1$與$\varepsilon_2$的曲面函數式如下：

R=0.5:

$$f(\varepsilon_1,\varepsilon_2)=-0.1448\varepsilon_1^{-2}-0.1540\varepsilon_2^{-2}+0.0006(\varepsilon_1\varepsilon_2)^{-2}+1.7803(\varepsilon_1\varepsilon_2)^{-1}+0.5835$$

R=0.6:

$$f(\varepsilon_1,\varepsilon_2)=-0.1215\varepsilon_1^{-2}-0.1251\varepsilon_2^{-2}+2.9436(\varepsilon_1\varepsilon_2)^{-1}-0.3841\varepsilon_1^{-1}-1.0639\varepsilon_2^{-1}+1.6132$$

R=0.7:

$$f(\varepsilon_1,\varepsilon_2)=0.1883\varepsilon_1^{-2}+0.1289\varepsilon_2^{-2}+0.0013(\varepsilon_1\varepsilon_2)^{-2}+3.7457(\varepsilon_1\varepsilon_2)^{-1}-1.7920\varepsilon_2^{-1}+0.8614$$

R=0.8:

$$f(\varepsilon_1,\varepsilon_2)=-1.4415\,\varepsilon_1^{-2}+1.3127\,\varepsilon_2^{-2}+0.0052\,(\varepsilon_1\varepsilon_2)^{-2}+3.0205\,(\varepsilon_1\varepsilon_2)^{-1}+3.0213\,\varepsilon_1^{-1}$$
$$-3.8783\,\varepsilon_2^{-1}-2.2055$$

R=0.9:

$$f(\varepsilon_1,\varepsilon_2)=5.1446\varepsilon_1^{-2}+4.5237\varepsilon_2^{-2}+0.0063(\varepsilon_1\varepsilon_2)^{-2}+7.2064\varepsilon_1^{-1}-9.0902\varepsilon_2^{-1}-4.7449$$

3. 參數未知時樣本數和正確決策率間之關係的模擬研究

在第二節中我們所討論的是在不同製程期望值和製程變異均給定時，樣本數 n 與正確決策率 R 之間的關係。此處,亦求得在固定的 R 之下配適度能達到 98%以上得以描述樣本數 n，ε_1與ε_2所構成的曲面函數式。爲了方便描述我們稱第二節中所得到的樣本值爲配適值。

在實務上，製程的參數通常是未知的，必須先透過樣本來估計製程參數，進而得到指標的估計值。因爲一般供應商所提供者大部份小樣本的製程資料，因此本節將只針對小樣本做討論。令供應商所提供之小樣本爲 n*，在已知最佳製程之製程指標值爲 2.08 的條件下(若最佳製程改變，則在其信賴區間內，我們可選擇許多分割點作類似分析)，實際指標值差的估計式爲三指標估計值的值差，以此爲依據求出爲達到固定 R 所需的樣本數 n，並比較其與附表一（或附表二）的差異，進而找出兩者之間的關係式，以便透過轉換的方式求得實際所需樣本數之範圍。

令來自 $N(\mu_x,\sigma_x^2),N(\mu_y,\sigma_y^2),N(\mu_z,\sigma_z^2)$ 的三組樣本數同爲 n*的獨立樣本爲 $(X_1,\cdots,X_{n^*}),(Y_1,\cdots,Y_{n^*}),(Z_1,\cdots,Z_{n^*})$ (考慮 n*=10，25，50，100)。透過這三組樣本所得的三個指標估計值之間的值差定義如下：

$$\hat{\varepsilon}_1 = \max\{\hat{C}_{pk}^x \ , \ \hat{C}_{pk}^y \ , \ \hat{C}_{pk}^z\} - \text{med}\{\hat{C}_{pk}^x \ , \ \hat{C}_{pk}^y \ , \ \hat{C}_{pk}^z\}$$

$$\hat{\varepsilon}_2 = \text{med}\{\hat{C}_{pk}^x \ , \ \hat{C}_{pk}^y \ , \ \hat{C}_{pk}^z\} - \min\{\hat{C}_{pk}^x \ , \ \hat{C}_{pk}^y \ , \ \hat{C}_{pk}^z\}$$

將$\hat{\varepsilon}_1$與$\hat{\varepsilon}_2$代入上節中所得的曲面函數式，得到爲達 R 所需的樣本數之估計。藉由這種模擬的方式，我們可以瞭解利用實際製程資料求出爲達指定 R 所需之樣本數和配適值間的差異性。

由附表三可知當廠商所提供的樣本之樣本數 n*爲 10 時，爲達到固定 R 所需的樣本值（在此令爲 n_{10}）均很小。以 R=0.9 爲例，（$\varepsilon_1,\varepsilon_2$）=(0.1,0.1)時所需的樣本也僅爲 127 個，而由附表一我們可得配適值爲 965 個，約爲附表三模擬結果之 8 倍。

爲了解決配適值與樣本值的差距，我們將附表一所得的結果，與附表三相除得到相對應樣本數之比例列於附表五。以 R＝0.5 爲例，將附表一及附表三相對應樣本數之比例(附表一/附表三)列於表 II。將表 II 的右上角與左下角拉出一條分隔線，我們可發現在此分隔線以下的部份比值均近似或小於 1.0，以上部份則呈遞增現象。由此可知，

當三個製程的資訊僅有 10 個樣本時，若實際製程差異微小，資訊將導致低估樣本數，而製程差異大到一定程度時，此資訊反而導致我們高估樣本數。

ε_2 \ ε_1		0.1	0.15	0.2	0.25	0.3	0.35	0.4	0.45	0.5
(Rn=0.5)	0.1	9.188	6.714	4.467	3.125	2.667	2.133	1.688	1.533	1.429
		6.267	4.063	2.938	2.250	1.933	1.600	1.429	1.214	1.071
	0.2	4.250	3.267	2.333	1.933	1.438	1.267	1.067	1.077	0.923
	0.25	3.400	2.643	2.071	1.438	1.286	1.143	0.929	0.857	0.769
	0.3	2.733	2.000	1.533	1.267	1.071	1.077	0.786	0.769	0.692
	0.35	2.429	1.786	1.333	1.143	0.929	0.923	0.769	0.750	0.615
	0.4	1.867	1.429	1.143	1.000	0.857	0.769	0.750	0.667	0.583
	0.45	1.846	1.357	1.154	0.923	0.714	0.75	0.667	0.583	0.636
	0.5	1.615	1.231	1.000	0.846	0.75	0.667	0.583	0.545	0.545

表 II：在 R=0.5，n*=10 時附表一及附表三相對應樣本數之比例(附表一/附表三)

表 II 之應用如下：若 n*=10 由廠商數據推算爲達 R=0.5 時平均樣本數爲 16，透過附表三可得所有可能產生 16 之值差（ε_1，ε_2）配對爲（0.1，0.1），（0.1，0.2），（0.15，0.15），（0.2，0.15），（0.25，0.1），（0.25，0.15），（0.25，0.25），（0.3，0.2），及（0.4，0.1）之間，再由表 II 可得比例分別爲 9.188，4.250，4.063，2.938，3.125，2.250，1.438，1.438 及 1.688。爲確保達到 R=0.5 的正確決策率所需之樣本數範圍約在（16*1.438，16*9.188）≒（24，147）之間。當製程資訊的取得來自於越大的樣本時，其精確度越高，因此確保達到 R 所需的樣本範圍越小。

由模擬結果我們發現，在 n*爲 10，25，50，100 逐步遞增時，經由模擬爲達固定的 R 所需的樣本數（在此依序稱爲 n_{10}， n_{25}， n_{50}，n_{100}）也隨之遞增，並逐漸趨近附表一。我們取 $\varepsilon_1 = \varepsilon_2 = 0.1$，R=0.5，…，0.9 時的結果並列於表 III：

Sample size n	R=0.5	R=0.6	R=0.7	R=0.8	R=0.9
n_{10}	16	28	40	66	127
n_{25}	22	37	62	104	191
n_{50}	32	53	83	136	241
n_{100}	41	71	109	175	320
配適值	147	247	382	592	965

表 III：製程期望值落在目標值上($\mu = T$)時，四種不同取樣數下模擬的結果($\varepsilon_1 = \varepsilon_2 = 0.1$)

爲了方便描述，我們將 R＝0.5 時，樣本數 n 與值差ε_1、ε_2的三維圖形與曲面函數式繪於圖二以做參考。將值差ε_1與ε_2代入與 R 相對應的曲面函數式，就可得到所需樣本數 n。

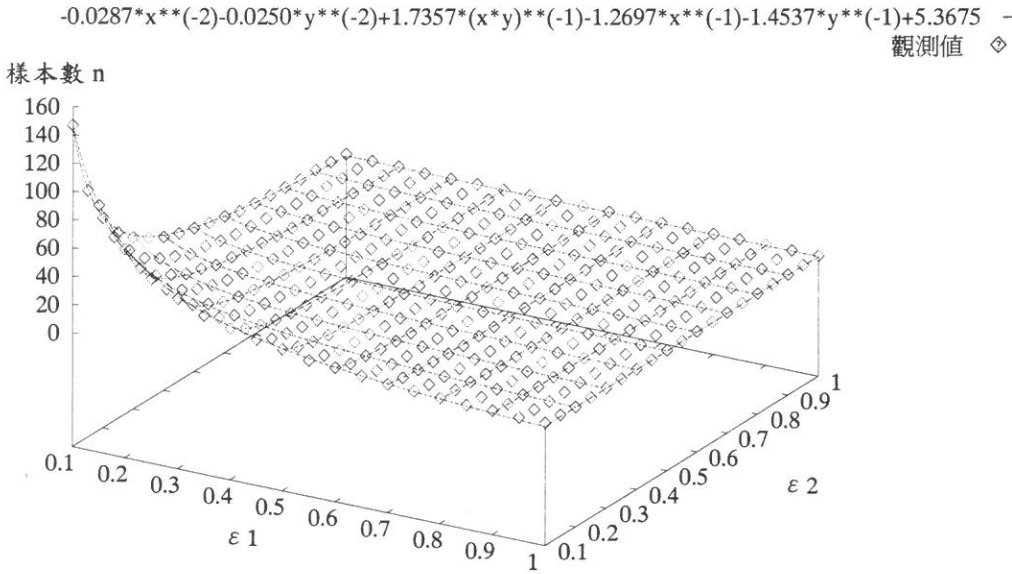

圖二：製程期望值在目標值上 R=0.5 時三製程值差與樣本數的三維圖形及其曲面函數式

當製程期望值在目標值外時，由模擬結果我們可看出，整體而言，樣本數的變化情形與製程期望值落在目標值時所得到的結果十分類似，但相對應的樣本數較大，顯然在實務上若製程偏離目標值，要達到正確的判斷需要較多的樣本，參考附表六。

4. 結　論

當廠商在做購買決策時，若以各個供應商所提出的製程能力指標值C_{pk}作爲判斷製程能力高低的依據，則需考慮到此時指標估計值是否能正確反映出實際製程能力大小順序，而指標估計值是根據小樣本而來，用大樣本結果無法精確提供實際製程能力。因此本文藉由電腦模擬的方式來瞭解在小樣本下製程參數、樣本數及正確決策率三者之間的關係。

參考文獻：

(1) Bechhofer, R. E. (1954). " A Single-Sample Multiple Decision Procedure for Ranking Means of Normal Populations with Known Variance," *Annals of Mathematical Statistics, vol.25, pp.16-39.*

(2) Bjornstad, J. F. (1985). "Asymptotic Consistency Of Procedures For Selecting Good Populations," *Communication in Statistics –Theory and Methods, vol. 14(7), pp.1659-1688.*

(3) Girshick, M. A. (1946). Contributions to the theory of sequential analysis, II, III. *Ann. Math. Statist. , Vol.17, pp.282-298.*

(4) Gupta, S. S. (1956). "On a decision rule for a problem in ranking means," *Ph.D. Thesis (Mimeo. Ser. No. 150). Institute of Statistics, University of North Carolina, Chapel Hill.*

(5) Gupta, S. S. (1965), "On Some Multiple Decision (Selection and Ranking) Rules," *Technometrics, vol.7, pp.225-245.*

(6) Gupta, S. S. and Miescke, K. J. (1984). "Sequential Selection Procedures – A Decision Theoretic Approach," *Annals of Statistics, vol.12 , pp. 336-350.*

(7) Huang, D.Y. and Lee, R.F. (1995). "Selecting the Largest Capability Index from Several Quality Control Processes," *Journal of Statistical Planning and Inference, vol.46, pp.335-346.*

(8) Kotz, S. and Johnson, N.L. (1993). "Process Capability Indices," Chapman and Hall.

(9) Kotz, S. Lovelace, C.R. (1998). "Process Capability Indices in Theory and Practice," Arnold.

(10) Somerville, P. N. (1985) " New Subset Selection Method for Normal Populations," *Journal of Statistical Computation and Simulation, vol.22, pp.27-50*

(11) Wald, A. (1947). "Sequential Analysis," Wiley, New York.

	ε_2 \ ε_1	0.1	0.15	0.2	0.25	0.3	0.35	0.4	0.45	0.5
(Rn=0.5)	0.1	147	94	67	50	40	32	27	23	20
	0.15	94	65	47	36	29	24	20	17	15
	0.2	68	49	35	29	23	19	16	14	12
	0.25	51	37	29	23	18	16	13	12	10
	0.3	41	30	23	19	15	14	11	10	9
	0.35	34	25	20	16	13	12	10	9	8
	0.4	28	20	16	14	12	10	9	8	7
	0.45	24	19	15	12	10	9	8	7	7
	0.5	21	16	13	11	9	8	7	6	6
(Rn=0.6)	0.1	247	158	111	86	68	57	47	41	34
	0.15	158	107	78	60	48	39	33	29	24
	0.2	115	79	58	45	37	31	26	22	19
	0.25	90	62	46	36	30	25	21	18	16
	0.3	74	51	38	30	25	21	18	15	13
	0.35	60	42	32	25	20	18	15	13	12
	0.4	52	36	28	22	19	16	14	12	10
	0.45	45	32	24	20	16	14	12	10	9
	0.5	42	28	22	17	15	13	11	9	8
(Rn=0.7)	0.1	382	248	180	140	118	97	83	74	67
	0.15	257	165	121	95	76	63	54	46	41
	0.2	188	124	92	71	57	47	39	34	30
	0.25	154	99	72	56	45	38	32	27	24
	0.3	131	81	59	46	37	32	26	23	20
	0.35	117	71	52	40	33	27	23	20	17
	0.4	104	64	46	35	28	24	20	17	15
	0.45	101	57	40	31	25	21	18	15	13
	0.5	93	53	36	28	22	19	16	14	12
(Rn=0.8)	0.1	592	385	298	237	204	186	170	155	148
	0.15	403	253	188	147	122	104	89	79	70
	0.2	318	194	138	107	87	72	63	55	49
	0.25	275	159	112	85	68	57	49	42	37
	0.3	260	139	95	71	58	48	40	34	30
	0.35	249	128	85	62	50	40	34	29	25
	0.4	247	118	77	56	44	36	30	26	22
	0.45	243	114	71	51	39	32	27	23	20
	0.5	239	113	68	48	36	29	24	21	18
(Rn=0.9)	0.1	965	644	510	452	414	394	367	344	327
	0.15	695	411	298	241	202	183	165	150	142
	0.2	611	328	220	169	138	118	102	92	81
	0.25	579	285	183	136	108	89	76	67	59
	0.3	579	270	165	118	90	74	62	53	46
	0.35	584	259	154	106	80	64	52	45	38
	0.4	591	259	148	99	74	58	47	39	34
	0.45	574	257	150	98	69	54	43	36	30
	0.5	584	265	150	94	66	51	41	34	28

附表一：製程期望值落在目標值上時，為達到指定的正確決策率 Rn 時所需之樣本數 n_a

	ε_2 \ ε_1	0.1	0.15	0.2	0.25	0.3	0.35	0.4	0.45	0.5
(Rn=0.5)	0.1	155	100	73	55	43	35	29	25	21
	0.15	100	67	51	39	31	26	22	19	17
	0.2	73	51	39	31	25	21	18	16	14
	0.25	56	39	31	25	20	18	15	13	11
	0.3	43	32	25	21	18	15	13	11	10
	0.35	36	27	21	17	15	13	11	10	9
	0.4	30	23	19	15	13	11	10	9	8
	0.45	26	20	16	13	12	10	9	8	7
	0.5	22	17	14	12	10	9	8	7	6
(Rn=0.6)	0.1	257	167	120	92	72	61	50	44	37
	0.15	170	114	83	62	51	43	36	31	27
	0.2	122	85	63	48	41	33	28	24	21
	0.25	96	66	49	39	32	27	23	20	18
	0.3	80	54	40	33	27	23	20	17	15
	0.35	64	45	34	28	23	19	17	15	13
	0.4	56	39	30	24	20	17	15	13	11
	0.45	49	34	26	21	18	15	13	12	10
	0.5	43	30	24	19	16	14	12	11	10
(Rn=0.7)	0.1	403	258	194	152	125	106	88	79	71
	0.15	269	174	129	101	80	67	59	51	44
	0.2	200	129	96	75	61	52	44	38	33
	0.25	163	104	77	60	49	41	34	30	26
	0.3	139	87	65	49	40	34	29	25	22
	0.35	122	74	55	43	35	29	25	21	19
	0.4	110	66	48	38	30	26	22	19	17
	0.45	105	61	44	34	27	22	19	17	15
	0.5	100	57	39	30	25	21	17	15	14
(Rn=0.8)	0.1	616	415	312	254	221	200	177	170	157
	0.15	425	265	195	156	129	109	97	87	79
	0.2	338	203	148	114	94	78	69	60	53
	0.25	287	167	118	92	73	61	52	46	41
	0.3	266	147	101	76	62	52	43	37	32
	0.35	262	134	88	68	53	43	37	33	28
	0.4	258	124	82	60	47	39	33	28	24
	0.45	257	119	75	55	42	35	29	26	22
	0.5	261	122	72	51	39	31	27	23	20
(Rn=0.9)	0.1	1012	686	547	483	449	425	407	380	370
	0.15	720	438	326	261	227	203	188	175	163
	0.2	628	343	238	190	154	132	116	107	96
	0.25	612	299	196	148	120	101	86	76	69
	0.3	612	283	176	126	99	83	70	61	54
	0.35	617	275	163	116	88	71	60	51	45
	0.4	608	272	160	107	80	64	52	45	38
	0.45	602	270	151	101	75	58	48	40	34
	0.5	615	272	155	100	71	55	44	37	31

附表二：製程期望值落在目標值外時，為達到指定的正確決策率 Rn 時所需之樣本數 n_b

	ε_2 \ ε_1	0.1	0.15	0.2	0.25	0.3	0.35	0.4	0.45	0.5
(Rn=0.5)	0.1	16	14	15	16	15	15	16	15	14
	0.15	15	16	16	16	15	15	14	14	14
	0.2	16	15	15	15	16	15	15	13	13
	0.25	15	14	14	16	14	14	14	14	13
	0.3	15	15	15	15	14	13	14	13	13
	0.35	14	14	15	14	14	13	13	12	13
	0.4	15	14	14	14	14	13	12	12	12
	0.45	13	14	13	13	14	12	12	12	11
	0.5	13	13	13	13	12	12	12	11	11
(Rn=0.6)	0.1	28	24	25	25	24	25	24	23	23
	0.15	24	23	25	25	24	23	25	22	22
	0.2	24	24	24	24	24	22	22	22	21
	0.25	23	23	25	22	22	22	21	22	20
	0.3	24	23	22	23	22	22	22	21	20
	0.35	22	23	24	21	22	20	20	19	20
	0.4	23	23	23	22	22	21	20	19	19
	0.45	23	21	22	20	20	19	19	17	17
	0.5	22	21	19	20	19	18	19	16	16
(Rn=0.7)	0.1	40	41	39	39	39	38	39	35	38
	0.15	39	40	40	38	40	36	37	37	37
	0.2	39	39	41	38	39	39	37	36	37
	0.25	40	41	38	39	37	37	36	35	34
	0.3	40	37	40	36	37	37	38	34	32
	0.35	37	39	35	37	36	35	35	32	31
	0.4	38	36	35	35	35	32	33	31	29
	0.45	36	35	34	33	34	32	29	29	27
	0.5	32	32	33	31	32	31	29	28	28
(Rn=0.8)	0.1	66	72	70	66	69	68	66	62	63
	0.15	70	69	66	66	66	66	62	65	64
	0.2	66	68	70	68	71	70	68	63	60
	0.25	68	65	63	68	62	63	63	57	61
	0.3	66	68	65	64	66	60	58	55	57
	0.35	66	62	64	64	61	63	59	58	55
	0.4	62	65	62	61	61	54	58	56	50
	0.45	63	62	56	59	58	52	54	49	50
	0.5	59	58	59	56	53	50	52	49	47
(Rn=0.9)	0.1	127	124	129	132	114	129	130	123	117
	0.15	126	129	137	118	132	131	125	124	116
	0.2	133	125	126	122	122	121	122	122	116
	0.25	128	132	131	131	125	125	117	113	106
	0.3	129	127	122	124	118	115	118	114	111
	0.35	130	124	124	119	112	111	105	106	100
	0.4	123	120	122	118	112	108	113	104	102
	0.45	117	118	130	115	110	107	106	102	101
	0.5	121	115	117	112	108	106	104	100	91

附表三：製程期望值落在目標值上，n*=10 之下，樣本數 n 與正確決策率 Rn 的關係

	ε_2 \ ε_1	0.1	0.15	0.2	0.25	0.3	0.35	0.4	0.45	0.5
(Rn=0.5)	0.1	16	16	17	16	16	17	16	15	14
	0.15	16	15	16	16	16	16	16	15	14
	0.2	16	16	16	16	17	16	15	14	14
	0.25	15	15	15	15	15	14	15	14	14
	0.3	15	15	15	15	14	14	14	14	12
	0.35	16	15	15	15	14	14	14	13	13
	0.4	15	15	15	15	14	14	14	13	12
	0.45	14	14	14	14	13	13	12	12	11
	0.5	14	14	14	14	12	12	12	11	11
(Rn=0.6)	0.1	27	27	26	26	24	25	24	24	24
	0.15	25	26	25	26	25	23	25	23	23
	0.2	26	26	24	26	25	23	24	23	22
	0.25	25	25	25	25	24	25	22	23	22
	0.3	23	24	25	24	24	22	23	20	21
	0.35	25	23	24	24	22	21	22	20	19
	0.4	23	24	23	22	22	21	20	20	20
	0.45	24	23	22	21	20	20	20	19	19
	0.5	22	22	21	21	20	20	20	20	17
(Rn=0.7)	0.1	43	43	42	40	41	42	40	40	41
	0.15	40	42	42	42	43	39	39	40	39
	0.2	40	42	39	41	38	40	39	41	36
	0.25	41	42	40	41	39	38	37	36	34
	0.3	42	39	38	40	38	38	36	37	34
	0.35	40	38	38	40	37	34	32	32	32
	0.4	37	37	38	37	35	36	35	34	32
	0.45	37	37	37	35	35	33	31	31	28
	0.5	36	34	35	34	32	31	32	31	30
(Rn=0.8)	0.1	71	70	74	72	71	73	71	68	64
	0.15	72	74	75	73	70	68	66	70	67
	0.2	73	70	72	70	73	74	72	65	64
	0.25	70	71	69	69	70	65	69	67	60
	0.3	69	69	68	69	67	69	65	65	58
	0.35	67	70	66	67	67	65	60	62	59
	0.4	67	65	69	68	66	63	61	60	54
	0.45	67	65	64	64	61	57	55	56	54
	0.5	66	64	62	57	57	59	54	51	48
(Rn=0.9)	0.1	143	139	147	143	138	143	138	133	133
	0.15	144	135	138	142	132	127	134	125	140
	0.2	141	139	141	146	135	137	129	132	130
	0.25	142	135	133	131	138	140	128	130	120
	0.3	140	145	139	127	130	129	125	128	130
	0.35	132	138	135	129	122	124	126	117	113
	0.4	134	132	128	123	120	127	122	113	118
	0.45	130	130	126	120	122	116	113	113	111
	0.5	128	132	118	125	113	111	119	114	99

附表四：製程期望值落在目標值外，$n^*=10$ 之下，樣本數 n 與正確決策率 Rn 的關係

ε_2 \ ε_1		0.1	0.15	0.2	0.25	0.3	0.35	0.4	0.45	0.5
(Rn=0.5)	0.1	9.188	6.714	4.467	3.125	2.667	2.133	1.688	1.533	1.429
	0.15	6.267	4.063	2.938	2.25	1.933	1.6	1.429	1.214	1.071
	0.2	4.25	3.267	2.333	1.933	1.438	1.267	1.067	1.077	0.923
	0.25	3.4	2.643	2.071	1.438	1.286	1.143	0.929	0.857	0.769
	0.3	2.733	2	1.533	1.267	1.071	1.077	0.786	0.769	0.692
	0.35	2.429	1.786	1.333	1.143	0.929	0.923	0.769	0.75	0.615
	0.4	1.867	1.429	1.143	1	0.857	0.769	0.75	0.667	0.583
	0.45	1.846	1.357	1.154	0.923	0.714	0.75	0.667	0.583	0.636
	0.5	1.615	1.231	1	0.846	0.75	0.667	0.583	0.545	0.545
(Rn=0.6)	0.1	8.821	6.583	4.44	3.44	2.833	2.28	1.958	1.783	1.478
	0.15	6.583	4.652	3.12	2.4	2	1.696	1.32	1.318	1.091
	0.2	4.792	3.292	2.417	1.875	1.542	1.409	1.182	1	0.905
	0.25	3.913	2.696	1.84	1.636	1.364	1.136	1	0.818	0.8
	0.3	3.083	2.217	1.727	1.304	1.136	0.955	0.818	0.714	0.65
	0.35	2.727	1.826	1.333	1.19	0.909	0.9	0.75	0.684	0.6
	0.4	2.261	1.565	1.217	1	0.864	0.762	0.7	0.632	0.526
	0.45	1.957	1.524	1.091	1	0.8	0.737	0.632	0.588	0.529
	0.5	1.909	1.333	1.158	0.85	0.789	0.722	0.579	0.563	0.5
(Rn=0.7)	0.1	9.55	6.049	4.615	3.59	3.026	2.553	2.128	2.114	1.763
	0.15	6.59	4.125	3.025	2.5	1.9	1.75	1.459	1.243	1.108
	0.2	4.821	3.179	2.244	1.868	1.462	1.205	1.054	0.944	0.811
	0.25	3.85	2.415	1.895	1.436	1.216	1.027	0.889	0.771	0.706
	0.3	3.275	2.189	1.475	1.278	1	0.865	0.684	0.676	0.625
	0.35	3.162	1.821	1.486	1.081	0.917	0.771	0.657	0.625	0.548
	0.4	2.737	1.778	1.314	1	0.8	0.75	0.606	0.548	0.517
	0.45	2.806	1.629	1.176	0.939	0.735	0.656	0.621	0.517	0.481
	0.5	2.906	1.656	1.091	0.903	0.688	0.613	0.552	0.5	0.429
(Rn=0.8)	0.1	8.97	5.347	4.257	3.591	2.957	2.735	2.576	2.5	2.349
	0.15	5.757	3.667	2.848	2.227	1.848	1.576	1.435	1.215	1.094
	0.2	4.818	2.853	1.971	1.574	1.225	1.029	0.926	0.873	0.817
	0.25	4.044	2.446	1.778	1.25	1.097	0.905	0.778	0.737	0.607
	0.3	3.939	2.044	1.462	1.109	0.879	0.8	0.69	0.618	0.526
	0.35	3.773	2.065	1.328	0.969	0.82	0.635	0.576	0.5	0.455
	0.4	3.984	1.815	1.242	0.918	0.721	0.667	0.517	0.464	0.44
	0.45	3.857	1.839	1.268	0.864	0.672	0.615	0.5	0.469	0.4
	0.5	4.051	1.948	1.153	0.857	0.679	0.58	0.462	0.429	0.383
(Rn=0.9)	0.1	7.598	5.194	3.953	3.424	3.632	3.054	2.823	2.797	2.795
	0.15	5.516	3.186	2.175	2.042	1.53	1.397	1.32	1.21	1.224
	0.2	4.594	2.624	1.746	1.385	1.131	0.975	0.836	0.754	0.698
	0.25	4.523	2.159	1.397	1.038	0.864	0.712	0.65	0.593	0.557
	0.3	4.488	2.126	1.352	0.952	0.763	0.643	0.525	0.465	0.414
	0.35	4.492	2.089	1.242	0.891	0.714	0.577	0.495	0.425	0.38
	0.4	4.805	2.158	1.213	0.839	0.661	0.537	0.416	0.375	0.333
	0.45	4.906	2.178	1.154	0.852	0.627	0.505	0.406	0.353	0.297
	0.5	4.826	2.304	1.282	0.839	0.611	0.481	0.394	0.34	0.308

附表五：n*=10 時附表一及附表三相對應樣本數之比例(附表一/附表三)

	ε_2 \ ε_1	0.1	0.15	0.2	0.25	0.3	0.35	0.4	0.45	0.5
(Rn=0.5)	0.1	9.688	6.25	4.294	3.438	2.688	2.059	1.813	1.667	1.5
	0.15	6.25	4.467	3.188	2.438	1.938	1.625	1.375	1.267	1.214
	0.2	4.563	3.188	2.438	1.938	1.471	1.313	1.2	1.143	1
	0.25	3.733	2.6	2.067	1.667	1.333	1.286	1	0.929	0.786
	0.3	2.867	2.133	1.667	1.4	1.286	1.071	0.929	0.786	0.833
	0.35	2.25	1.8	1.4	1.133	1.071	0.929	0.786	0.769	0.692
	0.4	2	1.533	1.267	1	0.929	0.786	0.714	0.692	0.667
	0.45	1.857	1.429	1.143	0.929	0.923	0.769	0.75	0.667	0.636
	0.5	1.571	1.214	1	0.857	0.833	0.75	0.667	0.636	0.545
(Rn=0.6)	0.1	9.519	6.185	4.615	3.538	3	2.44	2.083	1.833	1.542
	0.15	6.8	4.385	3.32	2.385	2.04	1.87	1.44	1.348	1.174
	0.2	4.692	3.269	2.625	1.846	1.64	1.435	1.167	1.043	0.955
	0.25	3.84	2.64	1.96	1.56	1.333	1.08	1.045	0.87	0.818
	0.3	3.478	2.25	1.6	1.375	1.125	1.045	0.87	0.85	0.714
	0.35	2.56	1.957	1.417	1.167	1.045	0.905	0.773	0.75	0.684
	0.4	2.435	1.625	1.304	1.091	0.909	0.81	0.75	0.65	0.55
	0.45	2.042	1.478	1.182	1	0.9	0.75	0.65	0.632	0.526
	0.5	1.955	1.364	1.143	0.905	0.8	0.7	0.6	0.55	0.588
(Rn=0.7)	0.1	9.372	6	4.619	3.8	3.049	2.524	2.2	1.975	1.732
	0.15	6.725	4.143	3.071	2.405	1.86	1.718	1.513	1.275	1.128
	0.2	5	3.071	2.462	1.829	1.605	1.3	1.128	0.927	0.917
	0.25	3.976	2.476	1.925	1.463	1.256	1.079	0.919	0.833	0.765
	0.3	3.31	2.231	1.711	1.225	1.053	0.895	0.806	0.676	0.647
	0.35	3.05	1.947	1.447	1.075	0.946	0.853	0.781	0.656	0.594
	0.4	2.973	1.784	1.263	1.027	0.857	0.722	0.629	0.559	0.531
	0.45	2.838	1.649	1.189	0.971	0.771	0.667	0.613	0.548	0.536
	0.5	2.778	1.676	1.114	0.882	0.781	0.677	0.531	0.484	0.467
(Rn=0.8)	0.1	8.676	5.929	4.216	3.528	3.113	2.74	2.493	2.5	2.453
	0.15	5.903	3.581	2.6	2.137	1.843	1.603	1.47	1.243	1.179
	0.2	4.63	2.9	2.056	1.629	1.288	1.054	0.958	0.923	0.828
	0.25	4.1	2.352	1.71	1.333	1.043	0.938	0.754	0.687	0.683
	0.3	3.855	2.13	1.485	1.101	0.925	0.754	0.662	0.569	0.552
	0.35	3.91	1.914	1.333	1.015	0.791	0.662	0.617	0.532	0.475
	0.4	3.851	1.908	1.188	0.882	0.712	0.619	0.541	0.467	0.444
	0.45	3.836	1.831	1.172	0.859	0.689	0.614	0.527	0.464	0.407
	0.5	3.955	1.906	1.161	0.895	0.684	0.525	0.5	0.451	0.417
(Rn=0.9)	0.1	7.077	4.935	3.721	3.378	3.254	2.972	2.949	2.857	2.782
	0.15	5	3.244	2.362	1.838	1.72	1.598	1.403	1.4	1.164
	0.2	4.454	2.468	1.688	1.301	1.141	0.964	0.899	0.811	0.738
	0.25	4.31	2.215	1.474	1.13	0.87	0.721	0.672	0.585	0.575
	0.3	4.371	1.952	1.266	0.992	0.762	0.643	0.56	0.477	0.415
	0.35	4.674	1.993	1.207	0.899	0.721	0.573	0.476	0.436	0.398
	0.4	4.537	2.061	1.25	0.87	0.667	0.504	0.426	0.398	0.322
	0.45	4.631	2.077	1.198	0.842	0.615	0.5	0.425	0.354	0.306
	0.5	4.805	2.061	1.314	0.8	0.628	0.495	0.37	0.325	0.313

附表六：n*=10 附表二及附表七相對應樣本數之比例(附表二/附表七)

A Study on the Process Capability Index C_{pk} Comparisons

Hsien-Ying Shen, Sy-Mien Chen and Yu-Sheng Hsu

Abstract

When sample size is large enough and when the central limit theorem holds, the natural estimator $\hat{C}_{pk}$ of the process capability index C_{pk} is asymptotically normally distributed. In this case, the problem about best selection can be solved by the selection rules proposed by Gupta (see Gupta (1965,1984)). However, in real world, people always face the problem caused by small samples. When the sample size is small, the exact distribution of $\hat{C}_{pk}$ becomes very complicated. On the other hand, the central limiting theorem cannot give very high accuracy. In this research, we attempt to use computer simulation to study the best selection rule when the sample is small.

Key Words: Process capability index; selection problem.

Blind Separation of Co-Channel Digital Signals with Subspace-based Iterative Least-Square Techniques

Jung-Lang Yu and Yuan-Chieh Cheng

Department of Electronic Engineering
Fu Jen Catholic University
Taipei, Taiwan 242, R. O. C.

Abstract

The eigenspace-based DWILSP is presented here, which utilizes the eigenstructure of the correlation matrix to enhance the performance of the decoupled weighted iterative least-square with projection (DWILSP) algorithm. In the DWILSP the signal estimate can be interpreted as the direct matrix inversion (DMI) beamforming problem. However, the DMI beamformer is very sensitive to the steering vector errors, which cause the signal cancellation effects. We then use the constraint projection beamformer instead of the DMI beamformer to alleviate the signal cancellation, where the output signal-to-interference-plus-noise ratio (SINR) is increased during the estimate of signal of interest. An efficient implementation of the proposed method is discussed. Computer simulations are given to demonstrate that the eigenspace-based DWILSP outperforms the DWILSP in the blind separation of co-channel digital signals.

I. INTRODUCTION

Wireless communication systems are rapidly growing in volume and range of services. The bottleneck of these systems is the limited available radio frequency spectrum. Approaches that increase spectrum efficiency have been received much attention then. One promising method is to use antenna arrays at the base station [1] [2]. Recently, the decoupled weighted iterative least-square with projection (DWILSP) [3] has been presented to blindly separate the co-channel signals by treating one signal at a time and solving a weighted least square problem. It was shown that the DWILSP algorithem can be interpreted as a direct matrix inversion (DMI) beamformer [4]. However, the DMI beamformer is very sensitive to the steering vector errors, which cause the signal cancellation effect on the signal of interest. On the other hand, it has been shown [5] that the eigenspace-based beamformer is less sensitive to the steering vector errors and converges faster than the DMI beamformer. In this letter we present the eigenspace-based DWILSP algorithm which combines the eigenspace-based beamforming techniques and the finite alphabet (FA) properties to separate the co-channel digital signals blindly. Computer simulations demonstrate that the proposed eigenspace-based DWILSP outperforms the DWILSP.

II . DWILSP ALGORITHM

Assume that d narrowband digital signals are impinging on an M-element antenna array with arbitrary geometry. The discrete-time data model of the array output is given by

$$\mathbf{x}(n) = \mathbf{A}s(n) + \mathbf{v}(n) \tag{1}$$

where A is an $M \times d$ matrix of array responses, $\mathbf{v}(n)$ is spatially and temporally white noise with covariance $\sigma^2\mathbf{I}$, and $\mathbf{s}(n) = [s_1(n)\ s_2(n)\ \cdots\ s_d(n)]^T$. It is assumed that $s_i(n)$ belongs to the finite alphabet. A block data formulation is obtained by taking N snapshots, yielding

$$\mathbf{X} = \mathbf{AS} + \mathbf{V} \tag{2}$$

where $\mathbf{X} = [\mathbf{x}(1)\ \mathbf{x}(2)\ \cdots\ \mathbf{x}(N)]$, $\mathbf{S} = [\mathbf{s}(1)\ \mathbf{s}(2)\ \cdots\ \mathbf{s}(N)]$ and $\mathbf{V} = [\mathbf{v}(1)\ \mathbf{v}(2)\ \cdots\ \mathbf{v}(N)]$. The DWILSP [3] decouples the estimation problem by treating one signal at a time. With the sample correlation matrix, the DWILSP performs the whitening technique as follows

$$\mathbf{Z} = \hat{\mathbf{R}}_x^{-\frac{1}{2}}\mathbf{X} \tag{3}$$

$$\mathbf{b}_r = \hat{\mathbf{R}}_x^{-\frac{1}{2}}\mathbf{a}_r \tag{4}$$

where $\mathbf{a}_r$ is the rth column of A and $\hat{\mathbf{R}}_x$ is the sample correlation matrix

$$\hat{\mathbf{R}}_x = \frac{1}{N}\sum_{n=1}^{N}\mathbf{x}(n)\mathbf{x}^H(n) = \frac{1}{N}\mathbf{X}\mathbf{X}^H \tag{5}$$

Then the DWILSP iteratively computes $\hat{\mathbf{b}}_r$ and $\hat{\mathbf{s}}_r$ by using the following equations

$$\hat{\mathbf{s}}_r = (\hat{\mathbf{b}}_r^H\hat{\mathbf{b}}_r)^{-1}\hat{\mathbf{b}}_r^H\mathbf{Z} \tag{6}$$

$$\hat{\mathbf{b}}_r = \mathbf{Z}\hat{\mathbf{s}}_r^H(\hat{\mathbf{s}}_r\hat{\mathbf{s}}_r^H)^{-1} \tag{7}$$

III. EIGENSPACE-BASED DWILSP

The signal estimate of DWILSP can be interpreted as beamforming problem. Substituting (3) and (4) into (6), one can find that

$$\hat{\mathbf{s}}_r = \mathbf{w}_d^H\mathbf{X} \tag{8}$$

where

$$\mathbf{w}_d = (\hat{\mathbf{a}}_r^H\hat{\mathbf{R}}_x^{-1}\hat{\mathbf{a}}_r)^{-1}\hat{\mathbf{R}}_x^{-1}\hat{\mathbf{a}}_r \tag{9}$$

The weight vector in (9) is well-known as direct matrix inversion (DMI) beamformer [4], which sets the unity gain constraint on $\hat{\mathbf{a}}_r$, i.e., $\mathbf{w}_d^H\hat{\mathbf{a}}_r = 1$,

and then minimizes the output power. However, the DMI beamformer is very sensitive to the steering vector error, which causes the signal cancellation effect on the signal of interest. The effect is especially evident when the iteration process is not yet converged. In this paper we utilize the eigenspace-based beamforming technique to alleviate the damages caused by the imperfections. The eigenspace-based beamformer generates the weight vector by

$$\mathbf{w}_s = \hat{\mathbf{U}}_s \hat{\mathbf{U}}_s^H \mathbf{w}_d \tag{10}$$

where $\hat{\mathbf{U}}_s$ is the signal subspace computed from the sample correlation matrix of (5). The eigenspace-based beamformer can be also interpreted as the constraint projection beamformer [6], which computes the weight vector by

$$\mathbf{w}_s = (\hat{\mathbf{a}}_r^H \hat{\mathbf{R}}_x^{-1} \hat{\mathbf{a}}_r)^{-1} \hat{\mathbf{R}}_x^{-1} \hat{\mathbf{a}}_{rs} \tag{11}$$

where $\hat{\mathbf{a}}_{rs}$ is given by

$$\hat{\mathbf{a}}_{rs} = \hat{\mathbf{U}}_s \hat{\mathbf{U}}_s^H \hat{\mathbf{a}}_r \tag{12}$$

It is easily shown that $\hat{\mathbf{a}}_{rs}$ has a smaller steering vector error than $\hat{\mathbf{a}}_r$ due to the projection operation in (12). In fact, it is shown in [5] that with normalizing the gain response of the signal of interest to be unity, the projection operation reduces the norm of weight vector $\mathbf{w}_d$ with the array responses to the signals unchanged. Thus, $\mathbf{w}_s$ produces a lower output noise power than $\mathbf{w}_d$ while both have the same output signal power and output interference powers. That means the constraint projection beamformer has a higher output signal-to-noise-plus-interference ratio (SINR) than the DMI beamformer. The eigenspace-based DWILSP is proposed by combining the DWILSP with the constraint projection beamforming techniques. Since $\mathbf{w}_s$ outperforms $\mathbf{w}_d$, the eigenspace-based DWILSP will converge faster and achieve a lower bit error rate on the estimate of $\mathbf{s}_r$ than the DWILSP.

IV. IMPLEMENTATION

The eigenspace-based DWILSP algorithm has two more operations than the DWILSP algorithm in each iteration. One is the computation of the beamforming weight vector $\hat{\mathbf{R}}_x^{-1}\hat{\mathbf{a}}_{rs}$ in (11) and the other is that of the vector $\hat{\mathbf{a}}_{rs}$ in (12). When the iteration number is high and/or source number is large, the computational complexity is accordingly increasing. To eliminate the operation of $\hat{\mathbf{R}}_x^{-1}\hat{\mathbf{a}}_{rs}$, one can see that the computation of $\mathbf{w}_s$ in (11) is similar to that of $\mathbf{w}_d$ in (9). Further, the computation of $\mathbf{w}_d$ is removed by using the whitening technique adopted by the DWILSP. We use the same method to eliminate the computation of $\hat{\mathbf{R}}_x^{-1}\hat{\mathbf{a}}_{rs}$ shown in the following Lemma.

Lemma 1: If $\hat{\mathbf{b}}_r$ and Z are computed by the whitening technique in (3) and (4), then $\hat{\mathbf{s}}_r = \mathbf{w}_s^H\mathbf{X}$ is identical to

$$\hat{\mathbf{s}}_r = (\hat{\mathbf{b}}_r^H\hat{\mathbf{b}}_r)^{-1}\hat{\mathbf{b}}_{rs}^H\mathbf{Z} \tag{13}$$

where

$$\hat{\mathbf{b}}_{rs} = \hat{\mathbf{U}}_s\hat{\mathbf{U}}_s^H\hat{\mathbf{b}}_r \tag{14}$$

proof : The proof of this Lemma is ignored here, but it can be performed by using the matrix inversion lemma and some simple manipulations.

Though the computation $\hat{\mathbf{R}}_x^{-1}\hat{\mathbf{a}}_{rs}$ is removed by using Lemma 1, the vector in (14) still wastes a lot of computational complexity. To combat the problem, (13) is rewritten as

$$\hat{\mathbf{s}}_r = (\hat{\mathbf{b}}_r^H\hat{\mathbf{b}}_r)^{-1}(\hat{\mathbf{U}}_s\hat{\mathbf{U}}_s^H\hat{\mathbf{b}}_r)^H\mathbf{Z} = (\hat{\mathbf{b}}_r^H\hat{\mathbf{b}}_r)^{-1}\hat{\mathbf{b}}_r^H\mathbf{Z}_s \tag{15}$$

where $\mathbf{Z}_s$ is defined as the signal subspace data matrix, $\mathbf{Z}_s = \hat{\mathbf{U}}_s\hat{\mathbf{U}}_s^H\mathbf{Z}$. It is observed that $\mathbf{Z}_s$ is irrelevant to $\hat{\mathbf{s}}_r$ and $\hat{\mathbf{b}}_r$, it could be computed in advance. Using (15) and (7), the computational complexity is reduced to nearly that of the DWILSP.

V. SIMULATION RESULTS

A five-element linear uniform array with half wavelength spacing is used for simulations. The array is illuminated by three digitally modulated QPSK signals with equally SNRs and DOAs = [5°, 16°, 35°] relative array broadside. The simulation results are plotted by averaging from 10000 independent Monte Carlo trials. A seven-training sequence was used to get an initial estimate of the array response vectors.

Fig. 1 presents the performance comparison of DWILSP and eigenspace-based DWILSP with sample number N = 100. It is shown that eigenspace-based DWILSP has a lower bit error rate (BER), especially for the user from 35°, than the DWILSP. We also show the beam patterns of these two weight vectors when they are converged. The input SNR is equal to 10dB. It is observed from Fig. 2a that the eigenspace-based DWILSP, with scaling the gain response at the signal of interest from 5° to be unity, has the ability to form deep nulls on the other two signals and keep low sidelobe levels. On the other hand, as shown in Fig. 2b, the DWILSP fails to separate the co-channel signals for some trials, which cuase high sidelobe level and can not form nulls at the other two signals. This is because using (10), the projection operation reduces the norm of weight vector $\mathbf{w}_d$ with the array responses to the signals unchanged. Thus, $\mathbf{w}_s$ produces a lower output noise power than $\mathbf{w}_d$ while both have the same output signal power and output interference powers. That means the eigenspace-based DWILSP would get higher output signal-to-noise-plus-interference ratio (SINR) and lower BER in average than the DWILSP.

In addition, the convergence properties of those two approaches when SNR =10dB are discussed. It is observed from Fig. 3 that the eigenspace-based DWILSP has better convergence speed than the DWILSP. Especially the eigenspace-based DWILSP reaches the BER below 10^{-4} using only N=40, while the DWILSP has a BER higher than 10^{-2}. The influence of the length of training sequence is also discussed in Fig. 4. The scenario is the same as that

in Fig. 2. One can find that the eigenspace-based DWILSP needs only 4-bit training sequence while the DWILSP needs 12-bit training sequence to have the BER approximately between 10^{-4} and 10^{-5}.

Finally, the effects of array sensor number on the performances of these two approaches are considered. The scenario is the same as that in Fig. 2 except input SNR=5dB. It is found from Fig. 5 that the BER of eigenspace-based DWILSP is decreased as the sensor number increases; however, the DWILSP doesn't.

VI. CONCLUSION

We have presented the eigenspace-based DWILSP algorithm, which combines the eigenspace-based beamforming techniques and the DWILSP algorithm. The DWILSP can be interpreted as a DMI beamforming problem. However, the DMI beamformer is sensitive to steering vector errors, which cause the signal cancellation on the signal of interests. To alleviate the signal cancellation effects and enhance the convergence rate, the constraint projection beamformer is used instead of the DMI beamformer. The simulation results demonstrate the eigenspace-based DWILSP can achieve much better performance than the DWILSP.

REFERENCES

[1] A. J. Paulraj and C.B. Papadias, "Space-time processing for wireless communications," IEEE Transaction on Signal Processing Magazine, pp. 49-83, Nov. 1997.

[2] Tsuhan Chen, guest editor, "Highlights of statistical signal and array processing," IEEE Transaction on Signal Processing Magazine, pp.21-64, Sept. 1998.

[3] Ranheim, " A decoupled approach to adaptive signal separation using an antenna array," IEEE Transaction on Vehicular Technology, Vol. VT-48, No.3, pp.676-682, May 1999.

[4] R.T. Compton, Jr., Adaptive Antennas: Concepts and Performance. Englewood Cliffs, NJ: Prentice Hall, 1988.

[5] L. Chang and C.C. Yeh, "Performance of DMI and eigenspace-based beamformers," IEEE Transaction on Antennas and Propagation, Vol. AP-40, no.11, pp.1336-1347, Nov. 1992.

[6] D.D. Feldman and L.J. Griffiths, "A projection approach for robust adaptive beamforming," IEEE Transaction on Signal Processing, vol. SP-42, no.4, pp.867-876, Apr. 1994.

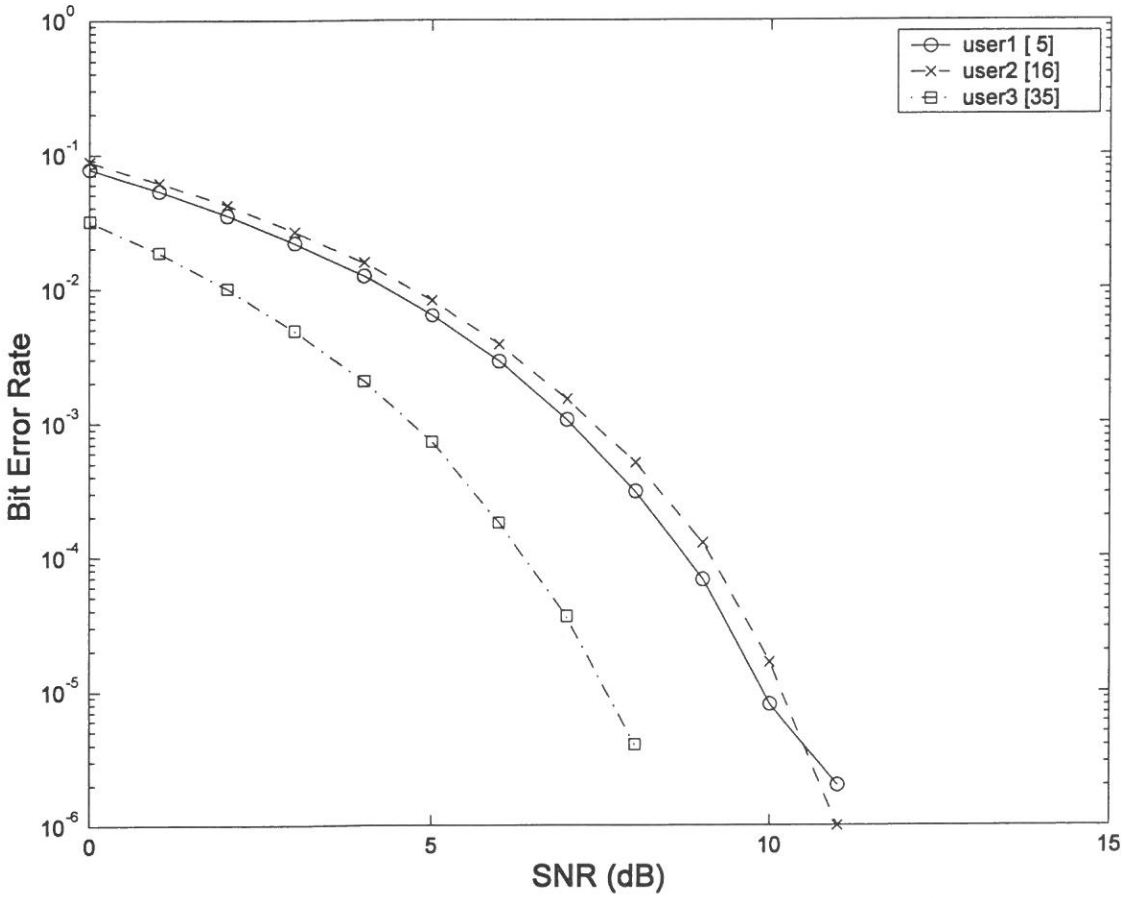

Fig. 1a Bit error rate for eigenspace-based DWILSP.

Fig. 1 Performance comparisons of eigenspace-based DWILSP and DWILSP with different input SNRs.

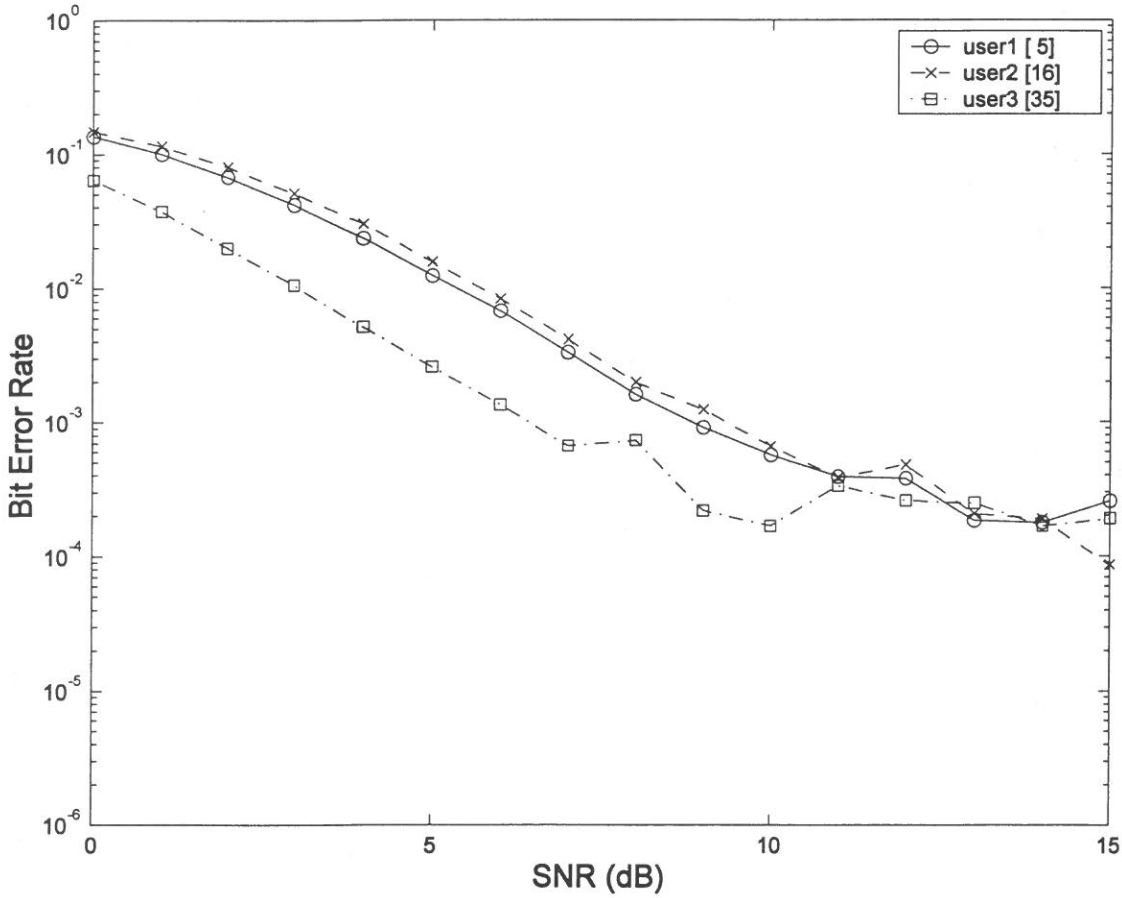

Fig. 1b Bit error rate for DWILSP.

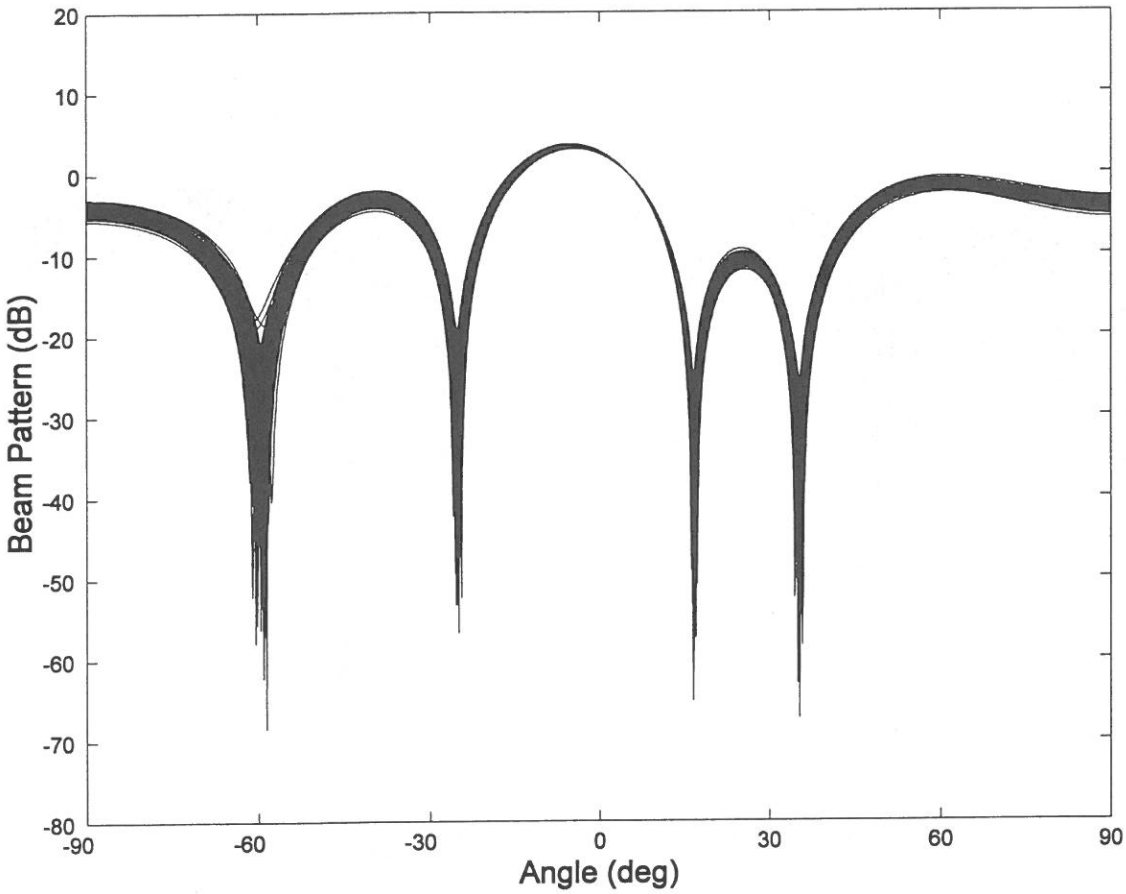

Fig. 2a Beam pattern of eigenspace-based DWILSP for the signal from 5°.

Fig. 2 Beam patterns for the weight vectors in (9) and (10) computed by eigenspace-based DWILSP and DWILSP.

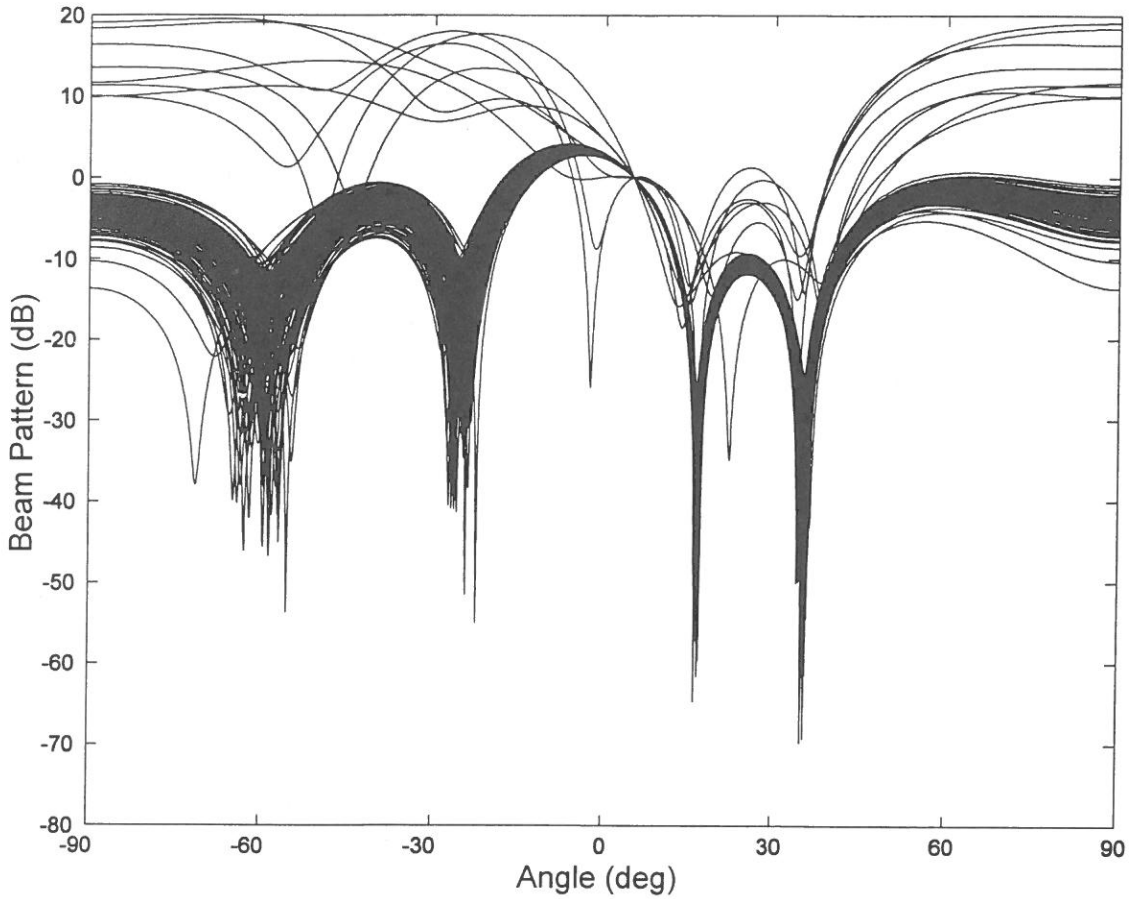

Fig. 2b Beam pattern of DWILSP for the signal from 5°.

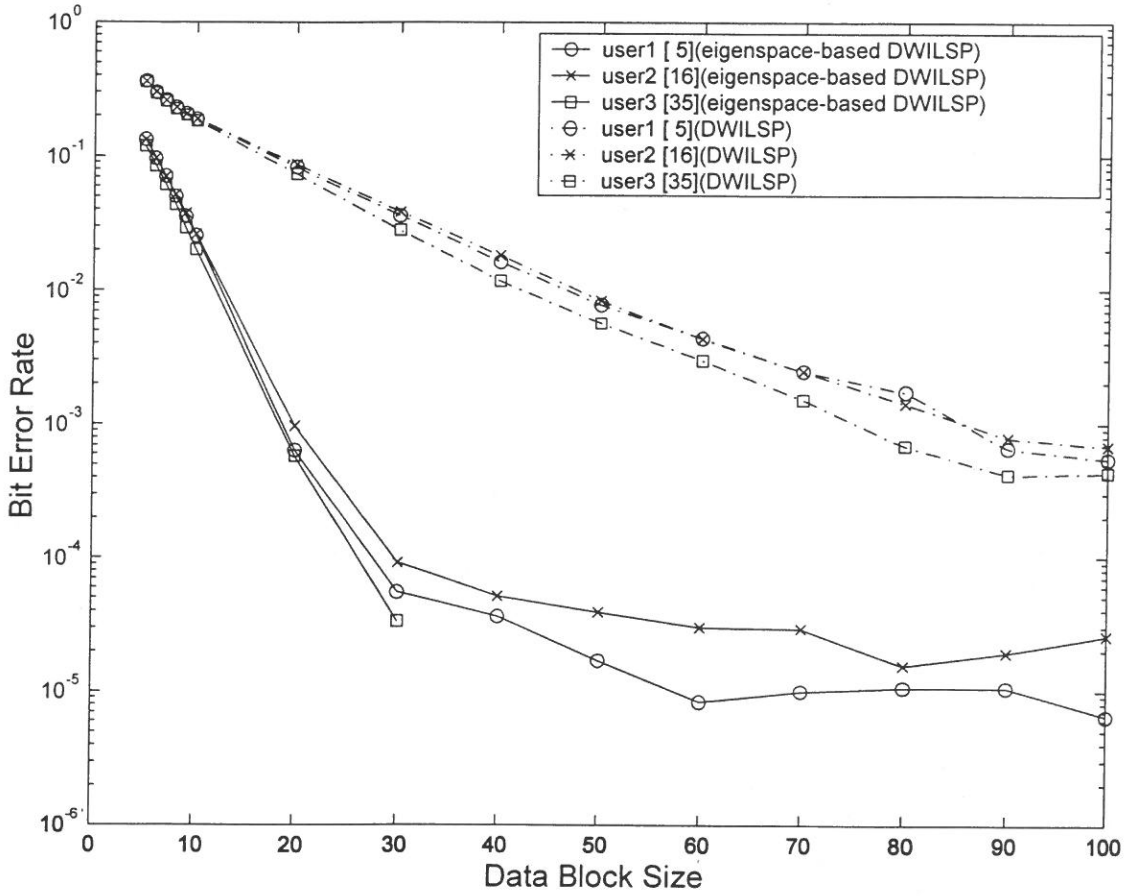

Fig. 3 Effects of sample number in the data block on the BER of DWILSP and eigenspace-based DWILSP. The input SNR =10dB.

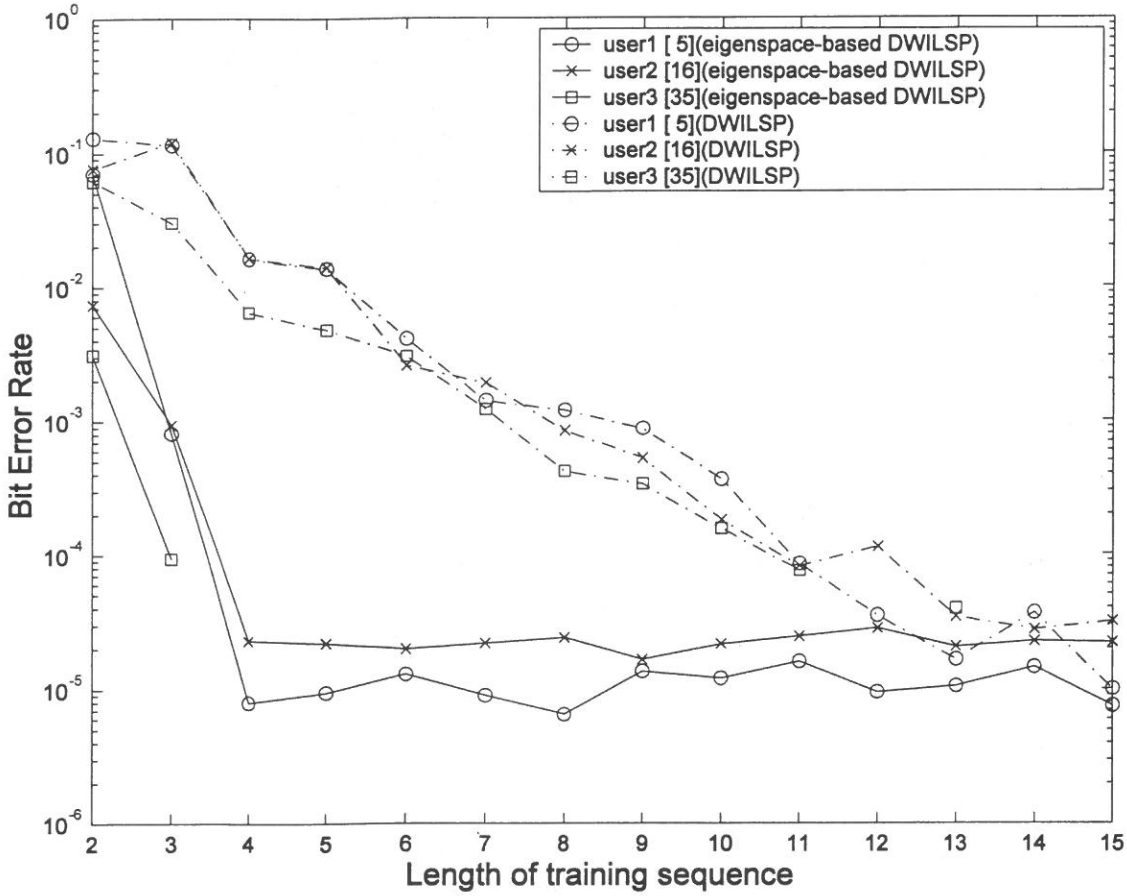

Fig. 4 Effects of training sequence length on the BER of DWILSP and eigenspace-based DWILSP. The scenario is the same as that in Fig. 2.

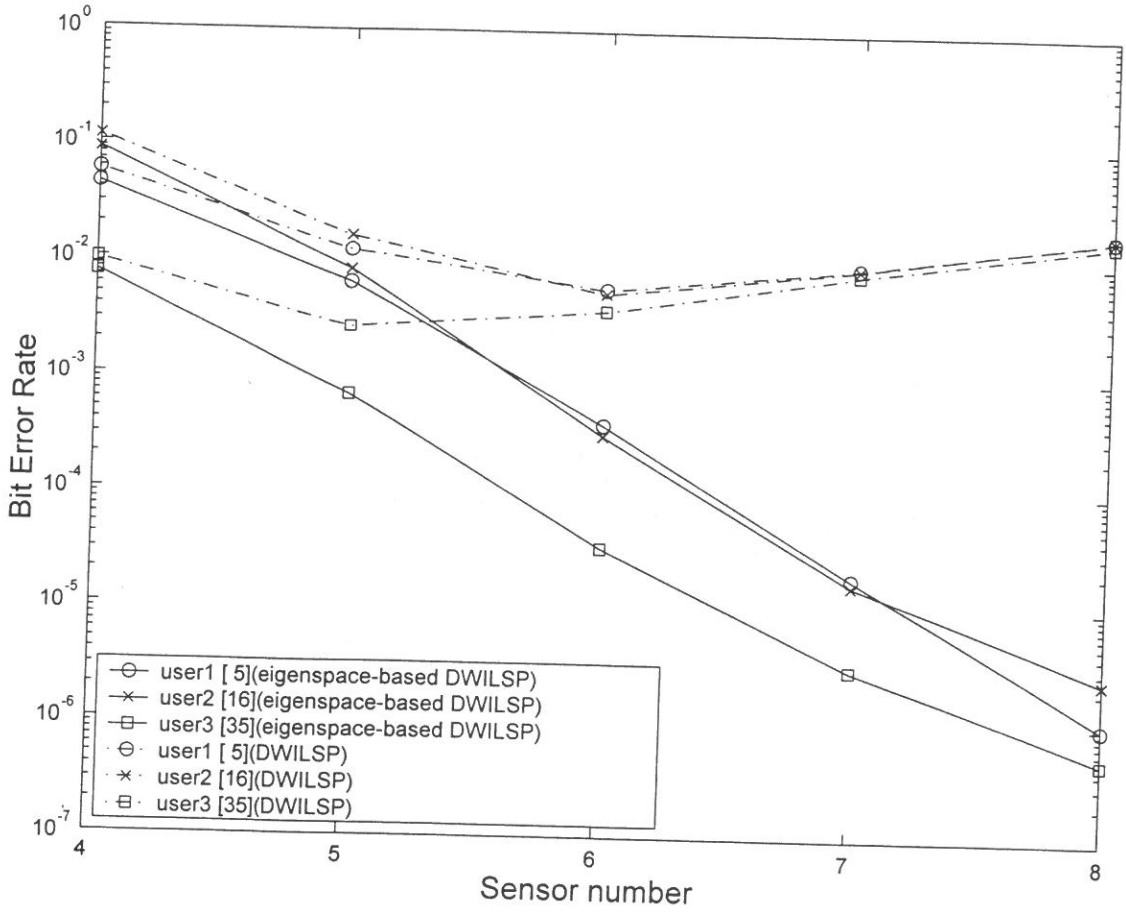

Fig. 5 Effects of array sensor number on the BER of DWILSP and eigenspace-based DWILSP. The scenario is the same as that in Fig. 2.except the input SNR = 5dB.

特徵子空間疊代最小平方技術應用在共通道數位訊號之盲目分離

余金郎　鄭元傑
輔仁大學電子工程系

摘　要

在此將提出特徵子空間 DWILSP 演算法，可利用相關矩陣的特徵架構達到提高 DWILSP 演算法的性能。在 DWILSP 演算法中，訊號估測可被解釋爲 DMI 的波束合成問題，然而，DMI 波束合成對於引導向量的誤差十分敏感，會導致訊號消除的效應，因此我們用限制投影波束合成代替 DMI 波束合成，使得估測待測訊號時的輸出 SINR 被提高，達到減輕訊號消除。我們也將探討此技術的有效實行方法。電腦模擬結果顯示特徵子空間 DWILSP 演算法在共通道(co-channel) 數位訊號的盲目分離上優於 DWILSP 。

GA-Based Evolutionary Design of PID Controller for Twin Rotor Multi-Input Multi-Output System

Wei-Yen Wang*, and Hong-Chih Huang

Department of Electronic Engineering,
Fu Jen Catholic University,
Taipei, Taiwan 242, R.O.C..
E-mail: wayne@ee.fju.edu.tw

Abstract

In this paper, a framework to automatically generate a set of parameters of PID (proportional, integral and derivative) controllers for the twin rotor multi-input multi-output system (TRMS) using a simplified genetic algorithm (GA) is proposed. The simplified GA is proposed in the paper for tuning the PID parameters. The sequential search method is used to find the desired crossover point for the crossover operation. Finally, the optimal PID parameters are applied to the TRMS. Simulation results and experiment verifications are demonstrated to show the effectiveness and performance of the proposed method.

Key Words: TRMS system, Simplified GA, PID controller.

---

*To whom all correspondence should be addressed.

This work was financially supported by the Societas Verrbi Divini.

1. Introduction

PID (proportional, integral and derivative) controllers are widely used to build the automation equipment in almost all industries [1,2], because they have very simple structures but show modest performance. A number of process and control engineers are familiar with the design and operation of PID controllers [1-4]. In high performance applications, high accurate control characteristics are of critical importance. Although the conventional control theory can realize such high performance, the optimal PID controller design strategies essentially require the complicated mathematic procedures [1,2]. Therefore, the auto-tuning of parameters of PID controllers is expected from the practical standpoints of labor saving and cost effective controller design. The application of soft computing technique to the evolutionary controller design should be one of the solutions [3-5].

Recently, genetic algorithms [6-8] have drawn significant attentions in various fields due to their capabilities in directed random search for global optimization. Thanks to a probabilistic search procedure based on the mechanics of natural selection and natural genetics, the genetic algorithms are highly effective and robust over a broad spectrum of problems [9,11-13]. This motivates the use of the genetic algorithms to overcome the problem encountered by the conventional optimization methods. Thus, a framework to automatically generate a set of parameters of PID controllers for the twin rotor multi-input multi-output system (TRMS) [10] using a simplified genetic algorithm is proposed in this paper.

This paper presents a novel evolutionary algorithm for the PID controller design, where the simplified genetic algorithm can autonomously optimize the parameters of PID controllers. The simplified genetic algorithm optimizes the three free parameters of the PID controller in the off-line manner to minimize the tracking error. Finally, the experimental results using a prototype verify the effectiveness of the optimal design.

2. PID Controller

In general, a transfer function of PID controllers has the following forms:

$$G_c(s) = \frac{u(s)}{e(s)} = k_p(1 + \frac{1}{t_i s} + t_d s) \qquad (2\text{-}1)$$

or

$$G_c(s) = \frac{u(s)}{e(s)} = k_p + \frac{k_i}{s} + k_d s \qquad (2\text{-}2)$$

where *u(s)* is the control input, *e(s)* is the error signal, which is the difference between the reference signal and the output of system, and k_p , $k_i = k_p / t_i$ and $k_d = k_p t_d$ are proportional, integral and derivative gains, respectively. The problem is to determine values of k_p , $k_i = k_p / t_i$ and $k_d = k_p t_d$, so that performance requirements are satisfied. However, for an MIMO system with complicated mathematic form, it is difficult to design an appropriate PID controller by using the conventional control theory. Therefore, the auto-tuning design of parameters of PID controllers is expected for the MIMO system. The configuration of PID controllers of the MIMO system is shown in Figure 1.

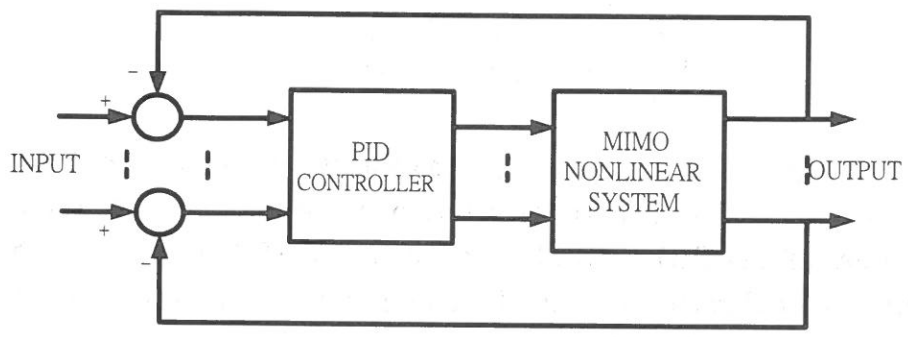

Figure 1. MIMO PID Controlled System.

3. Simplified Genetic Algorithm

Genetic algorithm (GA) was first proposed by Professor Holland in 1975. GA is a kind of mechanism of optimal searching. By using three operators: reproducing, crossover, and mutation, we can find the optimal solution of the proposed mechanism.

3.1 Fitness function

In this paper, a fitness function is defined as:

$$fitness = \frac{1}{1+E(K)} \tag{3-1}$$

where $E(K)$ denotes error between the output and the input of the closed-loop system and $K=[k_p \quad k_i \quad k_d]$ is a set of adjustable parameters of PID controllers.

3.2 Chromosomes

First, 4 chromosomes are randomly generated and the population is defined as:

$$\Psi = \begin{bmatrix} \phi^1 \\ \phi^2 \\ \phi^3 \\ \phi^4 \end{bmatrix} = \begin{bmatrix} \phi_1^1 & \phi_2^1 & \phi_3^1 & \phi_4^1 \\ \phi_1^2 & \phi_2^2 & \phi_3^2 & \phi_4^2 \\ \phi_1^3 & \phi_2^3 & \phi_3^3 & \phi_4^3 \\ \phi_1^4 & \phi_2^4 & \phi_2^4 & \phi_4^4 \end{bmatrix} \tag{3-2}$$

where $\phi^{\prime}$, $1=1,2,3,4$ are chromosomes in which $\phi_4^{\prime}$ are virtual parameters. If $\phi^{\prime}$ is an optimal solution via genetic search, then the best parameters of the PID controller are set as $K=[\phi_1^{\prime} \quad \phi_2^{\prime} \quad \phi_3^{\prime}]$. In this paper, the number of chromosomes in the population is set to be 4 for taking the crossover operation described in the next subsection.

3.3 Crossover Operation

In tradition, the position of crossover point is chosen randomly. However, in this paper, we propose a novel method to find the crossover point for the crossover process. It is called the sequential searched crossover point.

The population Ψ is divided into four parts by choosing column j and row 2 as follows:

$$\Psi = \begin{bmatrix} \phi^1 \\ \phi^2 \\ \phi^3 \\ \phi^4 \end{bmatrix} = \left[\begin{array}{cc:cc} \phi_1^1 & \phi_j^1 & \phi_{j+1}^1 & \phi_4^1 \\ \phi_1^2 & \phi_j^2 & \phi_{j+1}^2 & \phi_4^2 \\ \hdashline \phi_1^3 & \phi_j^3 & \phi_{j+1}^3 & \phi_4^3 \\ \phi_1^4 & \phi_j^4 & \phi_{j+1}^4 & \phi_4^4 \end{array}\right] = \left[\begin{array}{c|c} \Psi_{11} & \Psi_{12} \\ \hline \Psi_{21} & \Psi_{22} \end{array}\right], \phi_j^i \in R \qquad (3\text{-}3)$$

Secondly, let $j = 1$ be a crossover point and take crossover operation as:

$$\hat{\Psi} = Cr(\Psi) = \left[\begin{array}{c|c} \Psi_{11} & \hat{\Psi}_{12} \\ \hline \Psi_{21} & \hat{\Psi}_{22} \end{array}\right] = \begin{bmatrix} \hat{\phi}^1 \\ \hat{\phi}^2 \\ \hat{\phi}^3 \\ \hat{\phi}^4 \end{bmatrix} \qquad (3\text{-}4)$$

$$\hat{\Psi}_{12} = \Psi_{12} * (1-a) + \Psi_{22} * a \qquad (3\text{-}5)$$

$$\hat{\Psi}_{22} = \Psi_{12} * a + \Psi_{22} * (1-a) \qquad (3\text{-}6)$$

where $Cr(\bullet)$ is a crossover operator of a linear combination of Ψ_{12} and Ψ_{22}, a is a given constant between 0 and 1, $\hat{\Psi}$ is a new population produced by the crossover operator. From (3-3) and (3-4), two fitness values, $1/(1+E(\phi^1))$ and $1/(1+E(\hat{\phi}^1))$, can be calculated by (3-1) for ϕ^1 and $\hat{\phi}^1$, respectively. If $1/(1+E(\hat{\phi}^1)) > 1/(1+E(\phi^1))$ is satisfied, then we choose $j=1$ to be the crossover point for the crossover process. Otherwise, we re-choose $j=2$ and take the same testing of $1/(1+E(\hat{\phi}^1)) > 1/(1+E(\phi^1))$. If there is no crossover point to satisfy $1/(1+E(\hat{\phi}^1)) > 1/(1+E(\phi^1))$, the default point $j=3$ is chosen as the crossover point. Because ϕ_4^i is a virtual parameter, the crossover operation for $j=3$ does not affect the fitness values of the

population. By choosing the crossover point j and taking crossover operation, we can obtain a new population $\hat{\Psi}$ including 4 new chromosomes $\hat{\phi}^{\ell}$ for $\ell = 1,2,3,4$.

3.4 Sorting

After crossover, the population is sorted by the fitness values of chromosomes. According to $E(\hat{\phi}^1) \le E(\hat{\phi}^2) \le E(\hat{\phi}^3) \le E(\hat{\phi}^4)$, new population $[\hat{\phi}^1 \ \ \hat{\phi}^2 \ \ \hat{\phi}^3 \ \ \hat{\phi}^4]^T$ is obtained. Therefore, the first chromosome $\hat{\phi}^1$ has the highest fitness and the smallest error.

3.5 Mutation

After sorting, mutation is taken by the following formula:

$$\hat{\phi}^3 = \begin{cases} \phi^1 + \Delta(t, w_{\max} - \phi^1) & \text{if} \quad \delta > 0.5 \\ \phi^1 - \Delta(t, \phi^1 - w_{\min}) & \text{if} \quad \delta \le 0.5 \end{cases} \tag{3-8}$$

$$\Delta(t, y) = y * r * (1 - t/T)^b \tag{3-9}$$

where $\delta \in [0,1]$ denotes a random value when $\hat{\phi}^3$ is mutated, t is iteration number, T is the number of total iterations, r and b are given constants between $[0,1]$.

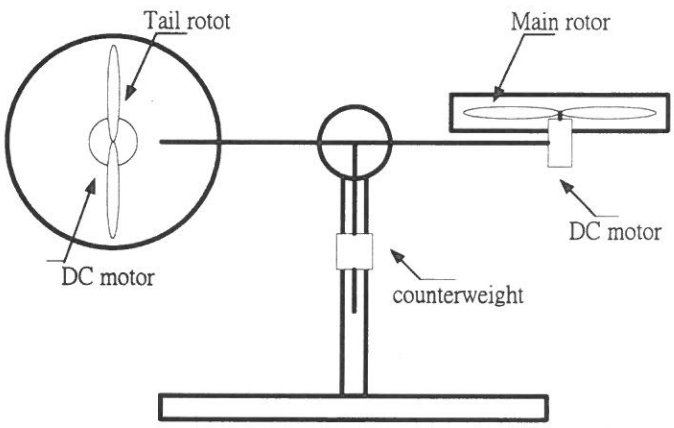

Figure 2. Indication of the twin rotor multi-input multi-output system (TRMS).

4. Coupled Model of TRMS

Figure 2 indicates the TRMS and its dynamic equations [10] can be described as follows.

A. Main Rotor Model:

$$\frac{dS_v}{dt} = \frac{l_m F_v(w_m) - \Omega_v k_v}{J_v} + \frac{g((A-B)\cos\alpha_v - C\sin\alpha_v)}{J_v} - \frac{\frac{1}{2}\Omega_h^2(A+B+C)\sin 2\alpha_v}{J_v} \quad (4\text{-}1)$$

$$\frac{d\alpha_v}{dt} = \Omega_v = S_v + \frac{J_{tr} w_t}{J_v} \quad (4\text{-}2)$$

where $A = (m_t/2 + m_{tr} + m_{ts})l_t$, $B = (m_m + m_{mr} + m_{ms})l_m$, and $C = (m_b l_b/2 + m_{cb} l_{cb})$.

B. Tail Rotor Model:

$$\frac{dS_h}{dt} = \frac{l_t F_h(\omega_t)\cos\alpha_v - \Omega_h k_h}{J_h} = \frac{l_t F_h(\omega_t)\cos\alpha_v - \Omega_h k_h}{D\sin^2\alpha_v + E\cos^2\alpha_v + F} \quad (4\text{-}3)$$

$$\frac{d\alpha_h}{dt} = \Omega_h = S_h + \frac{J_{mr}\omega_m \cos\alpha_v}{J_h} = S_h + \frac{J_{mr}\omega_m \cos\alpha_v}{D\sin^2\alpha_v + E\cos^2\alpha_v + F} \quad (4\text{-}4)$$

where $D = m_b l_b^2/3 + m_{cb} l_{cb}^2$, $E = (m_m/3 + m_{mr} + m_{ms})l_m^2 + (m_t/3 + m_{tr} + m_{ts})l_t^2$, and $F = m_{ms} r_{ms}^2 + m_{ts} r_{ts}^2/3$.

The physical variables are described as follows: S_v is angular momentum in vertical plane for the beam, S_h is angular momentum in horizontal plane for the beam, ω_m is the rotational velocity of main rotor, $F_v(\omega_m)$ denotes the dependence of the propulsive force on the angular velocity of the main rotor (should be determine experimentally), ω_t is the rotational velocity of tail rotor, $F_h(\omega_t)$ denotes the dependence of the propulsive force on the angular velocity of the tail rotor (should be determine experimentally), l_m is the length of main part of the beam, Ω_v is the angular velocity around the horizontal axis, Ω_h is the angular velocity around the vertical axis, k_v and k_h are the friction coefficients, g is the gravitational acceleration, m_{mr} is the

mass of the main DC-motor with main rotor, m_m is the mass of main part of the beam, m_{tr} is the mass of the tail motor with tail rotor, m_t is the mass of the tail part of the beam, m_{cb} is the mass of the counter-weight, m_b is the mass of the counter-weight beam, m_{ms} is the mass of the main shield, m_{ts} is the mass of the tail shield, l_m is the length of main part of the beam, l_t is the length of tail part of the beam, l_b is the length of the counter-weight beam, l_{cb} is the distance between the counter-weight and the joint, α_v is the pitch angle of the beam, α_h is the pitch angle of the beam, J_v is the sum of moments of inertia relative to the horizontal axis, J_h is the sum of moments of inertia relative to the vertical axis, J_{tr} is moment of inertia in DC-motor tail propeller subsystem, J_{mr} moment of inertia in DC-motor main propeller subsystem, r_{ms} is radius of main shield, and r_{ts} is radius of tail shield. The vertical motion of the beam (around the horizontal axis) can be described as a rotational motion of a solid mass $M_v = dS_v / dt$. The horizontal motion of the beam (around the vertical axis) can be described as a rotational motion of a solid mass $M_h = dS_h / dt$. It should be noted that angular velocities are non-linear functions of the input voltage of the DC-motor. Thus, we have two additional equations.

C. The Nonlinear Equation of Main Motor:

$$\frac{du_{vv}}{dt} = \frac{1}{T_{mr}}(-u_{vv} + u_v), \omega_m = P_v(u_{vv}), \tag{4-5}$$

D. The Nonlinear Equation of Tail Motor:

$$\frac{du_{hh}}{dt} = \frac{1}{T_{tr}}(-u_{hh} + u_h), \omega_t = P_h(u_{hh}), \tag{4-6}$$

where u_h and u_v are the inputs of the DC motors, P_v and P_h are nonlinear functions, T_{mr} is time constant of main-motor propeller system, and T_{tr} is time constant of tail motor-propeller system. The above model of the motor-propeller dynamics is obtained by substituting the nonlinear system by a serial connection of a linear dynamic system and static non-linearity as shown in Figure 3.

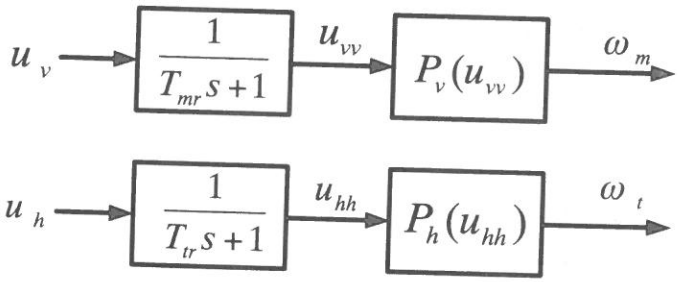

Figure 3. The nonlinear functions of the DC-motors.

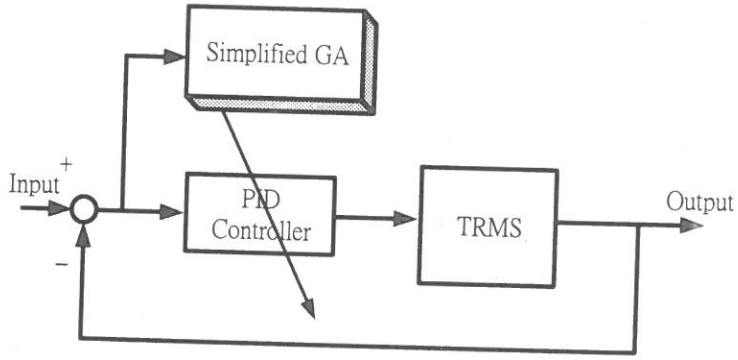

Figure 4. The PID controlled system using genetic search.

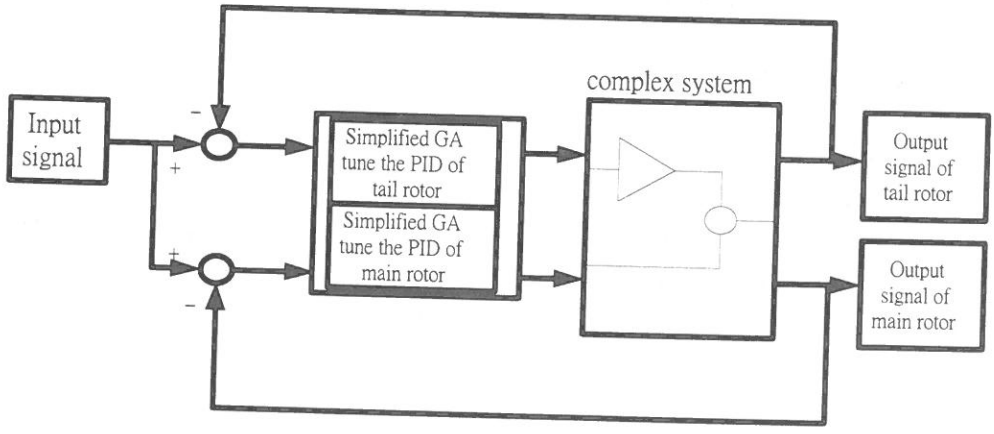

Figure 5. Configuration of the learning mechanism.

5. Simulation Results and Experimental Verifications

5.1 Simulation Results

The simplified GA is used to tune the parameters, i.e., $K = [k_p \quad k_i \quad k_d]$, of PID controllers. Figure 4 shows the structure of the closed-loop system.

Due to airstreams, in general, the controllers of the TRMS system are difficult to design. The closed-loop system controlled by PID controllers using GA-based evolutionary design is shown Figure 5. Two respective simplified GA are applied to search the parameters of PID controllers for the main rotor and the tail rotor.

By using the simplified GA for off-line tuning the parameters of PID controllers, the tracking output of main rotor of the coupled system is shown in Figure 6. The tracking output of tail rotor of the coupled system is shown in Figure 7. Therefore, we can find the optimal PID parameters as $k_{pv}^* = 0.1889$, $k_{iv}^* = 0.4732$, and $k_{dv}^* = 0.8801$, which are shown in Figure 8 for the coupled main rotor system. For the coupled tail rotor system, the optimal parameters of the PID controller are $k_{ph}^* = 5.9457$, $k_{ih}^* = 0.088$, $k_{dh}^* = 7.7734$, which are shown in Figure 9. To demonstrate the effectiveness of the optimal parameters, they are applied in experiments of the prototype TRMS.

5.2 Experimental Verifications

To make experiments, the prototype of TRMS is shown in Figure 10. The optimal parameters of PID controllers obtained from simulations are used to control the TRMS. Figures 11 and 12 indicate that the output trajectories of the main rotor and the tail rotor can follow the reference signals like the simulation results shown in Figures 6 and 7.

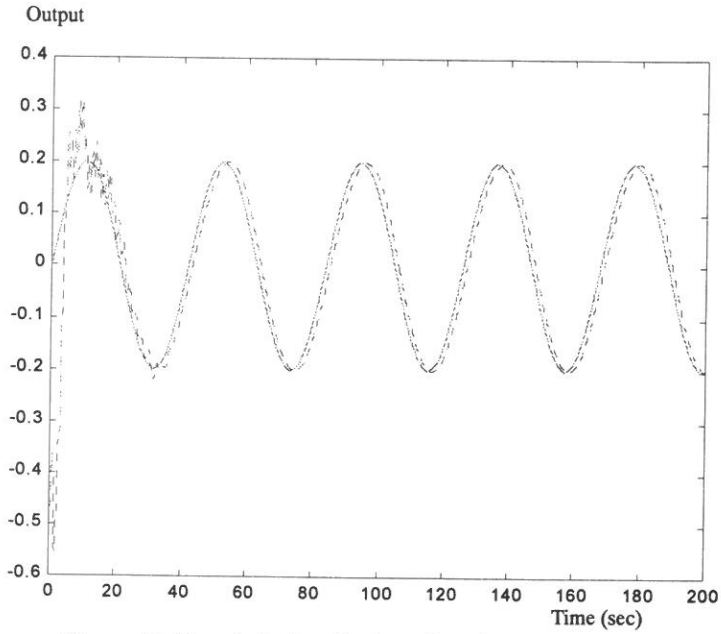

Figure 6. Coupled simulation of main rotor (dot line is tracking signal and solid line is *sin* signal).

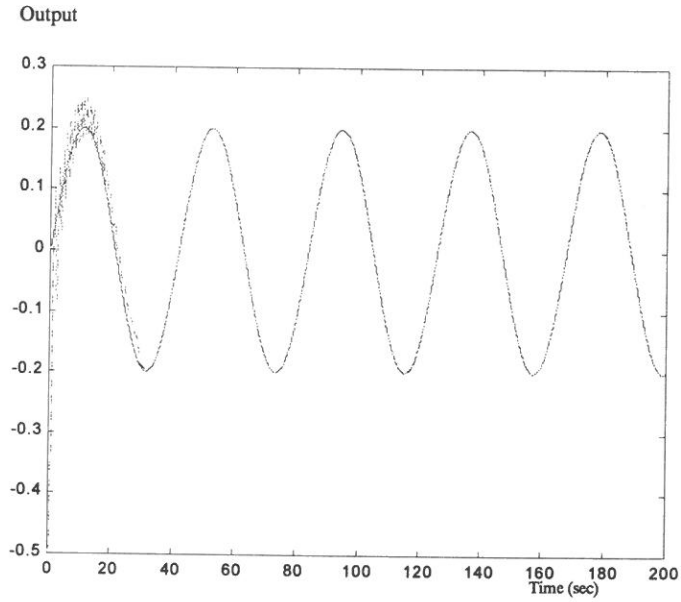

Figure 7. Coupled simulation of tail rotor (dot line is tracking signal and solid line is *sin* signal)

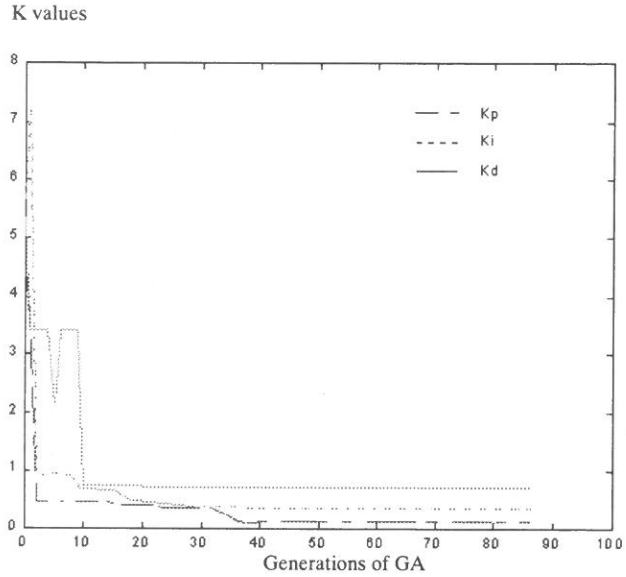

Figure 8. The PID parameters for the main rotor.

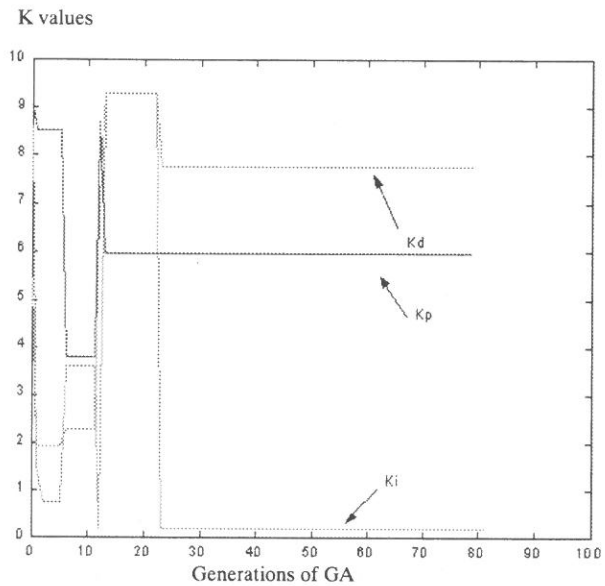

Figure 9. The PID parameters for the tail rotor.

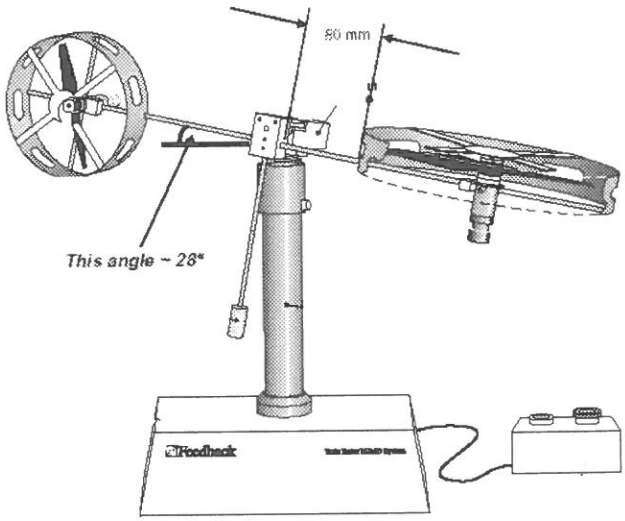

Figure 10. The prototype of MIMO TRMS.

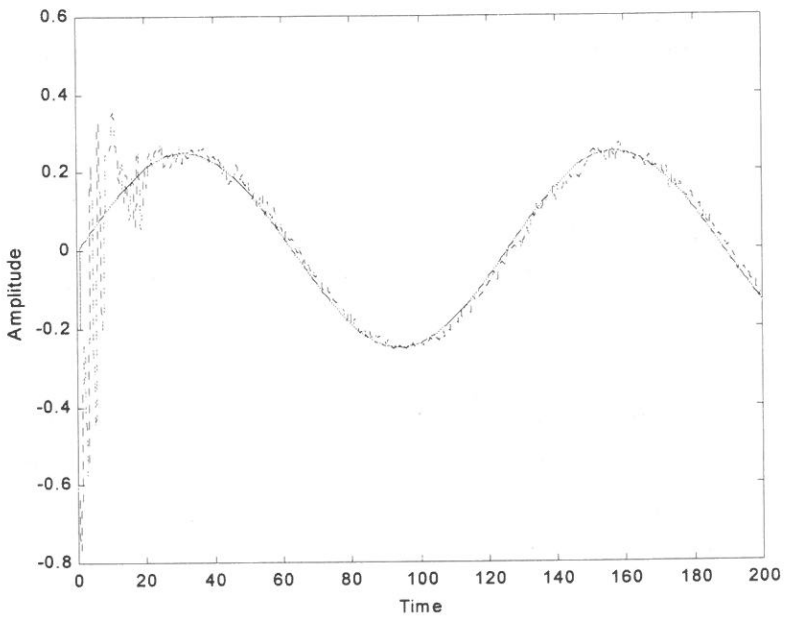

Figure11. The experiment result of coupled main rotor using optimal PID controller.

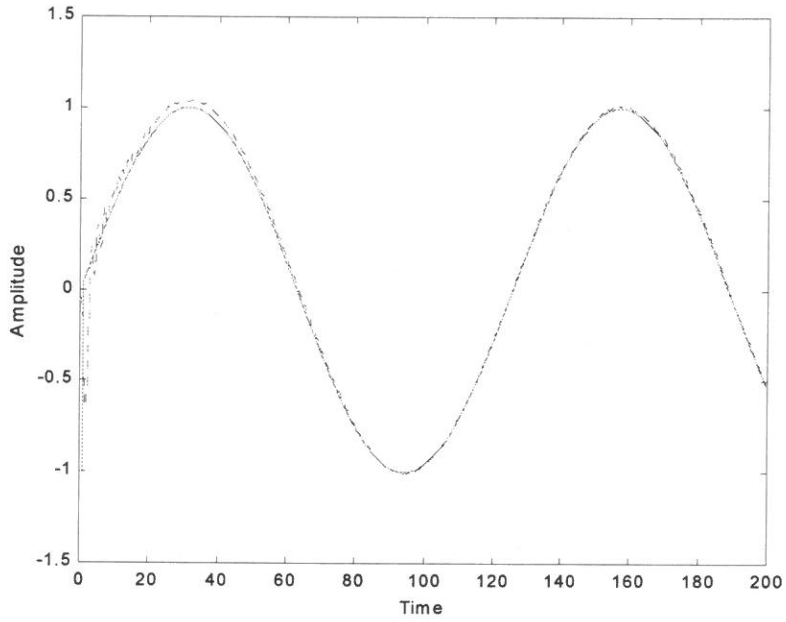

Figure12. The experiment result of coupled tail rotor using optimal PID controller.

6. Conclusions

In this paper, a novel evolutionary PID controller design for TRMS using a simplified genetic algorithm is presented. The design algorithm requires no complicated procedure, which is used in the conventional design theory. Moreover, the computation procedure of the proposed method is much simpler than that of the non-genetic optimization algorithms. Simulation results for off-line tuning the parameters of PID controllers have been illustrated to show the effectiveness of the GA-based design. Experiment results using the prototype of TRMS also verify the effectiveness of the proposed optimal PID controller design.

7. References

(1) Cs. B and L. Keviczky, "A High precision PID Controller for Inverse Unstable Plant," *IEEE Instrumentation and Measurement Technology Conference*, pp. 1183-1188, 2001.

(2) Ming Tzu Ho, "Non-Fragile PID Controller Design," *IEEE Conference on Decision and Control Sydney*, pp. 4903-4908, December, 2000.

(3) K. C. Jeong *et al.*, "A Fuzzy Logic-Based Gain Tuner for PID Controllers," *IEEE International Conference on Fuzzy System*, pp. 551-554, 1998.

(4) R. W. Swiniarsski, "Novel Neural Network Based Self-Tuning PID Controller Which Uses Pattern Recognition Technique," *Process of the American Control Conference*, pp. 3022-3024, 1990.

(5) A. E. B. Ruano, P. J. Fleming and D. I. Jones, "Connectionist approach to PID auto tuning," *IEE proceedings-D*, vol. 139, pp. 279-285, 1992.

(6) Z. Michalewicz, *Genetic Algorithms + Data Structure = Evolution Program*, Springer-Verlag, 1996.

(7) D. Goldberg, *Genetic Algorithms in Search, Optimisation, and Machine Learning*, Addison-Wesley, 1989.

(8) D. Lawrence, *Handbook of Genetic Algorithms*, Van Nostrand Reinhold, 1991.

(9) K. Kristinsson and G. Dumont, "System identification and control using genetic algorithms," *IEEE Transaction SMC,* Vol. 22, pp. 1033-1046, 1992.

(10) *Feedback Matlab Based Control Products Manual.* Feedback Instruments Ltd., 1997.

(11) B. Porter and A. Jones, "Genetic tuning of digital PID controllers," *Electronic Letters*, Vol. 28, pp. 843-844, 1992.

(12) C. Hsu, K. Tse and C. Wang, "Digital Redesign of Continuous Systems with Improved Suitability Using Genetic Algorithms," *Electronics Letters*, Vol. 33, no. 15, pp. 1345-1347, 1997.

(13) R. Caponetto, L. Fortuna, S. Graziani, and M. Xibilia, "Genetic algorithms and applications in system engineering: a survey," *Trans. Inst. Meas. Control,* Vol. 15, pp. 143-156, 1993.

多輸入多輸出雙螺旋系統 PID 控制器之基因演化設計

王 偉 彥　　黃 宏 智
輔仁大學 電子工程學系

中 文 摘 要

本文提出對非線性多輸入多輸出雙螺旋系統使用簡化式基因演算法則調整其 PID 控制器參數，產生對系統較佳之控制器，以實現輸出訊號可以追蹤期望的輸入訊號。本文中所提出的方法將突破傳統調整 PID 參數的方式，使用簡化式基因演算法，藉由實數循序搜尋參數交配法，快速地找出所要之參數，對系統產生較好之控制器，直接對系統進行模擬追蹤。最後，以雙螺旋系統原型機之控制實驗來驗證本文所提方法之可行性及效果。

關鍵詞： 多輸入多輸出雙螺旋系統，簡化式基因演算法則，PID 控制器。

壓力及人格特質與猝睡症之關聯

陳 秀 蓉
輔仁大學心理系
錢 仁 琳
輔仁大學心理系
李 宇 宙
台灣大學附設醫院精神部
陳 美 琴
輔仁大學心理復健系

摘 要

本研究目的在探討壓力及人格特質與猝睡症之關聯。而目前台灣較少有研究從社會心理取向瞭解猝睡症患者。本研究即進行二項假設考驗：1.猝睡症患者之特定人格傾向與對照組間有顯著差異。2. 研究假設猝睡症患者會較一般人感受到更多的主觀壓力，但因個人平日表現如一般常人，所以來自情境的社會資源與支持應與一般組無差異。經採立意取樣選入猝睡症患者16位爲病人組，並配對一般正常個案16位爲對照組。研究結果顯示：猝睡症患者的人格特質在外向性面向中之「活動力」與謹慎性面向中之「自我訓練」兩項分數，與對照組比較有顯著差異。而猝睡症者比對照組感受到更多的主觀壓力，特別在是否能自我控制的題項上出現比對照組更高的壓力，在社會支持度上其環境資源則與一般人無異。建議未來在健康維護與治療上，除藥物幫助外，可以針對特定性格因素如活動性過低，自我訓練差，以及特定壓力知覺如不可控制性協助個案因應因爲疾病所帶來的適應問題。

關鍵詞：猝睡症、人格特質、壓力知覺、社會支持、活動性、自我訓練

簡　介

睡眠障礙是臨床工作上常聽到的抱怨，各種生理疾病或心理因素都有可能引起不同的睡眠問題，失眠(insomnia)是最常聽見的一種，一般精神醫學或心理學多將研究重點擺在失眠的症狀上，卻忽略其他睡眠障礙如多眠(hypersomnia)與猝睡症(narcolepsy)背後的臨床問題以及其可能的病理因素。國外的流行病學調查發現，日間多眠的終身盛行率約在百分之五左右，猝睡症、睡眠週期干擾、睡眠呼吸中止症均會引發嗜睡、疲倦等現象。尤以工作中發生猝睡現象更嚴重，容易導致交通誤失、工業災難等問題，影響不可說不大(Benbadis et al.,1999)。又猝睡症好發於青春期，青少年發病後往往被貼與懶惰、無意志力等負面標籤，卻未能接受妥善醫療照顧，影響他們的身心健康發展。

目前，國內缺乏對猝睡症患者心理社會現象的瞭解，雖然國外的研究並未發現猝睡症患者的人格特質與一般人有明顯差異，但患者通常因爲嗜睡的症狀在工作學業家庭上感受到較大的壓力,進而可能也會反映出特定的性格特徵。本研究的目的主要想了解台灣猝睡症患者個人的特質是否與一般人有差異，另外對於患者本身在社會、心理方面遭受的衝擊進行初步的探究，進而喚起社會重視這樣的症狀與對疾病整體包括藥物與社會心理層面的照護。

猝睡症的臨床特徵是：至少三個月期間反覆在日間發生異常REM（rapid eyes movement，快速動眼）睡眠, 並在REM睡眠期間可能會經驗到突發性肌肉失張症--猝倒(cataplexy)、將睡與將醒幻覺(hypnagogic or hypnopompic hallucinations) 及睡眠麻痺(sleep paralyze)等症狀（註一）；並於片刻醒來時會有疲勞消除之清爽感(refreshing)，且需排除因癲癇或心因性困擾的因素所致（Kaplan, Sadock & Grebb, 1994）。在日間REM睡眠每次發作期間個案會報告有作夢經驗，且每次持續時間約爲10至20分鐘，若未治療平均每日有2-6次睡眠發作。流行病學研究顯示，在成人中猝睡症的盛行率爲0.02%-0.16%，男女比率相同，而遺傳與生物性因素在猝睡症的發生佔重要的角色 (DSM-IV, 1994; Kaplan, Sadock & Grebb, 1994；蘇, 民89)。

要瞭解猝睡症的病理現象，首先得瞭解人類的睡眠生理學。一般正常成年人的腦波是規律有節奏的，在清醒、安靜、閉眼的狀態下，會呈現主要爲10Hz的α波，而成人睡眠節奏白天和晚上分得很清楚。一般在睡眠期之深度與腦波變化有關係，通常分爲四期，第一期腦波呈現4-6Hz的低幅θ波，間歇會出現高振幅銳波；第二期多出現14Hz的紡錘波以及K複合波；第三期會出現高振幅慢波δ波，比例約佔此時腦波的20-50%，中間會參雜一些紡錘波；第四期會出現不規則的連續大慢波，約佔這時腦波的50%。而在睡眠期間會交替出現快速動眼期(簡稱REM睡眠)與非快速動眼期兩階段（簡稱NREM

睡眠）。一般睡眠先從淺層的NREM睡眠開始，逐步進入深層的第三與第四期之NREM睡眠，約90分鐘左右，接著在NREM睡眠期第三或第四期後會進入快速動眼期REM睡眠，是爲一個睡眠週期，一般夜晚睡眠共有4至6個重複週期 (廖等，民89；蔡, 民89)。

猝睡症的病理學探討顯示，排除下列因素造成病態性嗜睡，包括睡眠不夠充足、老化、睡眠呼吸中止症、時差等等，猝睡症者則是在不可控因下，無法保持一個穩定的睡醒節律。在夜間睡眠時，正常者會由清醒進入睡眠週期循環（由NREM進入REM，再進入NREM至REM循環），有時正常者在REM後會出現非常短暫清醒，然而猝睡患者的睡眠型態在REM後會出現更多次數之短暫清醒狀態，使得夜間睡眠斷斷續續；而其白天猝睡發作時，個人腦部會病態地從清醒期直接轉換到REM睡眠，這樣不穩定的腦部狀態解釋了猝睡症的主要症狀(Saucerman, 1997)。正常REM睡眠的特徵是腦部主動的激起狀態，通常伴隨栩栩如生的認知，以及聽覺或視覺影像，同時肌肉非常放鬆，這樣可以保護睡著的人不至於隨夢境做出動作。然而，猝睡個案白天REM睡眠侵入清醒狀態時，會因進入REM時期，以致於發生猝倒、睡眠麻痺、將睡幻覺(出現栩栩如生的視覺影像以及聽覺)等現象。發作可以是在患者吃東西、開車、講話的當中，不像睡眠呼吸中止的患者，猝睡症患者從小睡中醒來可以感到精神恢復了，睡眠發作前通常沒有徵兆(李, 民89)。

有些研究主張猝睡症REM睡眠的不規則主因與腦幹功能的損壞有關；也有些人認爲猝睡症是90分鐘生物基本節律(rest-activity cycle)的極端表現，正常人在清醒時可以壓制REM的部分，但是猝睡症患者不行, 在成人與狗的身上都發現猝睡現象的REM抑制機轉問題。另外還有學者認爲猝睡症跟基因異常有關(Mignot,1998)，發現九成以上猝睡症患者在人體白血球抗原(human leukocyte antigen, 簡稱HLA)有HLA-DR2及DQw1類型比例，比未出現猝睡症病史個案之10%-34%要高(Kaplan, Sadock & Grebb, 1994)。上述例證都說明猝睡個案有生理因素導致，可能伴隨有神經損傷的症狀完整病兆，特別是腦幹區域。

猝睡症通常在青少年以及成人早期逐漸顯現出嗜睡的症狀，而猝倒、睡眠麻痺、將睡幻覺等正性症狀通常是在睡眠第一次發作後數年才發生，只有14%的患者會經歷到所有四種症狀。但是因爲上述的症狀，猝睡問題會對患者的社會及職業功能有重大的影響(Roy, 1976)。又根據美國的研究，對於兒童或是青少年時期的猝睡症患者來說，通常會報告這樣的疾病(症狀)讓他們感到尷尬、學業成績低落、感覺喪失自我價值，而其人格傾向畏避可能引起他人注意的情境，對他們的誤診也常常造成不適當的治療，而且會低估個人的潛力(Broughton & Broughton, 1994)。而成人患者的問題則圍繞在可能喪失工作、安全問題、婚姻障礙、還有精神疾病方面(Broughton & Mullington, 1994)。

在猝睡症人格特徵的探討上，Beutler等人(1981)比較20位猝睡症者與20位呼吸中止患者在性格上有明顯區別，而猝睡患者在焦慮與社會內向傾向上偏高；另外一個研究則發現與睡眠呼吸中止的患者比起來，猝睡症患者在艾森克人格問卷（Eysenck Personality Questionnaire，簡稱EPQ）上出現較高的身體焦慮(somatic anxiety)分數，以及較低的社會化（socialization）分數(Sachs & Levander, 1981)；但是Krishnan等人（1984）的研究與正常個案比較卻發現猝睡症在外向性方面的分數卻是偏高的，研究者指出這可能是因爲猝睡症患者服用保持白日清醒的興奮劑所導致的結果。在性格傾向上到底本國個案是否也有特殊的性格問題，值得進一步瞭解。

在以上的文獻研究中可以發現，猝睡症患者因爲自身的症狀，在人格方面似乎比較畏避社會合作的環境，在身體焦慮方面則比較高，而這樣的疾病會帶來的壓力，除了患者對自己可能自信不夠，也要擔心外在的工作、婚姻、家庭是否不保，猝睡症的症狀確實帶給患者日常生活方面的種種不便，因此患者是否會主觀知覺到更多的壓力，也是作者關心的焦點之一。本研究的假設性目的有二：1. 研究者欲驗證猝睡症雖然爲一生理性疾病，但是該患者長期嗜睡問題其人格特質是否與一般人不同，亦即研究假設與一般沒有猝睡症的人比較，兩者性格傾向應有顯著差異。2. 根據文獻假設猝睡症患者會較一般人感受到更多的主觀壓力，但因個人平日表現如一般常人，所以來自情境的社會資源與支持應與一般組無差異。以上探討期能回應猝睡症患者之社會心理特徵。

研究方法

本研究受試者採取立意取樣（purpose sampling），抽取經某教學醫院精神部醫師根據精神疾病診斷與統計手冊第四版符合猝睡症的診斷準則(DSM-IV, 1994)（註二）者，並在接受過多次入眠潛期試驗(Multiple Sleep Latency Test)檢測以及抽血檢查後之個案組成病人組，並配對組成正常對照組。

研究工具方面依據研究目的，想瞭解猝睡症個案性格特性，現今性格量表以NEO PI-R人格問卷在研究、應用上與心理健康、每天應付壓力的因應反應有相關（Costa & McCrare, 1992），符合本研究探討議題，因此選採用NEO PI-R人格問卷，作爲個案現階段性格特徵之測量。艾普渥斯嗜睡度量（Epworth Sleepiness Scale，簡稱ESS)則測量個人嗜睡程度，以瞭解猝睡症的嚴重度。而社會資源量表測量個案生活中的社會支持與資源取得，加上主觀壓力知覺量表之測量共有量表四種。以下分別說明工具性質與其信、效度資料。

「NEO PI-R人格問卷」爲Paul T. Costa & Robert R. McCrae編制，由輔仁大學陳美琴老師將其翻譯爲中文，並且建立台灣地區的信、效度資料(Chen & Piedmont, 1999)。量表爲五點式李克特量表(Likert scale)。題目涵蓋了人格的五個面向(domains)包括：神經質(neuroticism, 簡稱N)測量個案適應性或情緒的穩定性程度；外向性(extraversion, 簡稱E) 測量個案人際方面偏向社交、果斷、主動、有精力、樂觀的、喜好刺激的程度；開放性(openness, 簡稱O)測量個案對情境開放性與好奇性的程度，以及是否有創新的點子與非傳統的價值；同意度(agreeableness, 簡稱A)是測量個人利他表現與同情他人的傾向程度。謹慎性(conscientiousness, 簡稱C)測量一個人有效主動計畫、組織、並完成任務的特徵傾向。五個面向中每一獨立面向又各有六個分量表(facets)，六個分量表的總分即爲該人格面向的得分。此問卷的記分方式是依符合程度大小分別給予0-4的記分，即個案覺得該敘述明顯錯誤描述自己或十分不同意該句就記爲0分，如果該敘述多半是錯誤就記爲1分，該敘述一半正確一半錯誤，無法決定或介於於中立記爲2分，如果該敘述多半正確或同意記爲3分，如果該敘述明顯正確或十分同意記爲4分。此次研究根據文獻採用其中三個面向與猝睡症有關之性格特質：即神經質、外向性、與謹慎性，單一分量表中有六個題項，因此單一分量表得分範圍應該在0至24分之間。而每個人格面向的得分應該介於0至144分之間。

「艾普渥斯嗜睡度量表」(Epworth Sleeping Scale, 以下簡稱ESS)是臨床上用來評估嗜睡程度最常用的主觀報告量表(John, 1992)，本研究亦考驗其內部一致性Cronbach α 係數爲0.8498，顯示本量表內部題項同質性一致程度頗高。本量表內容總共有八題，請受測者自評在八種不同的日常生活情境中的嗜睡程度。每一情境請個案評估，從不曾打瞌睡記分爲0，偶爾會打瞌睡（大都能維持清醒）記分爲1，很可能打瞌睡（半數機會打瞌睡）記分爲2，經常要打瞌睡（很少能維持清醒）記分爲3，然後計算自己的嗜睡分數有多高。

「社會資源量表」爲呂碧鴻等（民84）參考Cohen & Wills(1985)以及Franks、Campbell & Shield(1992)之測量方法所編修，內容共有18題，爲四點式Likert量表，主要是測量受試者在生活中社會支持資源的狀況，內容包含(1)情感上支持:包括第1、3、10、11、12、13、14、15、18題與(2)實質上支持:包括第2、4、5、6、7、8、9、16、17題。該量表爲Likert四點量表，受試者自評符合程度，1代表非常不符合，2代表有點不符合，3代表符合，4代表非常符合，經轉換分數最後分析資料之得分越高表示受試者所經驗到的實質支持與情感支持度就越高。本量表由呂碧鴻（民84）以219名台大醫院家醫科門診患者爲研究對象，得到全量表內部一致係數爲.90，因素分析共得兩個因素：「情感資源因素」與「實質資源因素」，其內部一致性係數分別爲.84與.82，顯示此量表具有良

好的信度。

「壓力知覺量表」爲呂碧鴻等(民84)依據Cohen等人(1983)主觀知覺壓力的概念編修而成，主要是想了解受試者最近一個月自我知覺壓力的強度。共有六題，採用四點式Likert量表，其中1代表從不如此， 2代表偶爾如此， 3代表經常如此，4代表總是如此，得分越高表示受試者知覺壓力強度越強。呂碧鴻（民84）以219名台大醫院家醫科門診患者爲研究對象，得到全量表內部一致係數爲.81，顯示此量表具有良好的信度。

施測步驟首先在醫院精神部醫師協助下，收集到經診斷爲猝睡症、並且目前處於停藥階段的患者。患者皆做過多次入睡腦波檢查(MSLT)，並且抽血確認人類白血球抗原(HLA)類型。多次入睡腦波檢查過程如下：受試者須先在睡眠實驗室接上電極線，測量夜間睡眠腦波八小時，接著第二天白天自起床後，每隔兩小時再作一次20分鐘的入睡試驗，一共進行五次。若五次白天入睡試驗中，至少有三次皆在五分鐘內入睡及出現REM，則可能爲猝睡症患者，請患者回診再經抽血檢驗與醫師臨床問診之後，確認爲猝睡症患者。另外徵求無睡眠障礙且無精神疾病史的一般人16名。請兩組受試者分別完成四份問卷後進行資料分析。

結 果

根據本研究假設，將針對假設一與假設二採用統計套裝軟體SPSS進行組間差異檢定比較，各項結果分述如下：

本研究依DSM-IV診斷準則與測量資料選入猝睡症患者16人，其中男性11人、女性5人，平均年齡23.41歲(標準差6.61)；並配對抽取對照組即一般沒有特殊睡眠障礙的受試者16人，其中男性9人、女性7人，平均年齡24.02歲(標準差7.76) ，而兩組在性別(Chi-square=.533, df=1, p<.465)與年齡(t=..236, df=30, p<.815)上均無統計顯著差異，兩組共計32人。

其中猝睡症患者16人接受抽血檢查以及多次入眠潛期試驗診斷，各病患皆經由醫師針對多型睡眠電腦圖判斷排除其他異常之睡眠，且檢視16位患者第二天白天五次MSLT試驗，他們都至少有三次在五分鐘內即入睡（入睡潛伏期平均3分鐘，SD=2.18）及在五分鍾內出現REM睡眠發作情況（REM發作期平均在睡後4.5分發生，SD=2.37），依據上述資料確認後選入個案。

此外，本研究進一步檢測，猝睡患者之嗜睡度與睡眠時間是否顯著不同於正常對照組個案，以確認選組個案之適合性。發現兩組個案在夜間睡眠的平均時間有統計顯著差異, t=-3.320, df=30, p<.002 (兩組的平均夜間睡眠時數請參見表一)；且猝睡症組夜

間睡眠時間較長。關於平日嗜睡程度，本研究利用艾普渥斯嗜睡量表，發現兩組間嗜睡程度也有顯著差異，t=-6.057, df=29, p<.000 (兩組的平均嗜睡程度請參見表二)；且猝睡個案嗜睡傾向顯著高於對照組，而以猝睡症嗜睡程度平均達14.60分來看，此分數在ESS量表診斷分數上也已顯著達到臨床意義。在確認兩組個案特性後，以下就假設進行差異考驗。

表一・兩組平均夜間睡眠時數

睡眠時間	組 別	N	Mean	SD	t	df	Sig. (2-tailed)
平均夜間睡眠時數	對照組	16	6.4688	.9911	-3.320	30	.002**
	猝睡症組	16	7.7500	1.1832			

**p<.01

表二・兩組在艾普渥斯嗜睡量表的差異

嗜睡程度	組別	N	Mean	SD	t	df	Sig. (2-tailed)
ESS得分	對照組	16	7.31	2.75	-6.057	29	.000***
	猝睡症組	15	14.60	3.89			

***p<.001

研究者在了解人格變項在猝睡症個案上是否與對照組有顯著差異，其中猝睡症個案在停藥階段作測量，將結果進行組間差異比較。發現在測量三個面向與18種人格分量表（兩組的平均數與標準差列在表三--1與三--2）有兩項分量表在兩組間有顯著差異，一爲外向性面向中的「活動力」(activity)量表(t=2.58, df=30, p<.015)，一爲與謹慎性面向之自我訓練(self-discipline)量表在兩組間有顯著差異(t=2.27, df=30, p<.030)，且其平均分數顯示猝睡症個案的活動性與自我訓練性傾向比對照組低。依據Costa & McCrare（1992）編制之NEO-PI 指導手冊資料說明「活動力」高分者行事節奏快速、動作靈活、充滿活力，傾向讓自己忙碌有生產力，低分者步調偏低、較無能量、偏向鬆散渙漫。而「自我訓練」高分者積極有能力，能自我要求以完成工作包括繁瑣事物，但是低分者則容易沒信心，容易放棄或延遲工作，自我控制力較低，常無法完成想完成之事。參照NEO-PI常模資料將分數強度分成五個等級（非常高分；高分、平均、低分、非常低分），猝睡症個案低分之兩項特質其分數落點均爲低分等級。由此可知，個案性格傾向上有其特殊性，都傾向低能量、控制力差、堅持度低。

表三--1 對照組與猝睡症組在三個人格面向的平均數與標準差

人格面向	組別	mean	SD	t	Sig. (2-tailed)
Neuroticism	對照組 猝睡症組	91.50 96.63	19.75 21.95	-.694	.493
Extraversion	對照組 猝睡症組	107.50 103.19	17.16 19.62	.662	.513
Conscientious-ness	對照組 猝睡症組	114.31 105.19	17.51 25.50	1.180	.247

N=32, 對照組 16 人, 猝睡症組 16 人, df=30

表三--2 對照組與猝睡症組在NEO PI-R各分量表上的平均數與標準差

組別	對照組		猝睡症組		兩組差異檢定	
人格分量表	Mean	SD	Mean	SD	t	Sig. (2-tailed)
Neuroticism Facets						
N1:Anxiety	16.81	4.13	17.56	4.69	-.480	.878
N2:Angry Hostility	14.25	4.23	14.00	4.59	.160	.874
N3:Depression	15.50	4.44	17.38	6.02	-1.002	.324
N4:Self-Consciousness	15.81	4.28	16.88	4.90	-.654	.518
N5:Impulsiveness	14.94	3.45	15.19	3.39	-.207	.838
N6:Vulnerability	14.19	2.83	15.63	4.54	-1.074	.292
Extraversion Facets						
E1:Warmth	21.50	3.92	21.13	4.73	.244	.809
E2:Gregariousness	18.13	5.12	19.06	6.03	-.474	.639
E3:Assertiveness	14.94	3.19	14.88	4.66	.044	.965
E4:Activity	17.19	2.07	14.56	3.50	2.580	.015*
E5:Excitement-Seeking	17.38	5.43	17.50	3.90	-.075	.941
E6:Positive-Emotions	18.38	4.66	16.06	5.90	1.230	.228
Conscientiousness Facets						
C1:Competence	18.25	2.41	17.81	4.29	.356	.725
C2:Order	17.50	3.74	16.75	5.65	.443	.661
C3:Dutifulness	21.50	3.31	20.88	4.54	.445	.660
C4:Achievement Striving	18.81	4.13	16.75	6.51	1.070	.293
C5:Self-Discipline	18.38	3.69	15.00	4.66	2.272	.030*
C6:Deliberation	19.88	3.77	18.00	4.52	1.274	.212

*p<.05 , N=32, 對照組 16 人, 猝睡症組 16 人, df=30

此外，猝睡症患者所經驗到的壓力程度與社會支持是否會較一般人不同，本部分分個人主觀壓力知覺與社會支持中物質資源與情感資源作探討，進行猝睡症組與對照組兩組間差異檢定。發現在整體主觀壓力知覺上兩組如假設確實有顯著差異（t=-2.538, df=30, p<.017），且猝睡症主觀壓力知覺較強於對照組個案；研究者進一步瞭解壓力各題項組間的差異程度，藉以作更多探討，結果發現在第1題「當發生不可預期的事情時，我會因此而感到沮喪」（t=-2.828, df=44, p<.008）與第3題「自己作了許多的努力，仍無法解決問題」（t=-2.510, df=44, p<.018）兩組間有顯著差異，其他四題則無顯著差異，包括第2題「我感到壓力很大，讓我神經緊張」、第4題「我感到事情是我不可控制的，讓我非常生氣」、第5題「事情必須靠自己來完成」及第6題「事情的困難度非常高，我無法克服它」（其平均數、標準差及t值請見表五）。在社會資源總分（t=.215, df=30, p<.831）、實質資源（t=-.252, df=30, p<.803）及情感資源（t=.541, df=30, p<.592）上，兩組間均無顯著差異（其平均數、標準差及t值請見表六）。

表五 壓力知覺各題項與總分在對照組與猝睡症組之平均數標準差與檢定結果

	組　　別	Mean	SD	t	Sig. (2-tailed)
第 1 題	對照組	2.13	.50	-2.828	008**
	猝睡症組	2.63	.50		
第 2 題	對照組	2.50	.73	-.659	.515
	猝睡症組	2.69	.87		
第 3 題	對照組	1.94	.44	-2.510	.018*
	猝睡症組	2.56	.89		
第 4 題	對照組	2.19	.54	-1.436	.161
	猝睡症組	2.56	.89		
第 5 題	對照組	2.94	.68	-.434	.667
	猝睡症組	3.06	.93		
第 6 題	對照組	2.00	.37	-1.168	.252
	猝睡症組	2.25	.77		
壓力總分	對照組	13.69	1.62	-2.538	.017*
	猝睡症組	15.75	2.82		

*p<.05, **p<.01, N=32, 對照組 16 人, 猝睡症組 16 人, df=30

表六 社會資源量表之平均數與標準差

	組　別	Mean	SD	t	df	Sig. (2-tailed)
情感資源	對照組 猝睡症組	26.56 26.94	3.08 5.11	-.252	30	.803
實質資源	對照組 猝睡症組	26.88 25.81	4.40 6.50	.541	30	.592
社會資源總分	對照組 猝睡症組	53.44 52.75	6.64 10.95	.215	30	.831

N=32, 對照組16人, 猝睡症組16人

討　論

本研究主要目的在探討猝睡症個案其心理社會層面的特性，在提出之二項假設上，研究結果假設獲得支持。以下分別就結果作進一步討論：

根據結果，猝睡症患者的人格特質有「活動力」與「自我訓練」分數顯著低於對照組之外，其他皆與一般人無差異，由此可知，雖然猝睡症已證實由生理因素導致，然性格傾向上也有其特殊性，都傾向低能量、控制力差、堅持度低。究竟是因爲嗜睡阻礙個人活動，使個人變得不可控制，或是原本個案在體質因素上就已具此性格傾向，值得探究。例如瞭解年輕個案其發病前性格與發病後之性格是否一致，性格與症狀究竟之關係，可繼續深論。

此外，筆者感興趣上述結果與國外已有之研究比較，國外文獻支持猝睡個案傾向社會內向或社會性低以及身體焦慮，而本研究資料顯示個案能量低較少從事社會性有關活動，此項與過去研究一致外，似乎本國個案有缺乏信心、控制感差及堅持度低的偏向，此項特性對個體的影響或呈現之社會心理意義，例如是否出現更多挫折與社會適應，值得未來深入探究。至於本國資料顯示焦慮傾向並未顯著高於對照組，國外資料顯示猝睡個案有此傾向特別是對身體焦慮，此部份筆者認爲除了研究工具的差異外，社會文化對嗜睡的詮釋是否也有不同，需要再做探討。

至於猝睡症者與一般人比較，確實感受到更多的主觀壓力，而且在能否自我控制的題項上顯現出更高的壓力，這可能是由於猝睡症的發作是生理性的，並無法由意志力或患者主觀意識控制，因此形成了患者對無法控制事情的壓力之知覺。而這些現象

顯示，在面對此類疾患時依據Taylor(1999)對慢性病的處置建議應放在如何提升生活品質議題之上來看，需考慮個案壓力感受在個人因應疾病中扮演之角色。亦誠如廖士程，李明濱，李宇宙（民89）三位學者主張在治療個案時在臨床上考慮特有生理現象外，還需要結合生物、心理以及環境社會面之努力，以本研究結果來看，猝睡症患者也需在此模式下被關注考慮。在社會支持度上，研究結果顯示猝睡症患者其環境資源與一般人無異，因此建議未來在健康維護與治療上，除藥物幫助外，可以針對特定性格因素如活動性、自我訓練性過低，特定壓力知覺如嗜睡的不可控制性協助個案因應問題。

本研究對於國內猝睡症患者進行首次人格與壓力知覺的測量，有了初步的結果，希望對於了解猝睡症這個疾病有所貢獻。猝睡症好發於青少年時期，往往延續至中年，對於正想好好唸書或打拼事業的人來說，無法克制的睡眠會造成職業上的極大不便與尷尬，甚至對自己信心全無。未來的研究方向除了對於此疾病有更深切的分析了解之外，最重要的也許是研究結果的臨床運用，幫助猝睡症患者與疾病好好共存。

註一：

與猝睡期間有關的症狀--

1. 猝倒指的是突發的肌肉張力消失，通常由強烈的情緒所引發，會持續幾秒到幾分鐘，易造成患者手上的物品掉落，兩膝彎曲或真的跌倒在地。
2. 將睡或將醒幻覺症狀會出現在大約兩到四成的猝睡患者身上，於正當入睡前或剛醒來之時會感受到強烈如夢般的影像（視幻覺），並常融合了真實環境的部分內容。
3. 睡眠麻痺則指的是患者經驗到自己已經醒來但是卻無法移動或說話的現象。睡眠相關的幻覺和睡眠麻痺常同時發生，會造成患者看見或聽見不尋常事物卻無法動彈的恐怖經驗，兩者通常僅延續幾秒鐘到幾分鐘且會自行消失。

註二：精神疾病診斷與統計手冊第四版(DSM-IV)對猝睡症的診斷準則如下：

A. 至少三個月期間每日發生無法抗拒而具恢復性的睡眠。
B. 並至少具備下列兩項之一:（1）猝倒(亦即突發兩側肌肉張力消失的短暫發作，大多伴隨強烈情緒而發生)；(2）快速動眼期睡眠一再插入睡眠與清醒之間的過渡期，並在睡眠發作或開始之時，表現將睡或將醒幻覺或睡眠麻痺。
C. 此障礙並非由於某物質使用(如:藥物濫用、臨床用藥)或其他一般性醫學狀況的直接生理效應所造成。

致　謝

承蒙輔仁大學理工學院提供本研究補助（計畫編號：35701529）謹此敬表謝忱。

參考文獻

李宇宙（民89）：睡眠醫學。台北市，健康世界雜誌社。

呂碧鴻、梁繼權、范姜群信、陳秀蓉(民84) ：社會支持、家庭互動與心理健康之關係。中華家醫誌，第五期，173-182。

廖士程、李明濱、李宇宙（民89）：睡眠的生物學基礎及臨床意義。台灣醫學。第四卷第六期，652-664。

蔡政楗（民89）：睡眠圖譜。台北市，合記出版社。

蘇東平(民89)：睡眠障礙之診斷分類及臨床評估。台灣醫學。第四卷第六期，665-672。

Benbadis, S. R., Perry, M. C., Sundstad, L. S. & Wolgamuth, B. R. (1999). **Prevalence of daytime sleepiness in a population of drivers.** Neurology, Vol 52(1), 209-210.

Beutler, L. E., Ware, J. C., Karacan, I. & Thornby, J. I. (1981). **Differentiating psychological characteristics of patients with sleep apnea and narcolepsy.** Sleep, 4(1), 39-47.

Broughton, R. & Mullington J. (1994). **Chronobiological Aspects of Narcolepsy.** Sleep, 17:S35-S44.

Broughton, W.A. & Broughton, R. J. (1994). Psychosocial impact of narcolepsy. Sleep, 17(8, Supp l), S45-S49.

Chen, M. C. & Piedmont R. L. (1999). **Development and Validation of the NEO PI-R for a Taiwanese Sample.** Progress in Asian Social Psychology Volume Ⅱ, 105-118.

Cohen, S., Kamarck, T., & Mermelstein, R.(1983). **A global measure of perceived stress.** Journal of health & social behavior, 24, 385-396.

Costa P. T. & McCrae, R. M. (1992). NEO PI-R, Bibliography for the Revised NEO personality and NEO five-factor inventory professional manual. Florida: Psychological Assessment Resources.

Franks, P., Campbell, T. L., Shields, C. G. (1992). **Social relationships and health: The relative roles of family functioning and social support.** Social Science Medicine, 34: 779-788.

John, M. W. (1992). Reliability and factor analysis of the Epworth Sleepiness Scale. Sleep, 115(4), 376-381.

Kaplan, H. I., Sadock, B. J. & Grebb, J. A. (1994). Synopsis of psychiatry. 699-716.

Krishnan, R. R., Volow, M. R., Miller, P. P. & Carwile, S. T. (1984). Narcolepsy: **Preliminary retrospective study of psychiatric and psychosocial aspects.** American Journal of Psychiatry, 141(3), 428-431.

Mignot, E. (1998). **Genetic and familial aspects of narcolepsy.** Neurology, 50, 1: 16-22.

Roy, A. (1976). **Psychiatric aspects of narcolepsy.** British Journal of Psychiatry, 128, 562-565.